UCLA

Title

Wet cells and dry cells: in situ transmission electron microscopy of electrically-driven, dynamical processes

Permalink

Author

White, Edward Robert

Publication Date

2014

Peer reviewed|Thesis/dissertation

Univeristy of California

Los Angeles

Wet cells and dry cells: *in situ* transmission electron microscopy of electrically-driven, dynamical processes

A dissertation submitted in partial satisfaction

of the requirements for the degree

Doctor of Philosophy in Physics

by

Edward Robert White IV

2014

Abstract of the Dissertation

Wet cells and dry cells: *in situ* transmission electron microscopy of electrically-driven, dynamical processes

by

Edward Robert White IV

Doctor of Philosophy in Physics

University of California, Los Angeles, 2014

Professor Brian C. Regan, Chair

Recent developments in nanofabrication techniques allow thin, wet systems to be imaged with high spatial and temporal resolution in the electron microscope. Coupling this ability with simultaneous, measured, electrical control, we cycle processes in liquid systems representing different electrochemical battery components. Dynamic processes imaged with these techniques, which represent a new state-of-the-art, include nanobubble collapse, dendrite growth, ion diffusion, and graphite intercalation. We also develop a sensitive system for measuring electron beam induced currents (EBIC) in the transmission electron microscope and apply it to graphene-MoS_2 heterostructures. This new hybrid material has strong light-matter interactions, and the EBIC measurements map the minority carrier diffusion length, which we observe to decrease with increasing radiation damage. These results have direct implications for the function and service lifetime of solar cells based on molybdenum disulfide.

The dissertation of Edward Robert White IV is approved.

Robijn Bruinsma

Bruce Dunn

Brian C. Regan, Committee Chair

University of California, Los Angeles

2014

For my grandmother, Nana,

Happy 100th birthday.

If I was half as sharp as you

I'd have finished this a long time ago.

Also for my parents, and for Alexandra.

TABLE OF CONTENTS

LIST OF FIGURES

LIST OF TABLES

<center>VITA</center>

2008	B.S. (Physics), University of Notre Dame
2008-2010	Teaching Assistant, University of California Los Angeles
2010	M.S. (Physics), University of California Los Angeles

<center>PUBLICATIONS</center>

S. B. Singer, Matthew Mecklenburg, E. R. White, and B. C. Regan, "Polarized light emission from individual incandescent carbon nanotubes", *Physical Review B*, 83, 233404 (2011).

Edward R. White, Matthew Mecklenburg, Scott B. Singer, Shaul Aloni, Brian Christopher Regan, "Imaging Nanobubbles in Water with Scanning Transmission Electron Microscopy", *Applied Physics Express*, 4, 055201 (2011).

S. B. Singer, Matthew Mecklenburg, E. R. White, and B. C. Regan, "Single-color pyrometry of individual incandescent multiwalled carbon nanotubes", *Physical Review B*, 84, 195468 (2011).

E. R. White, Matthew Mecklenburg, Brian Shevitski, S. B. Singer, and B. C. Regan, "Charged Nanoparticle Dynamics in Water Induced by Scanning Transmission Electron Microscopy", *Langmuir*, 28, 3695 (2012).

E. R. White, S. B. Singer, V. Augustyn, W. A. Hubbard, M. Mecklenburg, B. Dunn, and B. C. Regan, "In Situ Transmission Electron Microscopy of Lead Dendrites and Lead Ions in Aqueous Solution", *ACS Nano* 6, 7, 6308 (2012).

B. Shevitski, M. Mecklenburg, W. A. Hubbard, E. R. White, B. Dawson, M. S. Lodge, M. Ishigami, and B. C. Regan, "Dark-field Transmission Electron Microscopy and the Debye-Waller Factor of Graphene", *Physical Review B* 87, 045417 (2013).

C. C. Chen, C. Zhu, E. R. White, Chin-Yi Chiu, M. C. Scott, B. C. Regan, L. D. Marks, Y. Huang, and J. Miao, "Three-dimensional Imaging of Dislocations in Nanoparticles at Atomic Resolution", *Nature*, 496, 74 (2013).

Veronica Augustyn, Edward R. White, Jesse Ko, George Grüner, Brian C. Regan, Bruce Dunn, "Lithium-ion storage properties of titanium oxide nanosheets", *Materials Horizons*, 1, 219 (2014).

CHAPTER 1

Introduction

There are two distinct parts to this dissertation. The first part (and bulk of this document) describes experiments done using the rather newly developed fluid cell technology for imaging liquid systems inside a transmission electron microscope (TEM). The 'wet cells' in the title represent this fluid cell architecture and is described in Chapter 2. Chapters 3-6 describe a series of 'wet cell' experiments where we observe electrically-driven dynamical processes.

The second part of this dissertation describes a sensitive electron beam induced current measurement system built for a TEM. Chapter 7 details its construction, and Chapter 8 presents the experimental results. Here, the 'dry cells' represent the system of interest: a graphene-MoS_2 heterostructure that has potential use in solar cell devices.

The remainder of this introduction provides some necessary TEM and *in situ* TEM background.

1.1   Transmission electron microscopy (TEM)

The transmission electron microscope (TEM) has become the standard state of the art tool for imaging and characterizing materials at high resolution[1]. The basic principle of operation is shown in Figure 1.1[2]. Electrons are accelerated from a source to high energy where they make their way through the microscope column and scatter off the sample. These scattered electrons are what generate

contrast in any electron microscope. In a TEM the electrons pass through the sample, hence the name, and are detected below. There are two main imaging modalities in a TEM: conventional TEM, and scanning TEM (STEM).

In conventional TEM a large parallel electron beam illuminates the sample. Electron beam specimen interactions produce several different types of contrast: phase, diffraction, and mass-thickness[1]. The scattered electrons can either be used, or filtered out when forming the image by using apertures present in the back focal plane. Using the direct beam forms a bright field image by using only unscattered or forward scattered electrons. Considering only mass-thickness contrast, dense thick objects scatter many electrons and appear dark, while lighter thinner objects appear bright. A dark field image shows the opposite contrast and is used by selecting only electrons that are scattered out of the direct beam. Phase and diffraction contrast make TEM image interpretation much more complicated, but they also give rise to many of the structural characterization techniques that make TEM so useful. After selecting which electrons to use to form the image, the image plane is brought into focus on a fluorescent screen, and the emitted light is captured with a CCD (or film, in older microscopes).

Without changing the illumination conditions the back focal plane can be brought into focus by changing the optics below the sample. This allows the user to view the diffraction pattern of a crystalline sample, from which important structural information about the material such as lattice orientation and spacing can be deduced.

In STEM the electron beam is focused to a small probe and rastered over the sample. At each probe position an annular detector below the sample collects the scattered electrons and an image is formed where the intensity at each pixel is proportional to the number of electrons scattered into the detector at that probe position. Using the magnetic lenses below the sample the apparent position of the

Electron gun

Condensor aperture

Specimen port

Objective aperture

Objective lens

Intermediate aperture

Diffraction lens

Intermediate lens

Projector lenses

Binoculars

Fluorescent screen

Image recording system
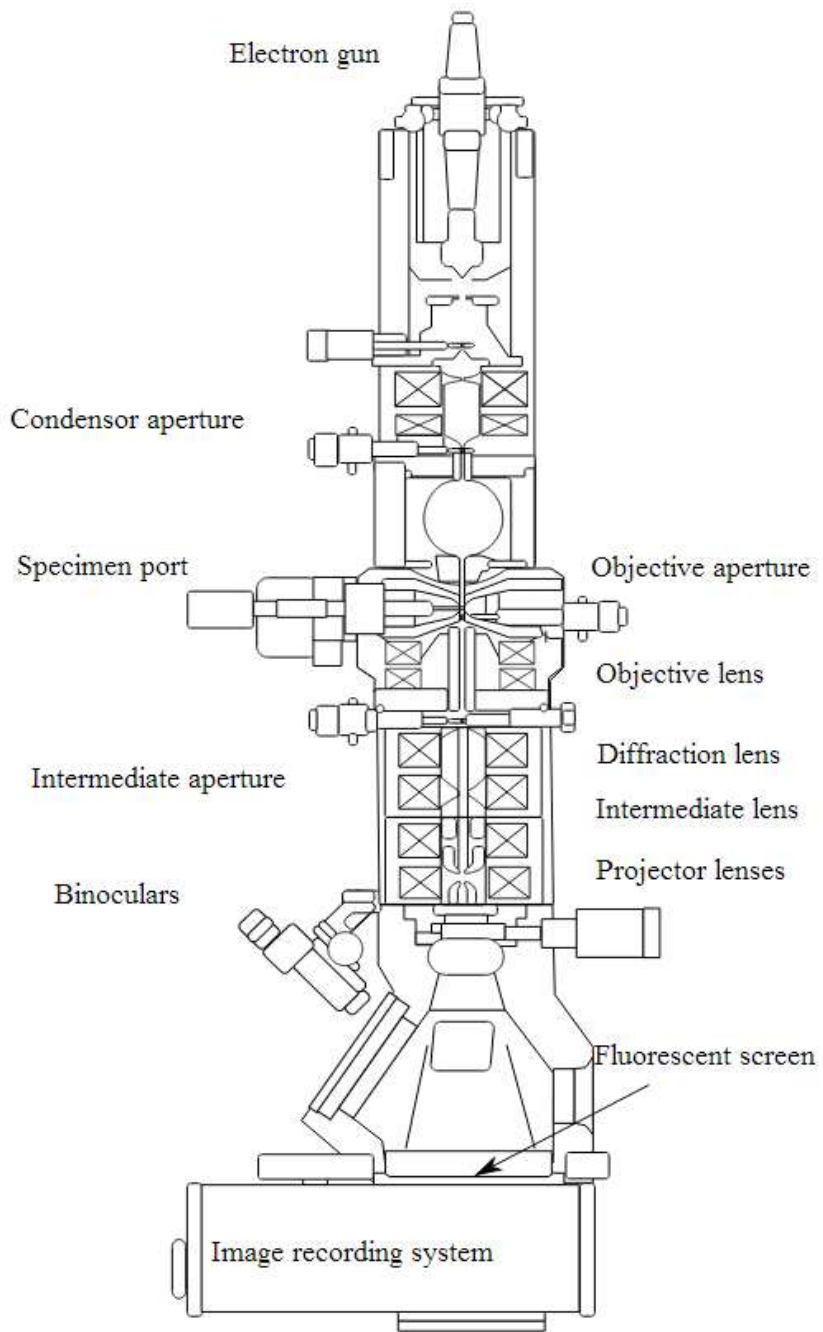
Figure 1.1: Transmission electron microscope schematic.

3

detector relative to the sample can be adjusted, giving the user control over what angle the electrons must be scattered in order to be collected by the detector. Thus the microscope can be operated in annual dark field, or high angle annular dark field modes. Annual dark field (ADF) images are similar to TEM dark field images in that they are sensitive to mass-thickness and diffraction contrast (and in principle phase contrast, with a suitable choice of beam convergence angle). High-angle annular dark field (HAADF) images are highly sensitive to the atomic number of the scattering atom. It is the operating mode of choice for performing atomic resolution imaging of samples with different atomic species since HAADF images are the most straightforward to simulate and thus interpret the contrast in terms of atomic structure.

1.2   *In situ* TEM

Materials characterization using the tools describes above is very well established and virtually every major research institute in the world interested in materials research is equipped with such an instrument. Beyond materials characterization where the sample is (ideally) static, there is a field dedicated performing experiments inside the TEM and imaging processes as they happen. This is done by using an external probe (electically biasing the sample, for example) or internal probe, the electron beam itself to modify the sample, or intiate some dynamic process. This field, *in situ* TEM, has greatly benefited from recent advances in detector speed and data storage technology. Imaging sample changes on the order of seconds, or less, was not feasible before the use of a CCD became standard on TEMs. A CCD allows for almost continuous acquisition with minimal wait time between frames, limited only by the time required for the charge wells to empty. This happens at a significantly faster rate than it takes to change the film in older TEMs. Continuous imaging during an *in situ* experiment has additional

data storage requirements given the enormous amount of data produced. Storing the images digitally makes it possible to generate and keep this data.

CHAPTER 2

Fluid cell TEM

To better understand physical and electrochemical phenomena that happen in liquids, it is important to image those processes at high resolution. Compared with a traditional optical microscope that has a diffraction limited resolution of a few hundred nanometers, a transmission electron microscope is an attractive alternative that offers atomic spatial resolution capability. Special care must be taken during the sample preparation process, as the sample must be very thin (< 1 μm) for the electron beam to easily penetrate. Progress in microfabrication techniques has allowed the successful construction of closed cell chambers in which a layer of liquid is sandwiched between two electron transparent windows. The chamber serves two purposes: to keep the fluid layer thin, and to separate the liquid from the high vacuum in the microscope column.

The birth of field of fluid cell TEM came in 2003 with a paper by Frances Ross of IBM and coworkers[3], which described imaging of electrochemical growth processes. Since then the field has exploded, with reports of biological cells, solution phase nanoparticle nucleation, and more reports of imaging electrochemical reactions[4, 5, 6, 7]. For material science and chemistry applications a probe is used to perturb the system so a particular phenomena or process can be observed. The two most common probes for such *in situ* fluid TEM experiments are an electrical bias applied to submerged electrodes[3, 6, 7] and the electron beam itself[5, 7].

In this chapter we describe the fluid cell construction methodology, as well as

our data acquisition procedure used for small signal detection and precise synchronization of the electrical transport and TEM data.

2.1 Fluid cell fabrication

The goal of the fluid cell chamber is to sandwich a layer of liquid between two thin membranes, such that the enclosure is electron transparent. We begin with a 200 μm thick Si(100) wafer. We grow 850 nm of SiO_2 followed by 20 nm of Si_3N_4 with LPCVD. On the back side of the wafer square or rectangular regions are defined with optical lithography and the oxide and nitride layers are selectively etched with a reactive ion etch in these regions. A KOH etch of the Si follows, leaving windows between 20 and 100 μm on a side composed of the top-side SiO_2 and Si_3N_4. On wafer metal electrodes (either gold with a chrome sticking layer or platinum with a titanium sticking layer) are patterned on the top side of the wafer using optical lithography and e-beam evaporation. The wafer is cleaved into individual chips. Chips with electrodes are 2.1 mm by 3.1 mm on a side, and constitute the 'bottom' of the sandwich. Chips without electrodes are 2 mm by 2 mm on a side, and constitute the 'top' of the sandwich. The smaller size allows electrodes to protrude from the bottom chip so we can make contact to the macroscopic pads near the end of the chip. The oxide layer is removed with an HF vapor etch, leaving only 20 nm of Si_3N_4. Figure 2.1 shows an example of each type.

With the pieces of the sandwich ready, the first step in constructing the fluid cell is to place a small droplet of liquid over the electron transparent window on the 'bottom' chip, as shown in Figure 2.1. A 'top' is then placed on the liquid droplet. Using micromanipulator probes the top is pressed down to achieve a thin layer. The separation of nitride layers (in the bulk part of the chip) is determined

7
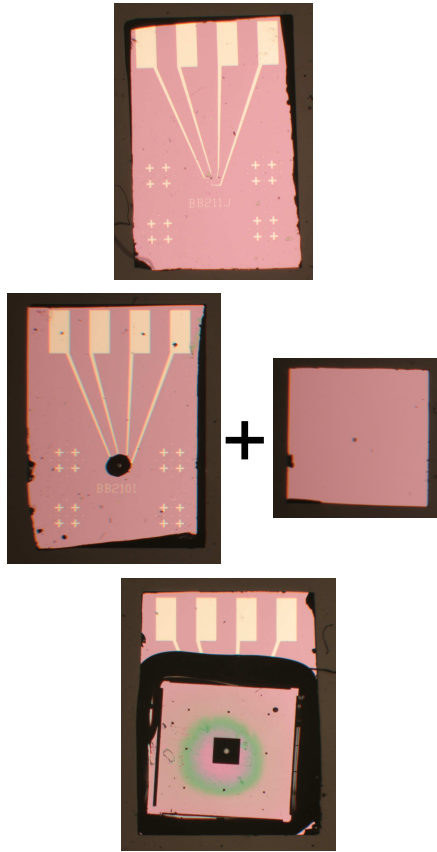
Figure 2.1: (top) Silicon chip with platinum electrodes. The chip is 2.1 mm by 3.1 mm on a side. The chip has been etched from the backside to reveal the $(30 \text{ um})^2$ electron transparent window composed of Si_3N_4 where the four electrodes meet. (middle) Another silicon chip with a drop of fluid placed on the window, along side a smaller silicon chip without electrodes with a similar electron transparent window. (bottom) Completed sandwich. The 'top' is placed on the 'bottom' and glued on all four sides with epoxy to create a vacuum tight seal. On the back side of the 'top' the etch hole is obvious, along with small holes that do not extend through the silicon which are used as guides to stick probe tips in for the alignment procedure.
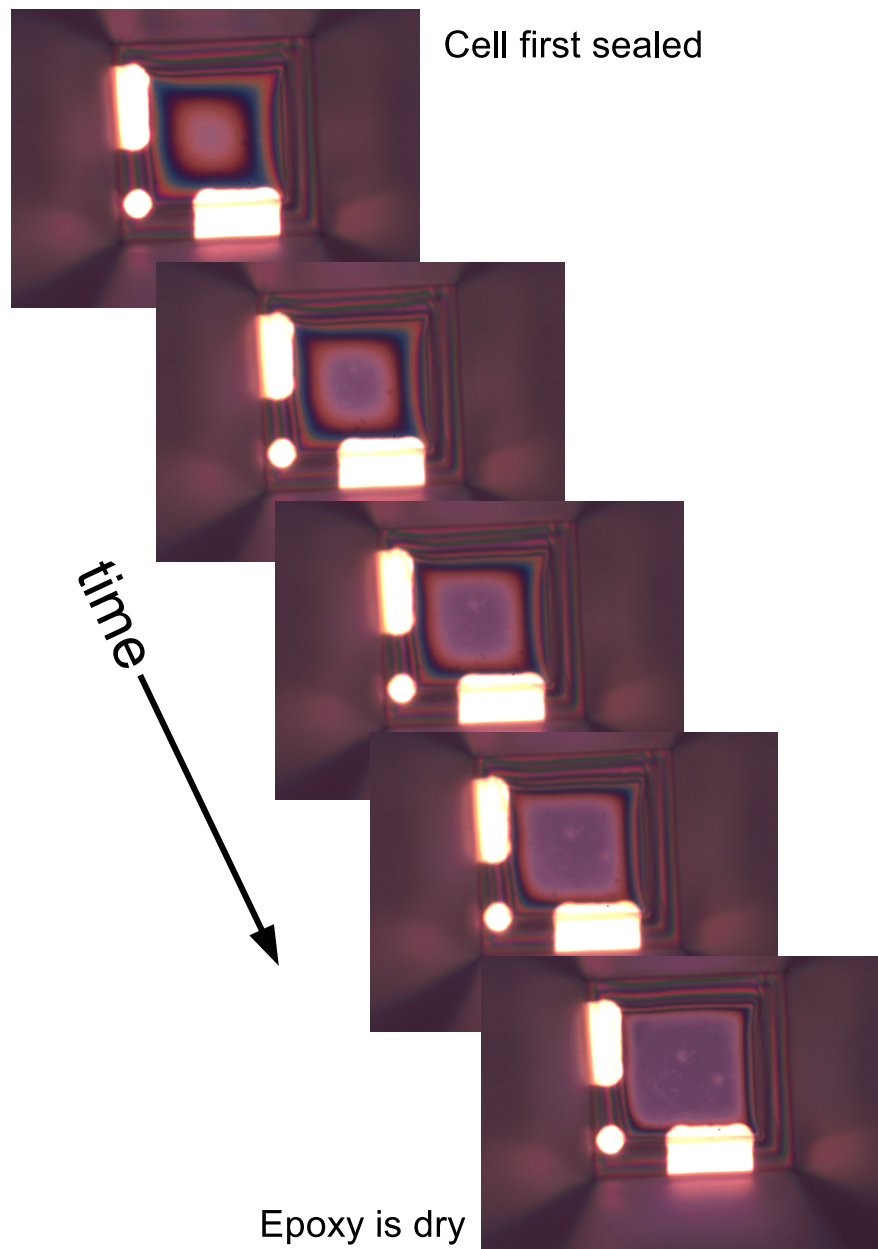
Figure 2.2: Time series of the electron transparent region of a fluid cell chamber as the epoxy that seal it dries. The window is 30 μm on a side. As the epoxy dries the fluid layer thickness becomes smaller.

by the electrode thickness, which is between 30 and 135 nm. The nitride of the electron transparent windows can bend since it lacks the silicon support, which eventually dictates the liquid layer thickness. The top window is aligned with the bottom window using the micromanipulator probes. This process is facilitated by inserting the probe tips into small etch holes in the silicon fabricated (defined with the first lithography step above). The holes are approximately 5 μm deep which is only 2.5% of the wafer thickness, and thus do not pose a risk to the structural integrity of the wafer. Once the two windows are aligned the wafer separation can be estimated with the optical microscope. Using an objective with a depth of focus of 1 μm the bottom window is brought in focus. If the top window is also in focus, then the wafer separation is 1 μm or less. If this is the case the cell is ready to be sealed. After placing a small amount of epoxy to a micromanipulator probe tip, epoxy is applied along the edges of the 'top' chip. The epoxy flows to make contact with the bottom chip and dries to create a vacuum tight seal. All fluid cells diccussed here were fabricated using this method with minor differences noted as needed for particular experiments. A completed fluid cell is shown in Figure 2.1.

A common problem in the field of fluid cell TEM is that the flexible Si_3N_4 windows bow outward when placed in the high vacuum of the electron microscope. The cell was sealed at STP and the micrscope column pressure is 10^{-7} torr or less, thus a pressure differential of one atmosphere exists across the Si_3N_4 windows causing them to bow outward, and increase the fluid cell thickness[7, 8]. Here, we use this window flexibility to achieve ultrathin liquid layers. The epoxy that seals the cell on all sides expands, very slightly, as it dries. As the epoxy expands, the spacing between the two wafers increases as well. Since the cell is vacuum tight and kept at room temperature the ideal gas law tells us the pressure inside the cell must decrease as the volume increases. Thus the epoxy expansion creates a negative pressure (relative to atmosphere) inside the cell. This causes
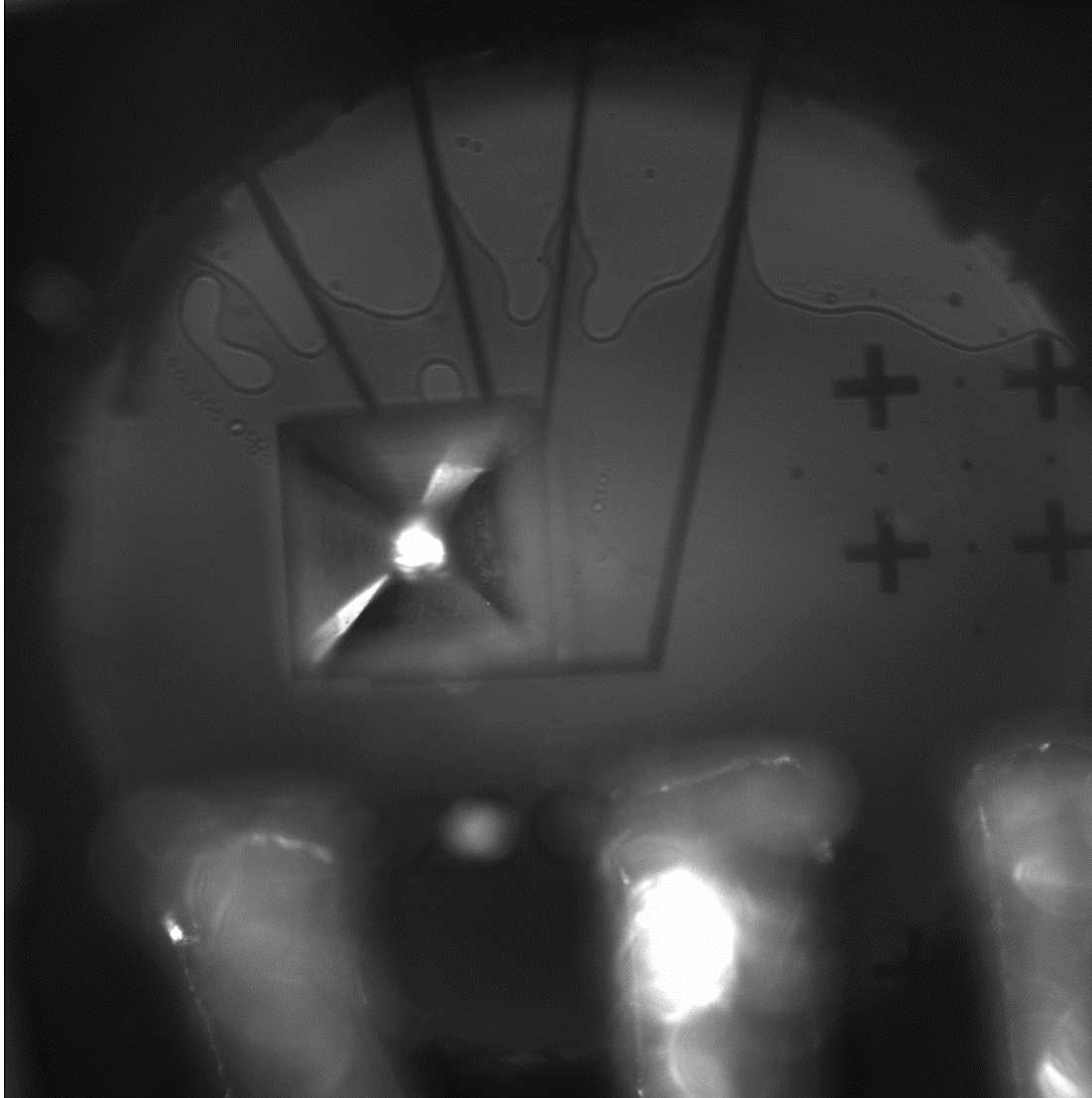
Figure 2.3: Imaging through a liquid cell with IR. Silicon is transparent to light with energy below its band gap of 1.1 eV. By back lighting the fluid cell and imaging with an IR camera we can see the fluid layer inside the liquid cell.

the Si_3N_4 windows to bow *inwards*, decreasing the liquid layer thickness in the region that is imaged. As the windows come closer together visible light interference fringes in the form of Newton's Rings give an indication of the liquid layer thickness. Furthermore the order of the colors verifies the cell is thinner in the middle of the window than at the edge. The color pattern red, green, blue, violet repeats as you move towards the center of the window. The color corresponds to the wavelength of light for which constructive interference occurs. Thus, as the wavelength of the light decreases (from red to violet) the thickness of the cell is decreasing as well. Once the cell is thinner than $\sim \lambda/2n$, where λ is the wavelength of light used and n is the index of refraction of the liquid, we no longer see an interference pattern and the cell has a uniform gray color in the center. Figure 2.2 shows a sample during the epoxy drying process, illustrating the expansion of the thin gray region.

Once the epoxy has fully dried we put the sample under vacuum to simulate the pressure differential present in the TEM and simultaneously observe changes in interference fringes. During pumping, the number of fringes in a thick sample decreases to zero and then reverses order, indicating the transition from the window bowing in, to bowing out. However, samples that have a thin (gray) region large enough before we place it under vacuum, show very little change in the interference pattern and appear to remain thin. There is only a small increase in thickness near the edges of the window. When the windows have a very thin layer of liquid between them they stay stuck together since surface tension forces are large enough to withstand the one atmosphere pressure differential and keep the fluid cell ultrathin.

We also verify the cell is in fact wet by imaging through the silicon. The band gap in silicon is 1.1 eV, thus it is transparent to light in the IR below this energy. After back lighting the silicon chip we image it with an IR camera. As shown in Figure 2.3 the liquid layer boundary is clearly visible.

The fluid cell is then placed in our custom electrical biasing holder from Hummingbird Scientific (see Figure 2.4) which is inserted into the TEM for imaging.
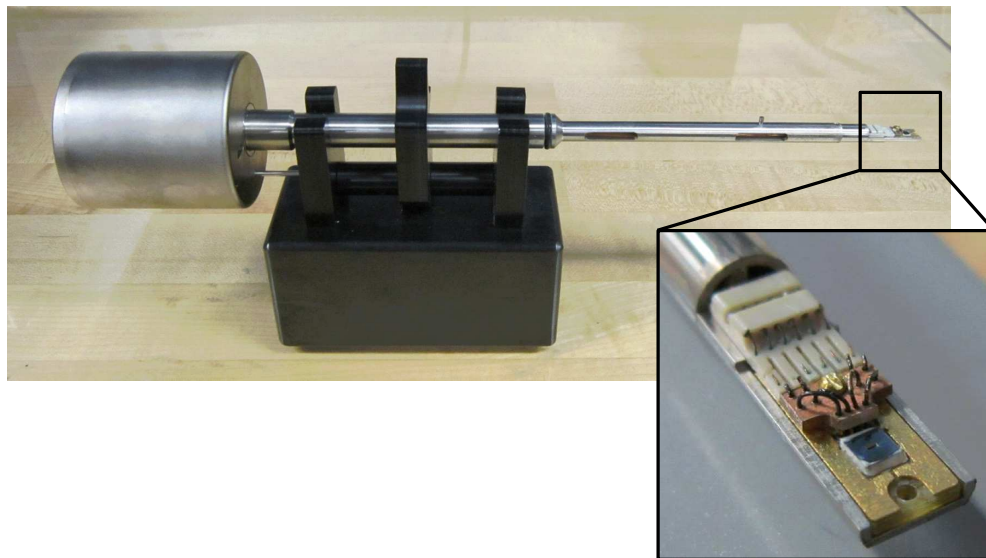
Figure 2.4: Fluid cell inside the electrical biasing holder

2.1.1 Failure modes

The one atmosphere pressure differential can have catastrophic consequences on the fluid cell if the nitride windows are too thin. Figure 2.5 illustrates this point, where the membrane ruptured when pumped on with vacuum. The cell was filled with a cesium chloride aqueous solution which recrystallized after the water evaporated.

Another challenge is that the use of certain solutions can affect the shelf life of the fluid cell. Figure 2.6 shows a series of optical photographs of a fluid cell containing uranyl chloride. A graphene sheet spans across two gold electrodes in the cell. Comparing Figures 2.6a and 2.6b the graphene sheet does not remain pristine during the three day span over which these photographs were taken. The
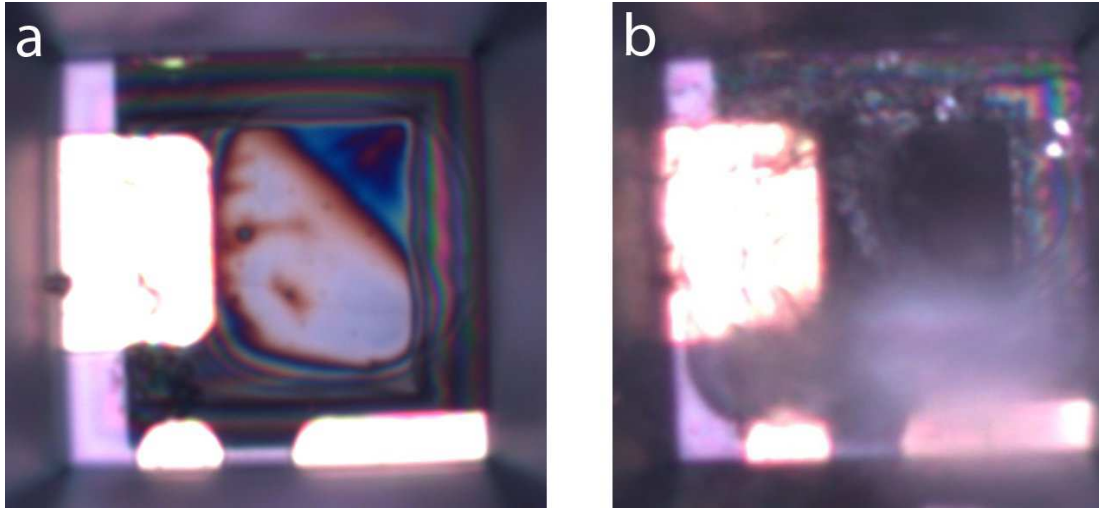
Figure 2.5: Optical photographs of the electron transparent portion of a completed fluid cell. The pictures are taken with a 50x objective. Each window is approximately 30 μm on a side. (a) Completed fluid cell immediately after construction. The silicon nitride windows are separated by a thin layer of a saturated cesium chloride solution. Gold contacts and alignments markers are also visible. (b) The same fluid cell after placing it under vacuum. The windows, unable to support the pressure differential, rupture.
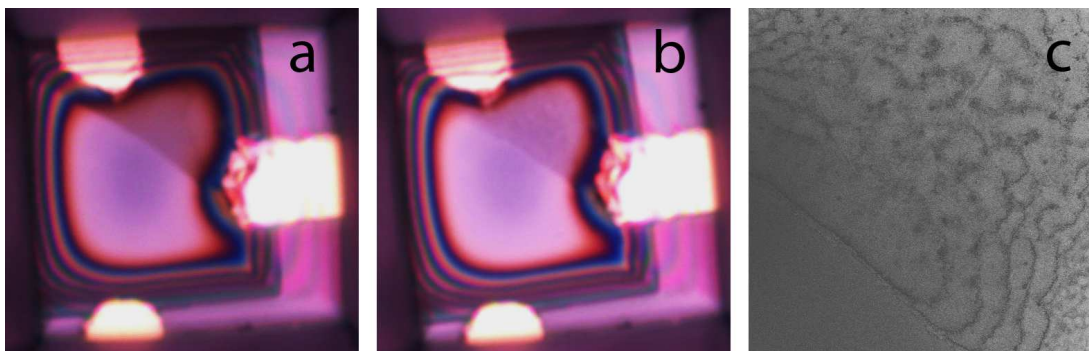
Figure 2.6: (a) Optical photographs of the electron transparent portion of a completed fluid cell filled with a saturated solution of uranyl chloride immediately after construction. A sheet of graphene sheet spans across the window and contacts the gold electrodes at the top and right portions of the photograph. (b) The same fluid cell three days later showing the deterioration of the quality of the graphene. (c) STEM picture of the graphene sheet after the photograph in (b) was taken.

ions in the solution likely attack the graphene surface, changing its morphology over the course of several days. Figure 2.6c shows a STEM picture of the graphene sheet several days after the fluid cell was sealed.

Contamination can be a major problem with in situ liquid TEM studies. Care must be taken to ensure that the sample, the sample holder, and microscope column are all free of volatile hydrocarbons that will be deposited on the sample by the beam. Buildup of contamination decreases resolution and complicates any quantitative analysis done on sequential series of images.

Understanding the different failure modes of the TEM fluid cell chamber is critical for consistently producing quality samples. Proper thickness of the membrane windows and liquid layer, effects of certain aqueous solutions on the other cell components, and contamination are all important considerations to account for when building a fluid cell chamber.

2.2 Data acquisition

2.2.1 STEM vs. TEM

All of the data in this work was acquired with an FEI 80/300 Low Base Titan, present at the Electron Imaging Center for NanoMachines at the California NanoSystems Institute at UCLA. A picture of the microscope is shown in Figure 2.7. The two imaging modalities are conventional TEM and STEM.

When imaging fluid cell systems it is generally preferable to operate in STEM mode. There are several reasons for this. First, the resolution when imaging a fluid cell is limited by the chromatic aberrations caused by the inelastic scattering off the liquid layer. It has been shown that STEM has higher resolution than TEM for all liquid layer thicknesses[7]. Second, for a given acquisition time for a single frame it is possible to obtain sub-frame rate time resolution under certain circumstances in STEM, which is not possible in TEM mode. The beam rasters in STEM mode, so the pixels are acquired in series, rather than in parallel (as in TEM mode). Thus each pixel acquistion takes a small fraction of the frame time, and changes to the system can be detected with almost pixel sensitivity. Third, as will be discussed at length later, beam effects play a major role in liquid cell TEM. We've found these effects are most easily controlled with STEM, where the quantities of merit, such as the dose rate areal density, are easier to control in STEM.

That being said, there are benefits to using TEM mode in some instances. Select area electron diffraction requires a parallel beam, thus operating in TEM mode is required. As needed, TEM mode will be used as well.

Figure 2.7: FEI 80/300 Low Base Titan at the UCLA EICN

2.2.2 The right electronics

The samples that can be imaged with TEM are necessarily thin and small. The electron transparent region of our fluid cells is approximately 100 nm thick and 30 μm on a side, giving a volume of 10^{-16} m^3. Accordingly, the signals we measure from the electrical transport are small and require sensitive instruments to measure them.

The transport measurements discussed here are all performed with a Keithley 6430 source meter and a Gamry 600 potentiostat. Both of these instruments are capable of femtoamp current sensitivity or better. In practice our signals are in the nano to picoamp range and are well within the measurement capabilities of these instruments.

We also taken special precautions to minimize stray capacitance. Stray capacitance introduces a background signal for any time dependent voltage measurement. Taking the time derivative of $Q = CV$ yields $i = C\frac{dV}{dt}$. Thus a background current proportional to the capacitance and the time derivative of the voltage is introduced for a measurement system with non-zero capacitance. The sample holder has approximately 100 pF of capacitance. Any added capacitance due to wiring the device is preferably much less than that. To accomplish this we built a box that sits directly on the back of the holder and has the proper electrical outputs for the given instrument. On the Keithley this is a BNC connector, which the Keithley preamp plugs into without the use of any cables. For experiments requiring the Gamry system we use a box that has banana jacks which the individually shielded banana cables from the Gamry plug into, again without any additional cabling. These efforts have limited the added capacitance a few tens of picofarads.

Furthermore, large stray capacitances can store a surplus of excess charge that can blow up a device via electrostatic discharge while making or breaking electrical

connections.

2.2.3   Synchronizing TEM and electrical transport data

There is a technical challenge required to synchronize the electrical transport data taken with either the Keithley or Gamry systems, and the image data acquired with the TEM. The problem arises from the inability to control our transport measurements with the computer used to operate the electron microscope. We have solutions for this when operating in TEM and STEM mode.

In TEM mode we begin by feeding a buffered version of the voltage output into a NI digitizing unit. The unit records the voltage with LabView software. Using the same software we send this information over the internal computer network to the computer controlling the microscope where it is written to a file. Digital Micrograph, the program used to acquire image data in TEM mode, reads this file and superimposes the voltage data in a corner of the image where it is saved with the image. The delay due to this write/read method is only approximately 100 ms, below the minimum time we use to acquire an image, which is about 1 s.

In STEM we utilize an unused port of the microscope's digitizing hardware designed for a bright field annual detector. We simply feed a buffered version of our voltage signal into this port and the voltage signal is digitized simultaneously with the HAADF signal. This yields the normal HAADF image along with a 'voltage image' where each pixel's value represents the voltage at that pixel, thus we achieve optimal TEM data/transport data synchronization, where we know the precise value at each pixel.

CHAPTER 3

Electron beam induced dynamics of charged nanoparticles in water

3.1 Introduction

At the cellular level most biological machinery is comprised of highly-charged molecules and macromolecular structures in aqueous solution [9]. Recent advances in the construction of environmental cells for use in transmission electron microscopes (TEMs) have made possible *in situ* experiments with high-vapor pressure liquids such as water [3, 10, 8, 6, 11, 5, 12, 13, 14, 15, 7]. While the field is still in its infancy, such measurements clearly hold great promise for revealing the molecular basis of cellular function [16, 17, 4, 18, 7]. However, a key assumption for the most straightforward interpretations of many *in situ* TEM experiments is that the imaging technique is not substantially disturbing the system under observation. Here we present data demonstrating that, under imaging conditions that are not extreme, the electron beam in a TEM can produce dramatic dynamic effects even in an inert aqueous environment. As these effects arise from charging induced by the imaging beam, they represent both a potential obstacle and a possible tool for studies of biological and other processes governed by the Coulomb interaction in water.

Previous studies on liquid-filled cells have seen no noticeable beam effects in some cases, and sample modifications in others. Gold nanoparticles exposed to $10^6 \, e/\text{nm}^2$ at 300 keV have been observed to move under the influence of a receding

fluid boundary or random diffusion, but the heating, momentum transfer, and charging effects of the electron beam were all found to be negligible [12]. A STEM dose of $10^5\,e/\text{nm}^2$ at 200 keV applied to 10 nm gold particles labeling biological molecules also showed no remarkable effect on the sample [16], but a dose ten times larger caused such particles to dissolve[10]. Two groups have used the electron beam to drive the growth of nanoparticles from solutions of metalorganic precursors. In one case platinum nanocrystals were created with a dose of 10^5–$10^6\,e/\text{nm}^2$ at 300 keV[5]. A similar experiment visualized the formation of lead sulfide nanoparticles, but dose information was not included in the report[15].

Using scanning transmission electron microscopy (STEM), we image ~ 4 nm platinum nanoparticles deposited on one of the windows of an electron-transparent, water-filled cell. An electron dose of $\sim 10^4\,e/\text{nm}^2$ causes the nanoparticles to be expelled outward from the center of the field of view (FOV). Such small doses have not previously been noted to affect the system under observation in an aqueous environment.

3.2 Experimental methods

As in previous *in situ* aqueous TEM experiments[3, 6, 17, 16, 5, 12, 10, 8, 11], the water is contained between two electron transparent membranes. The membranes are fabricated from 19 nm of Si_3N_4 and 850 nm of SiO_2 grown on a 200 μm thick Si(100) wafer[11]. A 20 μm $\times$ 300 μm hole is revealed in the silicon with a KOH etch and the membranes are subsequently thinned by an HF vapor etch to achieve electron transparency. In a scanning electron microscope (FEI Nova 600 Nanolab) equipped with a gas injection system, methylcyclopentadienyl (tri-methyl) platinum vapor is decomposed with the electron beam to deposit nominally platinum nanoparticles measuring $\sim$4 nm in diameter on the membrane. Two silicon chips, one with nanoparticles deposited and one without, are glued together with epoxy

(Hysol 1C-LV) around the outside edges, with a thin a layer of water separating the two chips. While the epoxy is setting micromanipulators are used to apply gentle pressure to the top chip to minimize the membrane separation. Although no spacer is used, the elevation variation produced by gold electrodes (not used in this experiment) and alignment markers on the bottom chip ensure that the chip spacing is greater than 130 nm. Under ambient conditions the membrane spacing in a properly assembled device is less than a few hundred nanometers, as indicated by the window's lack of color when viewed in an optical microscope. (Thicker devices show brightly colored windows due to optical interference effects.) In the TEM's vacuum environment the water layer thickness likely changes as the membranes bulge outward.[19] A cell contains less than 0.1 nanoliters of water.

We image the water-filled cells using an FEI Titan 80-300 TEM operated at 300 kV in scanning transmission electron microscopy (STEM) mode. Images measuring 512 pixels× 512 pixels are acquired with a dwell time of 1.3 μs per pixel, giving a frame acquisition time of 0.33 s. The spatial resolution is limited by the size of the pixel or the size of the electron beam after it has been spread by scattering in the sample (1–2 nm), whichever is larger.

3.3 Results and discussion

Figure 3.1 presents a time series of STEM images that span ~30 s and show an area that contains $\sim$ 2000 nanoparticles at first (see Supporting Information, Movie SM1). The initially immobile nanoparticles begin to move after several seconds of imaging. As the exposure time increases the nanoparticle clusters break apart and individual nanoparticles leave the FOV. On some occasions clusters of nanoparticles appear to move over each other as they move away from the center (see Supporting Information, Movies SM1–4). Ten individual nanoparticles are tracked in 3.1, with their trajectories shown in green. Generally the nanoparticles
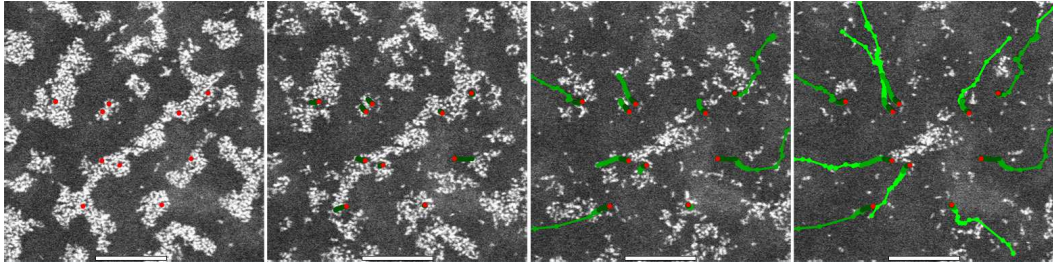
Figure 3.1: Time series of STEM images taken with a beam current of 57 pA and a 350 nm × 350 nm FOV (magnification $450,000\times$). The images are acquired $\sim$ 7 seconds apart, with time increasing to the right. The trajectories of 10 particles are shown with green tracks, with starting points denoted by red dots and the shade of green incrementing between frames. The scale bar in each image is 100 nm and the entire FOV is shown.

move radially outward from the center, and at times they appear to avoid clusters of other nanoparticles. The distance traveled per frame by each particle tends to increase with time, as indicated by the increasing separation between dots designating position measurements.

Half a minute of imaging under these relatively ordinary conditions decreases the density of nanoparticles in the FOV by an order of magnitude (Figure 3.2 a–b). In addition, the 'difference' image (Figure 3.2c) reveals that some particles in clusters neighboring the FOV, but not directly imaged, are also relocated. Light regions in the 'difference' image indicate that relocated nanoparticles come to rest as far as 50 nm from the FOV. Some nanoparticles may move much farther, as not all of the relocated material can be accounted for. We have observed displacements greater than 300 nm relative to the FOV boundary.

While the individual trajectories shown indicate that the particle flow is predominantly radial, particle image velocimetry (PIV) is used to ensure no selection bias. An image is divided into a 6×6 array of sub-images, and each sub-image is cross-correlated with the subsequent sub-image of the same location. Averaging the cross-correlations over an entire time series and multiplying by the frame rate gives the average velocity of the particles in each sub-image. These velocities are indicated with the vectors shown in Figure 3.2d. Deviations from purely radial motion are likely due to the tendency of nanoparticles to avoid large clusters of other particles. The longest vector corresponds to a velocity of 1.7 nm/s, while the shortest corresponds to 0.16 nm/s. In this PIV analysis motionless nanoparticles are counted while rapidly moving nanoparticles (when they cross a sub-image boundary between frames) are not. Both effects tend to decrease the average velocities returned, so the PIV values are smaller than the typical velocity of a moving nanoparticle. For individual nanoparticles in this data set velocities greater than 150 nm/s are observed (see Figure 3.1). Above this value conclusive
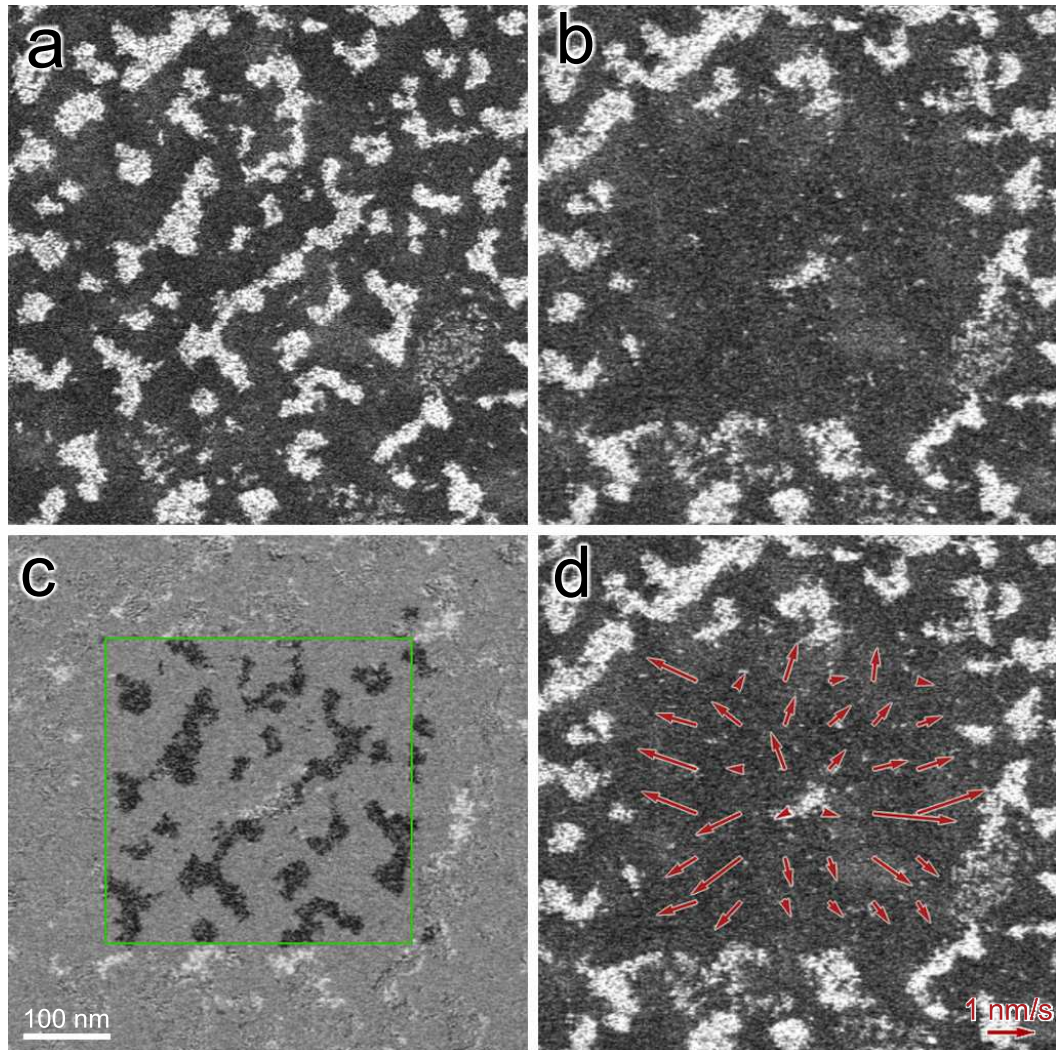
Figure 3.2: (a) The entire FOV of 3.1 plus the surrounding area, immediately before the 3.1 data was acquired. (b) The same region imaged immediately after the last frame of the data set. (c) 'Difference' image showing the result of subtracting the 'before' image from the 'after' image. Particles have relocated from the blacker regions to the lighter regions. The green box encloses the FOV from 3.1. (d) Results of the PIV analysis.

identification of a moving nanoparticle becomes progressively more difficult as the displacements between frames become comparable to the size of the FOV.

The rate at which the nanoparticles disperse can be controlled by adjusting either the exposed area (*i.e.* the microscope magnification) or the beam current. Thus we take the controlling variable to be the effective electron beam current density, where this density is defined as the beam current divided by the area of the STEM FOV. Larger current densities give increased dispersion rates. Figure 3.3 gives the nanoparticle density in the full FOV as a function of time for various beam currents. The nanoparticle expulsion is more complete and more rapid for larger beam currents. As the data in Figure 3.3 show, system modifications can be tuned to occur over time scales ranging from seconds to minutes. We are not able to establish a threshold below which charging effects are completely eliminated. Even successive images acquired with a total dose of $\sim 10^3\,e/\mathrm{nm}^2$ show subtle nanoparticle movement in this sample. This level of control over the dynamical time scales is a key advantage for studies in TEMs that are limited to data acquisition at video rates.

The complex particle motions observed in these data sets depend upon forces that are fundamentally derived from the Coulomb interaction, but can be described in more specific terms. Adhesion, interparticle, van der Waals, solvation, depletion, double-layer, electrostatic, viscous, steric, frictional, lubrication, and Brownian forces all play a role in moving a particle from its initial location to one hundreds of nanometers away [20, 21]. A detailed explanation is beyond the scope of this work, but the relative importance of some force mechanisms can be ascertained from the data.

The individual nanoparticles undergo driven motion that is predominantly radial and observable over many seconds. Both observations indicate that the Brownian motion expected for free particles in solution is strongly suppressed;
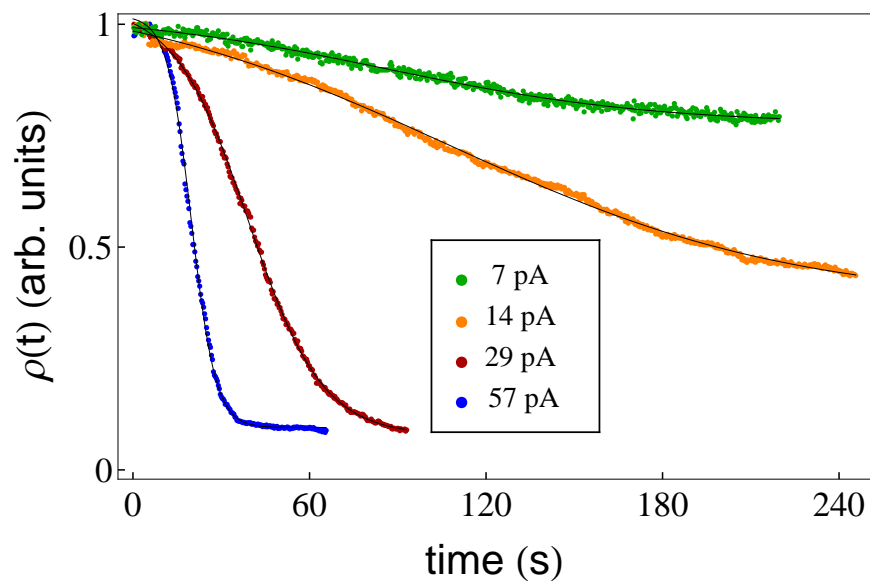
Figure 3.3: Density of nanoparticles in the full STEM FOV *vs.* time for beam currents of 7 pA, 14 pA, 29 pA, and 57 pA. Each curve is normalized by its maximum value.

adhesion forces continue to play an important role even after the nanoparticles begin to move. A free particle in a fluid drifts randomly due to Brownian motion, with a mean-square displacement $\langle x^2 \rangle = 2kTt/\alpha$, where kT is the thermal energy, α is the drag coefficient, and t is the time. In the low Reynold's number limit appropriate for small particles Stoke's law gives a drag coefficient $\alpha = 6\pi\eta\delta$, where η is the dynamic viscosity of the surrounding fluid and δ is the particle radius. For 4 nm diameter free particles in water ($\eta = 10^{-3}$ N·s/m^2) a drift time of 0.33 s gives an expected mean-square displacement $\sqrt{\langle x^2 \rangle} \sim 10$ μm, which is large compared to our FOV. Thus our Pt nanoparticles cannot be completely detaching from the membrane, because in this case single particles would not remain visible for more than one frame after their motion initiates. Random displacements between frames are smaller than the particle size, more than three orders of magnitude less than the expectation for free particles.

The small amplitude of the random drift implies a large effective drag coefficient. Hydrodynamic drag is known to be enhanced near a planar surface[22, 23], and previous *in situ* TEM measurements of the motion of ~ 10 nm gold nanocrystals in solution have seen strong substrate interactions and two-dimensional diffusion coefficients ~ 0.2 nm^2/s, similar to those seen here[12]. Using the same process recipe we deposited platinum nanoparticles on membranes and imaged them in the standard TEM high vacuum environment. These 'dry' samples showed no movement or morphology changes under identical beam conditions. Thus the presence of water, *i.e.* hydration, likely influences the adhesion and lubrication forces between the particles and the substrate and allows the particles to move[20].

To explain the radial motion it is necessary to invoke long-range forces, *i.e.* ones that are appreciable on length scales comparable to the size of the FOV. We attribute the radially-directed motion of the nanoparticles to electrophoresis caused by the charging of the membranes and the nanoparticles themselves. As is

well known, under the influence of a TEM's electron beam material can acquire net charge via Auger and secondary electron emission [24]. A uniform-charging model predicts a radial force based on symmetry considerations. In other words, to the extent that the material in the FOV charges uniformly under the influence of the electron beam, there will be an electric field with an in-plane component directed radially outward from the center of the FOV. Charged nanoparticles in the FOV will feel a force that decreases to zero at the center of the charged region (equivalent to the FOV in this model), which might explain why an anomalously large cluster of nanoparticles would be left in the center as in the last frame of Figure 3.1. (As this anomaly is not always observed, a local variation in the strength of the adhesive forces between the nanoparticles and the membrane could also be responsible.)

Debye screening limits the effective range of a nanoparticle's electromagnetic interactions. However, short-range forces explain the cluster-avoidance shown by some of the nanoparticles. Similarly charged surfaces with overlapping Debye layers are subject to an osmotic pressure that pushes the surfaces apart [20]. The deionized water used here would ideally have a Debye length of 1 μm, but exposure to epoxy and atmospheric gases during cell fabrication increases the concentration of ionic species. The Debye length is thus sub-micron, but still sufficiently lengthy that significant nanoparticle interaction occurs. To the extent that the Debye length is short, incomplete screening arises because the nanoparticles remain attached to the membrane. Unscreened fields penetrate the half-space delineated by the membrane-water boundary, which allows for charge interactions between particles and between particles and the membrane itself.

We have considered other possible explanations for the large-scale motion of the nano-particles. While the fluid cells often contain air pockets, vapor generates obvious contrast compared to the water[11]. No bubbles were near the FOV for the data reported here, thus interfacial phenomena, *e.g.* marangoni convection, can

be ruled out. Another possibility is thermally-driven diffusion, or thermophoresis [25], caused by the heat deposited by the STEM beam. The STEM beam produces a temperature increment above ambient in the center of the FOV which is given by [26],

$$\Delta T \simeq \frac{I_{\rm b}}{2\pi^2 e \kappa} \frac{dE}{dx} \ln \left(\frac{\pi}{2} \frac{a}{d} \right).$$ (3.1)

To estimate the temperature change ΔT we take the beam current $I_{\rm b} = 57$ pA, the energy loss rate per electron $dE/dx = 0.04$ eV/nm in water, and the governing thermal conductivity to be that of water, $\kappa = 0.5$ W/m·K[12]. For a FOV with dimension $a = 350$ nm and a probe with dimension $d = 1$ nm, these values give a temperature increment $\Delta T \simeq 0.001$ K. The small size of the implied temperature gradient indicates that heating by the electron beam is not responsible for driving the nanoparticles from their initial positions.

3.4   Conclusion

In conclusion, we have presented here the first TEM observations and analysis of charge-induced nanoparticle dynamics in solution. The nanoparticles acquire charge as a direct consequence of exposure to the imaging beam. Operating in STEM mode, a user has detailed control over the dose, dose rate, and exposed area. Since these parameters dictate the magnitude and location of the charging, STEM experiments can probe Coulomb-derived interactions in aqueous solution with unprecedented spatial resolution. These observations are especially relevant for *in situ* TEM studies of functional biomolecules and biostructures, where charge interactions are known to play a dominant role.

CHAPTER 4

Imaging nanobubbles

4.1 Introduction

Bubble formation in homogeneous liquids plays a critical role in initiating boiling, an effective mode of heat transfer that figures in a wide variety of natural and industrial processes [27]. The key variables governing inhomogeneous bubble nucleation involve sub-microscopic length scales, which are challenging to probe experimentally. We describe here a new method for probing nanobubble dynamics which takes advantage of the outstanding spatial resolution of transmission electron microscopy (TEM).

Nanobubbles have been previously studied with a variety of sophisticated but indirect methods [28], including optical [29, 30] and atomic force microscopy (AFM) [31, 32, 33]. Optical microscopy's spatial resolution is limited by the wavelength of the light used, and AFM requires some interpretation. For instance, soft domains with radii of curvature of 100–300 nm have been imaged with tapping-mode AFM and interpreted as nanobubbles [31, 32]. However, a polymer melt layer has been proposed as an alternative explanation [34]. Thus neither optical nor atomic force microscopy can provide compelling images of nanobubbles.

Direct evidence is particularly desirable in this case because of the fundamental questions about the stability requirements of a nanobubble [35, 28]. The Young-Laplace equation describes the pressure differential Δp across a spherical gas-liquid

interface,

$$\Delta p = \frac{2\gamma}{R},$$ (4.1)

where R is the bubble radius and γ is the surface tension ($\gamma = 72$ mN/m for water at room temperature). The ideal gas law $pV = NkT$ implies that an $R = 1\,\mu$m vapor bubble in water supports a reasonable pressure differential of 1.4 bar. However, at $R = 10$ nm, where eq. (4.1) should still be valid [35], the corresponding value is 140 bar. Such a large pressure differential is thought to be incompatible with bubble stability — a 10 nm bubble should dissolve rapidly [31, 32].

Thus the Young-Laplace equation appears to stand in conflict with a variety of experimental evidence supporting the existence of nanobubbles [28]. To address this issue we have built a general platform capable of studying bubble dynamics with nanometer spatial resolution.

4.2   Experimental methods

Like TEM cell constructions reported previously [3, 36, 17, 16, 5, 10, 8], our nanobubble cell contains a thin layer of liquid sandwiched between two electron-transparent membrane windows (see Figure 4.1). The $20 \times 300\,\mu$m^2 windows are revealed by a potassium hydroxide wet etch through a 200-μm-thick Si(100) wafer covered with 850 nm of SiO$_2$ and 19 nm of Si$_3$N$_4$. To further thin the windows, most of the oxide is removed with an HF etch, leaving less than 50 nm of total thickness.

Bubble formation is achieved in two ways: by injecting heat into the liquid to cause boiling, and by applying a potential difference between two submerged electrodes to electrochemically induce gas formation. For local heating, wires with a constriction of width $w = 200$ nm and length $\ell = 5\,\mu$m are fabricated on the
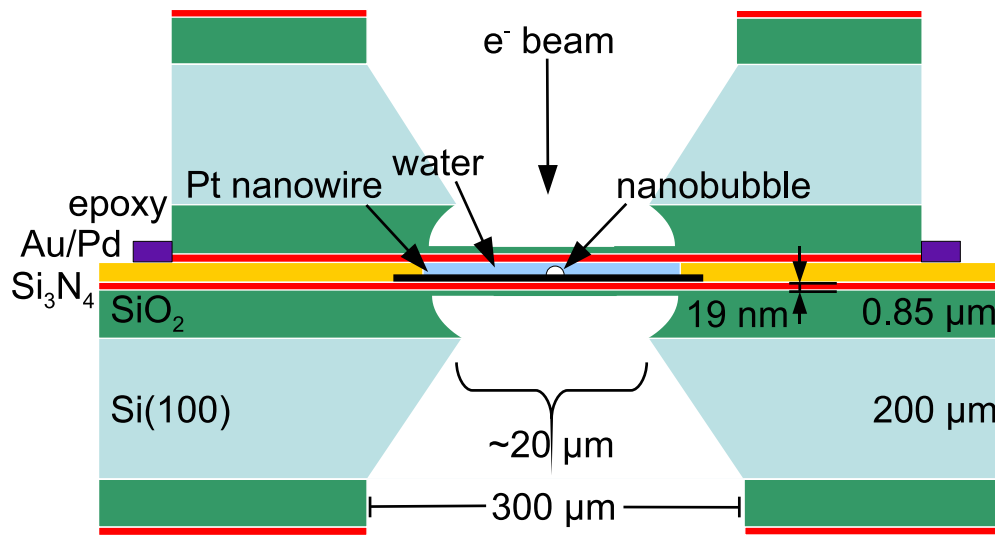
Figure 4.1: Schematic layout of the 'sandwich' TEM *in situ* nanobubble cell (diagram not to scale). The thickness of the fluid chamber between the Si_3N_4 windows is limited by the ~ 300 nm corrugation on the silicon chip surface due to the metal electrodes.

bottom membrane window using e-beam deposition of methylcyclopentadienyl (trimethyl) platinum. These nanowires connect to large, gold contacts defined with optical lithography that are accessible from the edge of the chip. Narrow, many-layer graphene strips are also used as local heat injectors. Graphene is electron transparent, and thus can allow unobscured imaging of nanobubble nucleation. Graphite electrodes separated by a few micrometeres are used for the electrochemical gas formation.

Through mechanical exfoliation of bulk graphite we isolate single and multi-layered graphene on Si/SiO2 wafers. The graphene is subsequently transferred to a silicon chip with gold contacts and a 20 nm thick Si_3N_4 electron transparent window. To create the fluid cell, a small droplet of liquid is placed between the chip and a second silicon chip without electrodes, which is maneuvered such that the Si_3N_4 windows are aligned. Applying epoxy around the edges of the cell creates a vacuum-tight seal, which keeps the graphene wet and the electron-transparent windows aligned when the cell is placed in the microscope's high vacuum.

We image the nanobubble cell in real-time using a TEM (FEI Titan 80-300) operated at 300kV in STEM mode. Bubble formation in the cell is initiated by applying a voltage to the electrodes in the fluid cell. A voltage pulse to the nominally platinum nanowire or graphene strip heats the nanostructure predominantly at the constriction. With sufficient applied power (P), a gas bubble forms. Application of a constant potential between two graphene electrodes electrochemically initiates continuous bubble formation.

4.3   Results and discussion

4.3.1   Platinum nanowire heating

A time series of STEM images showing a representative nanobubble event is presented in Figure 4.2. Here a voltage of 0.5 V is applied over a period spanning several frames. The bubble's initial growth from zero to micrometer size occurs in less than one frame (0.22 s), implying some degree of superheating [27]. The bubbles' morphologies are reproducible with repeated pulsing, which suggests heterogeneous nucleation, but such fast growth prevents unambiguous localization of the nucleation site. The rapid nucleation phase is followed by a period of slower growth, which terminates when the applied bias is set to zero. The vapor bubble then collapses over a period of 9 frames, finally disappearing within one frame when it reaches a radius of 70 nm.

For the device shown in Figure 4.2 an applied bias of 0.5 V is sufficient to create a vapor bubble that can be imaged. Reducing the applied bias to smaller values leads to the absence of visible bubble creation rather than smaller bubbles. Our inability to create and visualize arbitrarily small bubbles, *i.e.*, the existence of a power threshold for metastable bubble creation, further supports the superheating hypothesis.

While no chemical change is definitively seen in any of the experiments reported here, mechanical modifications to the membrane are observed. In particular, the varying contrast seen in the water-covered sections of the membrane in Figure 4.2 (for instance, the lighter crack-type feature extending from the upper electrode to the lower) was not present in the pristine device. These features appeared when the bias voltage pulse first reached $\sim 80\%$ of the metastable bubble initiation value, and showed some evolution with time. We interpret these features to be tears or folds in a thin layer, possibly the silicon nitride, that initially
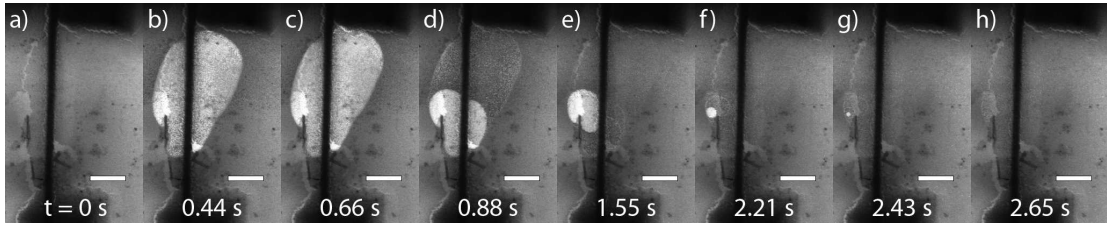
Figure 4.2: Time series of STEM images showing the nucleation and collapse of a bubble. At t=0 a 0.5 V, 1 mA pulse lasting 740 ms is initiated on the nanowire, the dark strip spanning each image from top to bottom. The nanowire is initially completely covered with water (a), but a microbubble appears in the next image (b) and grows slowly (c) as the input electrical power is maintained. Images (d) though (g) show the collapse of the bubble after the pulse ends. The scale bar in all images is 1μm. The radius of the bubble in image (g) is 70 nm. The dark feature to the left of the nanowire and extending halfway up from the lower electrode is membrane material relocated from the lighter regions immediately to its left.

covered the membrane uniformly, but was reconfigured by surface tension stresses resulting from interaction with a bubble. In other words, bubbles formed below the metastable bubble creation threshold and modified the membrane window surface, but collapsed before they could be imaged.

The heat-nucleated bubble formation depicted in the images of Figure 4.2 suggests that the water is boiling. We estimate the maximum temperature differential ΔT achieved at the midpoint of the nominally platinum nanowire by taking the nanowire to be a one-dimensional, isolated system. Then $\Delta T = P\ell/8\kappa tw$, where κ is the nanowire's thermal conductivity and t is its thickness [37]. The nanowire's resistance of 500 Ω implies an effective thickness of $t = 5$ nm, a value less than the deposited thickness of 200 nm because of incomplete fractionation of the metal-organic precursor gas. For platinum, $\kappa = 70$ W/m·K, implying ΔT as large as 4000 K. This number is certainly an overestimate, as cooling via the thermal links through the water and silicon nitride has been neglected. However, those thermal conductivities (0.6 W/m·K and 2 W/m·K respectively [5]) are small in comparison to that of platinum. Furthermore, the pressure in the cell may be lower than atmospheric pressure. The cell is loaded at ambient pressure, but the cell volume might increase due to, for example, the elasticity of the epoxy when the whole device is placed in the TEM vacuum. In any case, voltage pulses of order 0.5 V are clearly capable of bringing the nanowire to 100 °C or beyond.

While the electrical heat input could be inducing nanoboiling, we note that the gas bubbles produced might be predominantly filled not with water vapor, but rather with air coming out of solution as a result of the local temperature increase. At present we cannot discriminate between these two possibilities.

The collapse to zero radius of the nanobubble of Figure 4.2 between images (g) and (h) emphasizes the ability of this technique to address very small bubbles. Bubble disappearance at radii of 50–300 nm was common among all bubbles
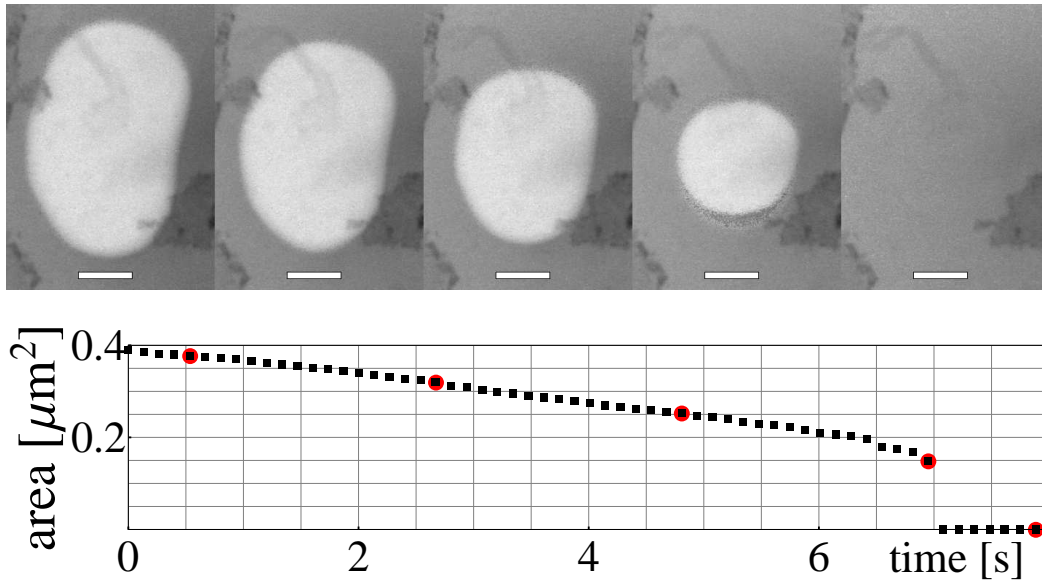
Figure 4.3: (Top) Time series of high resolution STEM images showing the collapse of a nanobubble. The scale bar in all images is 200 nm. (Bottom) Bubble area [μm^2] *vs.* time [s] as determined by a frame-by-frame analysis. The frame rate here is faster than that in Figure 4.2; each data point is separated by 130 ms. The five red data points correspond to the five images shown.

nucleated. Figure 4.3 presents a time series showing the collapse of a nanobubble. For the first 7 s shown, the bubble's area is observed to decrease at a nearly constant rate of $\sim 0.03\,\mu\text{m}^2/\text{s}$, reaching a final radius of 220 nm. At $t = 7$ s the bubble vanishes within a single frame, implying an areal decrease rate that is at least a factor of 30 times larger. All of the bubbles we observed underwent a single-frame collapse at some critical radius; none showed areas that decreased smoothly to zero.

4.3.2 Many-layer graphene heating

The high-quality, mechanically-exfoliated graphene is an ideal substrate on which to form nanobubbles via Joule-heating. Figure 4.4 shows optical images of a small bubble forming as a graphene electrode boils the water inside a liquid (water) cell. The graphene sheet contacts two gold electrodes and gives a circuit resistance of 2.2 kΩ. The bubble forms within 34 ms (one frame) of the application of a 1.6 V pulse (300 ms), and begins to shrink immediately afterwards (Figure 4.4c-d). From the positioning of the bubble, which has its centroid between the gold electrodes and not over one of them, it is evident that the bubble nucleated on the graphene itself. Such a device is thus ideal for STEM imaging of thermal nanobubbles, for if the nucleation site can be identified it can be directly imaged with high resolution.

4.3.3 Electrochemically induced bubbles

While a Pt wire effectively creates individual nanobubbles, it most likely obscures the corresponding nucleation sites in the STEM projection image. Here we bias a liquid (H_2SO_4) cell containing electron-transparent graphene electrodes and image nanobubbles forming. Since in this case the nanobubbles are generated electro-chemically via the formation of hydrogen gas ($2H^+ + 2e^- \longrightarrow H^2$), the physics

39
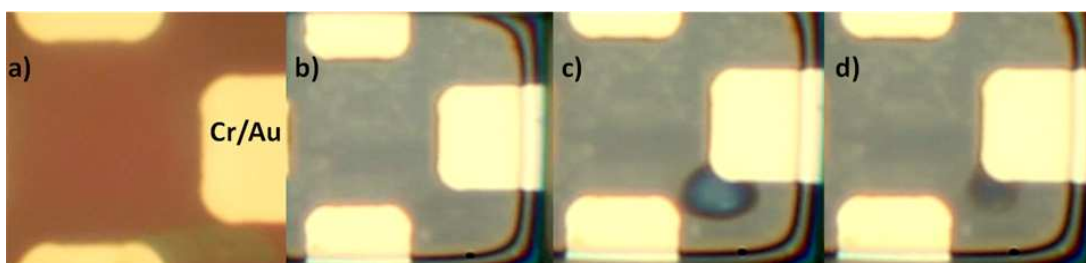
Figure 4.4: Optical images showing bubbles forming across graphene (approximately 2-5 layers) that is electrically connected to the bottom and right Cr/Au electrodes. (a) the graphene is visible over the window before liquid (water) is applied and the cell is sealed with epoxy. The cell shows signs of being wet in images (b) through (e). A 300 ms pulse of 1.6 V was applied to create the nanobubble shown in (c). The cell drew 610 μA during this pulse. (d) shows the collapse of the bubble after the pulse has been applied. The scale bar is 10 μm.

underlying bubble nucleation is quite different. Thus graphene shows promise for characterizing the nucleation sites of bubbles produced both thermally and electrochemically.

Figure 4.5 shows images taken from a 3 minute liquid cell STEM video of electrochemical nanobubble production on a graphene electrode. The graphene electrode is visible, though only barely in Figure 4.5b-e; a yellow line has been drawn on the electrode boundary in Figure 4.5e as a guide to the eye. Nanobubbles are forming in various locations on the graphene, indicating the existence of multiple nucleation sites. Efforts are underway to identify and characterize such nucleation sites by exploiting the low background from these electron-transparent graphene electrodes.

4.3.4 Beam induced bubble stabilization, creation, and manipulation

Bubble collapse can be prevented by the STEM beam alone. The first hint that such an effect exists can be seen by comparing the slower, temporally resolved rates of bubble shrinkage for the bubbles of Figures 4.2 and 4.3. These rates are quite different: the former rate is ~ 50 times the latter when comparing bubbles of similar areas. This discrepancy is observed repeatedly and is correlated with the STEM magnification setting. In general faster shrinkage rates occur at low magnification and *vice versa*.

Figure 4.6 illustrates this effect dramatically with a time series of eight images of a single bubble. Here pairs of images acquired at magnifications alternating between high and low show that increasing the STEM magnification alone reverses the bubble collapse. The STEM beam current is 0.8 nA, and the total field of view changed between 13, 9.2, and 4.5 μm per side for the three magnifications shown. Thus changing the dose rate (averaged over the field of view) from 4.7 or

41
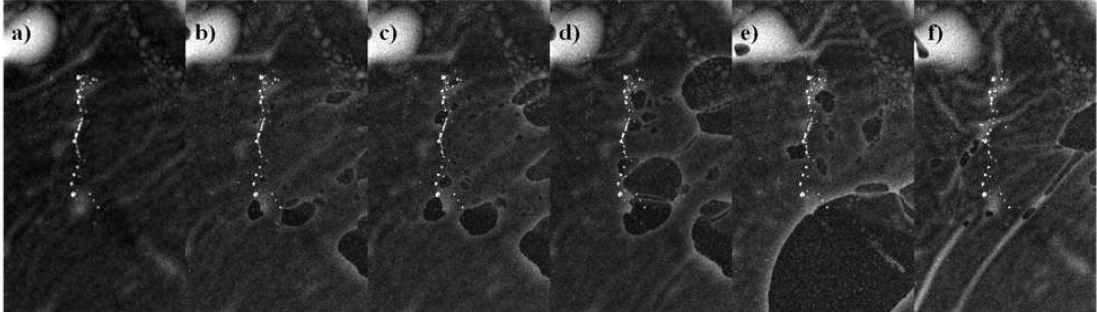
Figure 4.5: (a)-(f) In situ STEM images (8.2 x 14.6 μm^2) taken at 5000x showing growth and collapse of nanobubbles. Gas is electrochemically produced in the liquid (H_2SO_4) by applying a bias between two graphene electrodes. The positive graphene electrode is visible in images (b)-(e) and is depicted above a yellow outline in (e). The nanobubbles form on the graphene expanding throughout the liquid cell. (f) Wrinkles in the top membrane after bubbles have been made. The scale bar is 1 μm.
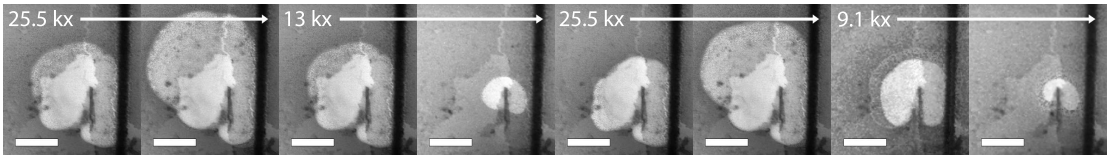
Figure 4.6: Time series of bubble images acquired at different magnifications showing STEM beam control of bubble size. The images have been digitally rescaled to the same apparent magnification. At high magnification (25.5 kx) the bubble grows, but switching to low magnification (13 or 9.1 kx) causes it to shrink. Given sufficient time at low magnification the bubble will collapse entirely, as occurred 0.66 s after the last image. No electrical power was applied to the cell at any time during this sequence. The scale bar is 500 nm.

9.5 A·m^{-2} to 40 A·m^{-2} is sufficient to make this shrinking bubble grow.

The mechanism by which the STEM beam influences the bubble size is not yet understood. The obvious suspect is heating. Electron-beam heating of particles on poorly conducting substrates has proved capable of raising local temperatures by hundreds of degrees[38]. However, the lowest thermal conductivity in this system, excepting the bubble itself, is water's $\kappa = 0.6$ W/m·K, and such conductivities are thought to be too high to support temperature differentials of more than a few degrees[5]. A simple estimate supports this view: the STEM beam represents a total power of 0.8 nA×300 kV, or roughly half the power the nanowire deposits electrically. Given that the nanowire produces temperature shifts of $\sim 100°$C and the sample absorbs only 10^{-3}–10^{-4} of the beam, the beam-induced shifts should be of order a degree or less, averaged over the field of view.

Under some circumstances the STEM beam can nucleate and stabilize a nanobubble. Figure 4.7 shows two different bubble patterns written by applying the STEM beam to individual points for sustained periods. Here the images are acquired in annular dark-field mode (ADF) and the bubbles appear dark. The beam-nucleated nanobubbles persist for many seconds, which is enough time to write and subsequently image a complicated pattern. Employing different write times, bubbles of different sizes can be produced. As shown in Figure 1, bubbles of radii 50 nm and 5 nm are generated using write times of 1 s and 0.1 s respectively. The smaller bubbles appear grainy because they are not large in comparison to our 12 nm spatial resolution. They appear, persist, and disappear in an identical fashion to the larger ones, with the only difference being that the timescales are shorter by a factor of 10.

Using a similar technique pre-nucleated bubbles can be locally modified. Directing the beam to a single, nanometer-size location, and holding it there for a period much longer than a typical dwell time can displace a bubble boundary, or
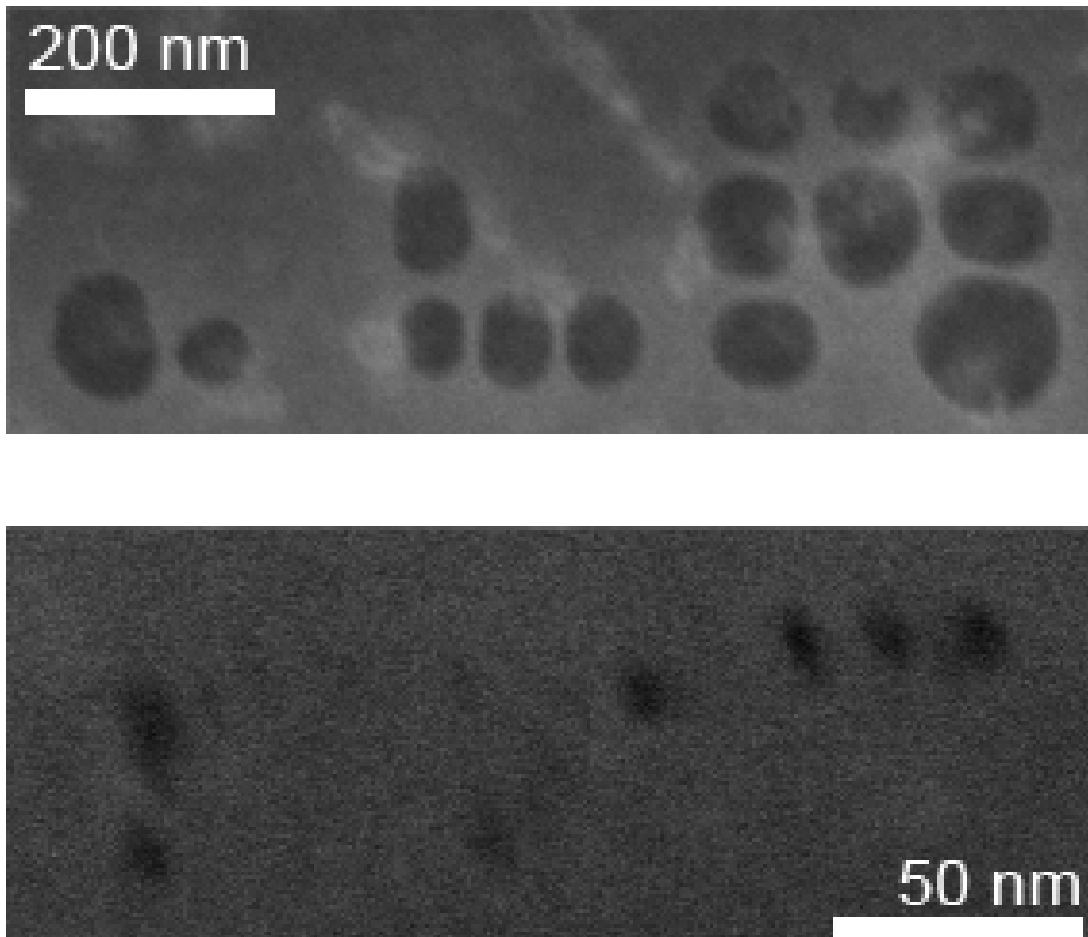
Figure 4.7: Annular dark-field STEM images of nanobubbles nucleated by fixing the STEM beam at user-determined positions. (top) The STEM beam is positioned at several points for 1 s each to create a pattern of bubbles. Each bubble has a diameter of 100 nm or less. Increasingly complex patterns are created from left to right. (bottom) Here the STEM beam is held at each point for 0.1 s, which creates much smaller nanobubbles, approximately 5 nm in radii.

even puncture a bubble as shown in Figure 4.8. The first frame shows an annular bright-field image of a bubble nucleated with a current pulse driven through the platinum wire spanning the field of view from top to bottom. The subsequent images illustrate how pointing the beam through the interior of a bubble can cause the bubble to collapse in the center. We attribute this collapse to a charging effect: the membrane acquires positive charge such that the pressure force supporting the bubble wall is overcome. Remarkably this effect is persistent over time periods ranging up to a minute after the local dosing ceases even as the rest of the now-toroidal bubble collapses, it does so without ever piercing the area occupied by the hole.

Thus these dramatic changes in the bubble dynamics are either produced by relatively small temperature shifts or another dose-related mechanism. Temperature-induced vapor pressure changes could have an outsize effect if the bubble pressure is substantially lower than that given by a naive interpretation of eq. (4.1). The bubble radius of curvature could be larger than it appears because the TEM produces an image based on a two-dimensional projection of the three-dimensional bubble. The bubbles as observed are generally not circular, implying that they are attached to the membrane and that the liquid-vapor-membrane interfacial energies vary with position. The forces pinning the contact line to the substrate might be large compared to those minimizing the vapor-liquid interfacial area [31]. The bubbles' apparent diameters are observed to change smoothly from large to small compared to the membrane separation. Also, the contrast differential between edge and center is small, implying nearly constant column density. For these reasons we think it likely that the bubbles are nearly flat, and that a complete vapor column between the membranes is never achieved. Neglecting the position variation, we model the bubble as a spherical cap [33], writing

$$\Delta p = \frac{2\gamma}{r_p} \sin \theta_c, \tag{4.2}$$
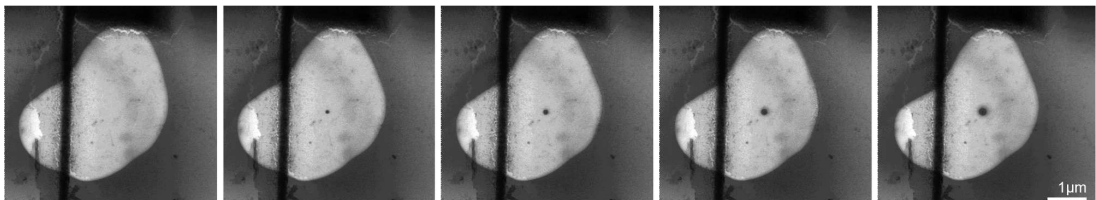
Figure 4.8: Annular bright-field STEM images demonstrating hole creation in a bubble with a fixed STEM beam. The left-most image shows the initial state of a stable bubble, taken more than 2 minutes after a nucleating heat pulse was delivered to the pictured platinum wire. The STEM beam is then fixed on the bubble for 3 s, which creates a hole, as displayed in the second image from the left. Directing the beam to the same spot for another 3 s causes the hole to grow larger as shown in the middle image. The final two frames show that repeated doses of the same size drive continuing size increases.

where r_p is the radius of the vapor-solid interface (taken to have cylindrical symmetry) and θ_c is the contact angle between the vapor-liquid and the vapor-solid interfaces. Thus for small θ_c (*i.e.*, thin bubbles and a hydrophobic membrane) the radius observed is best approximated by r_p, not R. A small θ_c also gives a small pressure differential, implying that small temperature changes could have a large effect on a prenucleated bubble. Other possible dose-related mechanisms include beam-induced electrochemistry, direct hydrolysis by the beam, and charging effects.

The observations presented here show that the electron beam of a scanning transmission electron microscope can generate and manipulate vapor bubbles in water. Since STEM allows facile, precise control of the position and dwell time of the electron beam, new bubbles can be nucleated and existing ones modified in tailored patterns.

4.4   Conclusion

We have imaged nanobubbles in water using a TEM in STEM mode. Injecting heat locally produces bubbles that grow rapidly to micrometer radii, and then shrink slowly to sub-100 nm size before vanishing on a timescale rapid compared to our temporal resolution ~ 0.1 s. At high magnifications the STEM beam alone can reverse bubble collapse. This clear evidence of the STEM beam's ability to change nanobubble dynamics may have important implications for STEM investigations of other liquid samples, for instance biological cells in aqueous solution [17, 16].

CHAPTER 5

Lead dendrite formation and ion diffusion in aqueous solution

5.1 Introduction

The physical structures produced by electrochemical deposition and removal play a critical role in determining the power density, lifetime, and ultimate utility of many energy storage devices. For instance, under repeated cycling through various states of charge and discharge metal electrodes in batteries reconfigure, gradually losing performance. Dendrites in particular contribute to important failure modes for many battery technologies, including those based on lead-acid, zinc-air, lithium, and lithium-ion chemistries[39, 40]. An improved understanding of the physical and chemical processes underlying dendrite formation thus is directly linked to modern challenges in power distribution and management. Dendrite growth also relates to fundamental open problems in natural, non-equilibrium pattern formation [41, 42].

Experimental investigations of dendrite formation generally incorporate at least one imaging technique. Optical imaging is the most convenient and straightforward, and has a history dating back to Kepler's direct visual observations of snowflakes[42]. Current optical techniques incorporate CCD detectors and microscope objectives and allow *in situ* measurements in real time. When combined with interferometric methods, optical microscopy can also provide a determination of the local ionic (*e.g.* Cu^{2+}) concentration[43, 44]. However, as dendritic growth

and morphology is known to depend on atomic-scale surface kinetics[45], efforts to employ higher resolution imaging techniques in the study of this problem are ongoing.

Within an electrochemical context scanning electron microscopy (SEM) or transmission electron microscopy (TEM) has historically been available only as an *ex situ* diagnostic, because the typical electrolyte's vapor pressure is incompatible with the high vacuum environment required in a standard electron microscope. To circumvent this problem a low-vapor pressure electrolyte can be used in some cases. *In situ* observations of Li-ion battery electrodes have been performed in environmental SEMs using solid polymer or low-vapor pressure liquid electrolytes[46, 47]. Very recently lithium fiber growth has been observed in *in situ* TEM experiments on nanoscale lithium-ion batteries [48, 49]. These measurements were performed with an open architecture through the use of a low-vapor-pressure ionic liquid as the electrolyte. The electrolytes chosen for these experiments hold promise for future applications, but are not yet in use commercially.

The most common electrolyte solutions are based on solvents with high vapor pressures such as water, and thus require special measures for *in situ* TEM studies. The development of vacuum-tight, electron-transparent environmental cells for TEM has made high resolution, *in situ* electrochemical experiments possible [3, 36, 5, 7]. Recent achievements include the observation of galvanostatic growth of copper clusters[36] and dendrites[50] from acidified copper sulfate solution, and the atomic resolution imaging of lead sulfide nanoparticles grown *in situ*[15]. In this latter case the liquid cell included no externally-controlled electrodes; the nanoparticles were produced *via* the electron-beam induced decomposition of a multi-component surfactant solution of lead acetate and thioacetamide[15].

Here we report *in situ* TEM observations of the growth of crystalline lead structures on gold electrodes that are immersed in an aqueous solution of lead(II)

nitrate. We observe the shorting of electrodes *via* dendrite formation, and the reproducible growth and dissolution of dendrites at particular nucleation sites. We achieve spatial resolution limited by the 2 nm pixel size programmed for the scanning TEM (STEM) beam. Quantitative image analysis of the captured movies, when compared with the current-voltage data acquired simultaneously, shows a direct relation between the total charge passed through the circuit and the amount of lead deposited. This image analysis also proves capable of revealing the variation of the Pb^{2+} ionic concentration as a function of position and time as a nearby electrode is plated with or stripped of lead.

5.2   Experimental methods

Our fluid cell design and construction procedure has been described previously [11, 51], and has elements in common with those of others [3, 36, 5, 7, 50, 15]. The electrolyte solution is imaged in the TEM through two membranes fabricated from 19 nm of Si_3N_4 and 850 nm of SiO_2 grown on a 200 μm thick Si(100) wafer. A KOH etch reveals a 30 μm $\times$ 30 μm square window in a 2.1 mm $\times$ 2.1 mm silicon chip, and the membrane window is subsequently thinned by an HF vapor etch until it appears colorless when viewed in an optical microscope. An environmental chamber is constructed by epoxying together two such silicon chips back-to-back, with their electron-transparent membrane windows aligned. On one of the chips are polycrystalline gold electrodes patterned *via* optical lithography. A saturated solution of $Pb(NO_3)_2$ (99.5%, SPI-Chem) in deionized water is sealed between the two chips. Lead nitrate is chosen because its high solubility in water and large atomic number make it a good candidate solute for demonstrating the direct imaging of solvated ions. No spacer is used, but the surface corrugation from the gold electrodes ensures a chip spacing greater than 130 nm. This spacing places a lower limit on the fluid layer thickness.

The environmental cells are imaged using a biasing sample holder (Humming-bird Scientific) in an FEI Titan 80-300 TEM operated at 300 kV. Standard TEM, diffraction, and scanning TEM (STEM) modes are employed. STEM images are recorded with a Fischione Model 3000 annular dark field detector using a beam current of 57 pA, a convergence semi-angle of 11 mrad, and a detector inner angle of 35 mrad. All STEM images presented are 512 pixel × 512 pixel, with the exception of Figure 5.1f. The resolution in each image limited by the pixel size programmed for the STEM beam. The highest resolution data presented has a 2 nm pixel size. A Keithley 6430 Sub-Femtoamp Remote Sourcemeter is used to perform the *in situ* current-voltage measurements. The *in situ* current-voltage measurements are performed without a reference electrode. *Ex situ* cyclic voltammetry measurements use a macroscopic gold working electrode, an Ag/AgCl reference electrode, and a Pt foil or glassy carbon counter electrode. See the Supporting Information for the *ex situ* cyclic voltammogram. Digital image analysis is performed using the Labview software system (National Instruments).

5.3   Results and discussion

Lead's large atomic number ($Z = 82$) makes it ideal for generating dark field STEM contrast, since the cross section for scattering electrons to large angles increases rapidly with Z[52]. Lead(II) nitrate is very soluble in water at room temperature, dissolving according to:

$$Pb(NO_3)_2 \, (s) \rightarrow Pb^{2+} \, (aq) + 2NO_3^- \, (aq). \tag{5.1}$$
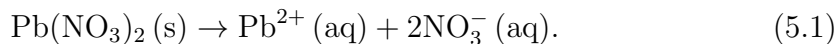
We work with a saturated (1.5 M) solution with excess, undissolved lead nitrate. Applying sufficient voltage across two electrodes in the solution leads to plating on the cathode,

$$Pb^{2+} + 2e^- \rightarrow Pb \, (s). \tag{5.2}$$
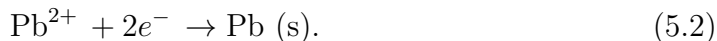
This reaction is reversible, so an electrode can serve as a source or a sink for Pb^{2+} ions. Regardless of whether the plating occurs in dendrites or in a compact layer, the products of eq 5.2 are crystalline with lead's characteristic face-centered cubic structure and atomic number density $n_{Pb} \simeq 33$ atoms/nm^3. Unsurprisingly, these products generate excellent contrast and are easily imaged.

The reactant Pb^{2+} ions of eq 5.2 also generate good contrast when present at number densities comparable to those of the saturated solution. Under this condition, in the absence of any applied electrical potential gradient, there are $\simeq 0.9$ Pb^{2+} ions/nm^3 and the number ratio of H_2O molecules to Pb^{2+} ions is ~ 34 to 1. During Pb deposition the ionic concentration of Pb^{2+} ions near the electrode decreases as the ions plate out of solution, and the STEM signal decreases. As will be shown below, while an electrode is stripping (*i.e.* when eq 5.2 is reversed and the Pb^{2+} ions are the products) the Pb^{2+} concentration nearby increases, leading to an increased STEM signal. Thus both Pb^{2+} concentration increases and decreases, whether induced by electrochemical reactions or applied electric potential gradients, can be visualized directly.

Before discussing the imaging of Pb^{2+} concentrations, however, we first describe the deposition product morphologies and growth behaviors observed on micrometer length scales. Figure 5.1 presents *in situ* STEM images illustrating how a compound dendritic structure can grow to short two electrodes in an electrochemical cell (see Supporting Information, Movie SM1). In this experiment the potential difference V applied between the working and counter electrodes is being ramped at 17 mV/s in a triangular waveform between ± 1.3 V, as in cyclic voltammetry (see Supporting Information for voltammogram). In the first frame (a), the working electrode is visible, it is at a potential $V = +1.24$ relative to the counter electrode, and the time derivative dV/dt is negative. In the frames that follow a tree-like dendritic formation enters the field of view (FOV) from the direction
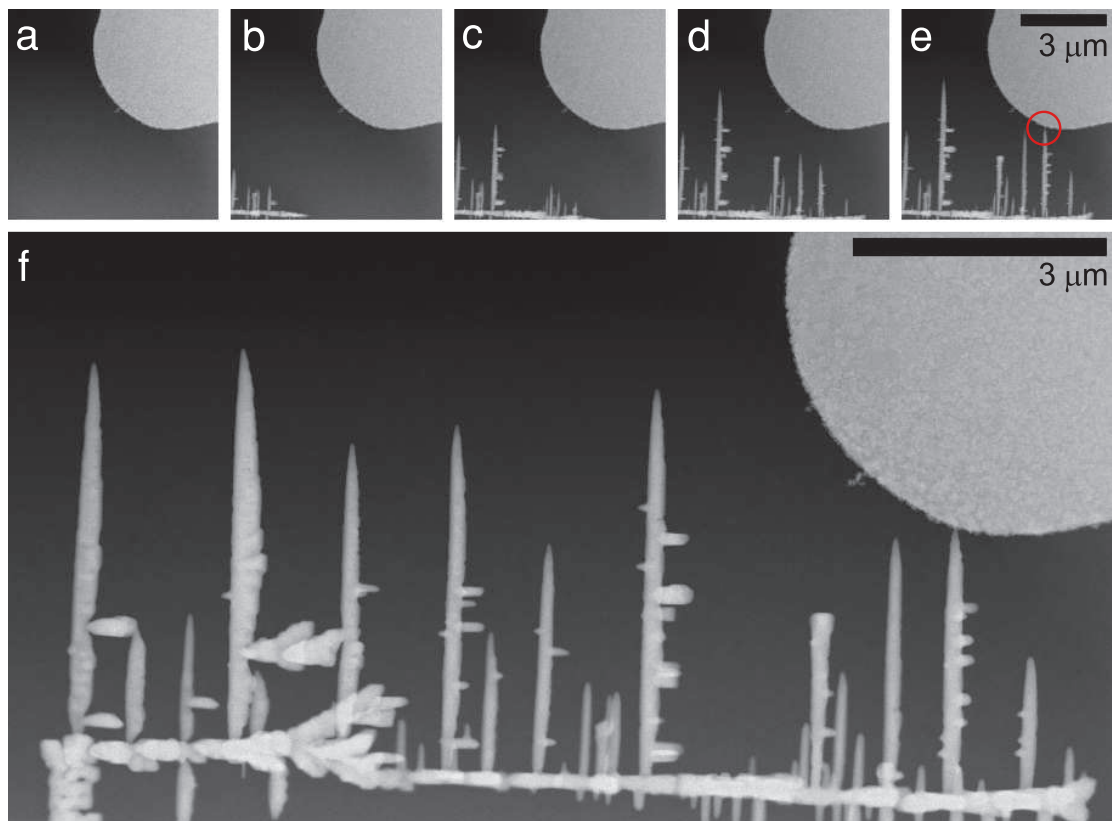
Figure 5.1: Time series of STEM images showing a dendritic forest that grows to short-circuit two electrodes (see also Supplementary Movie SM1). Images a–e are successive frames acquired 1.14 s apart, while the final image (f) was acquired 10 min after frame e. The working electrode, which consists of polycrystalline gold, appears in the upper right hand corner of each frame. A similar counter electrode is outside the field of view (FOV) in the direction of the opposing corner. The electrodes are shorted when contact is made at the point circled in frame e.

of the counter electrode and grows until it makes contact with the working electrode, shorting the cell. Coincident with the short-circuit the potential difference V changes from 1.17 V to 0.4 V, a value determined by the programmed current limit of 1 μA. The time from the first appearance of the dendritic forest until the short is established is 4.8 s, during which the dendrite's maximum growth rate is $\sim 2\,\mu$m/s.

From the time series it is clear that the dendrites grow from the tip and not the base. Two different growth morphologies are evident in this structure: a denser, flower-like morphology more common near the counter electrode, and a blade-like morphology such as the one that makes the final point contact with the working electrode. The formation is quasi-two-dimensional — in at least one place a blade appears to grow over or under a flower, but the main branches are longer than 10 μm, a length much greater than the fluid layer's thickness. In all cases branches with the blade-like morphology appear at right angles to each other. This observation is evidence of the critical role played by crystal surface energy anisotropies in determining the growth direction[53], as will be discussed later. Finally, branches extending off of the vertical segments are generally directed toward the working electrode and not away, indicating that the bias in the growth direction is local as well as global. This bias may be attributed to the electric potential and concentration gradients between the two electrodes.

Removing the dendritic structure proves to be difficult, which highlights the tenacity of the problems presented by dendrite formation. Figure 5.2 shows how the dendritic forest of Figure 5.1 alternately grows, shrinks, and then grows again as V is stepped from -0.3 V to 0.3 V and then to 1.0 V. See also Supporting Information, Movie SM2. Initially (frame a) the short of Figure 5.1 has been broken near the counter electrode with a 1 mA current. The remaining dendritic structure is thus at a cathodic potential and is plating lead. When the potential
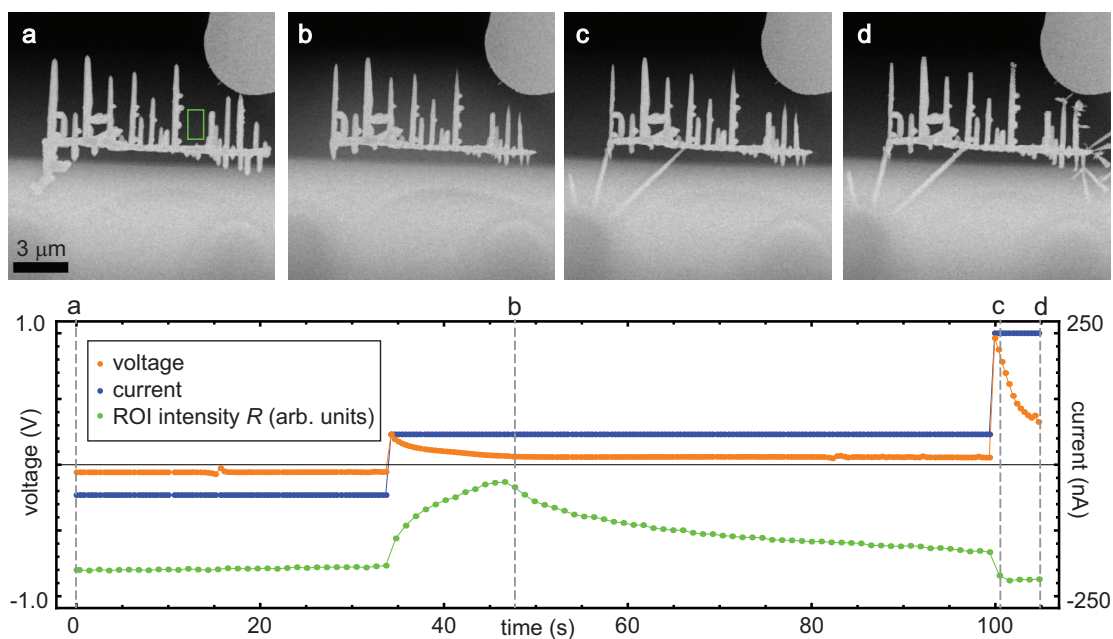
Figure 5.2: Time evolution (frames a–d) of the dendritic structure of Figure 5.1, and the corresponding applied electrical potential and measured electrical current (see also Supplementary Movie SM2). The increased brightness in the lower half of frames a–d is caused by the additional thickness of the membrane window near its edge. The intensity R from the ROI indicated by the green box in the first frame grows while the structure is stripping and decays thereafter, which demonstrates the STEM beam's sensitivity to the Pb^{2+} concentration.

is reversed the current surges and the structure begins stripping, which eventually causes the connection to the working electrode to be broken (frame b). Bringing V to an even more positive value initiates dendritic growth that begins at the counter electrode, reconnects to the remaining, previously isolated structure (frame c), and then re-establishes the short (frame d). The prevalence of right angles seen in the initial structure of Figure 5.1 is not evident in the structure's regrowth (Figure 5.2d), indicating that the second round of plating alters the previously regular geometric constraints on nucleation sites for new branches. Eventually the dendritic structure is almost completely removed with a voltage sequence customized in accordance with real time feedback provided by the *in situ* imaging.

The STEM signal is sensitive to the time variation of the ionic concentration. As captured by digital analysis of the indicated region of interest (ROI) in Figure 5.2, the stripping process is associated with a marked increase in the STEM signal R acquired from the regions neighboring the dendritic structure. This increase, which is readily apparent in the halo that appears in Figure 5.2b, starts to decay when the dendritic structure loses its connection to the working electrode (see also Movie SM2). A second current pulse and an associated dip in the signal from the ROI are coincident with the resumption of plating on the dendritic structure. The correlation between the gross morphological changes to the dendritic structure and the ROI signal indicates that the STEM beam experiences additional scattering from the Pb^{2+} ions in solution. The background concentration of these high-Z ions rises during stripping as ions are driven into solution, and drops during plating as ions deposit out of solution (or when the effective size of the stripping electrode changes due to a disconnection event). The impressive size of the contrast changes (more than 20%) produced here suggests that other, lower-Z solutes can also be visualized with this technique.

Dendrites can be grown and shrunk controllably and repeatedly with step-like
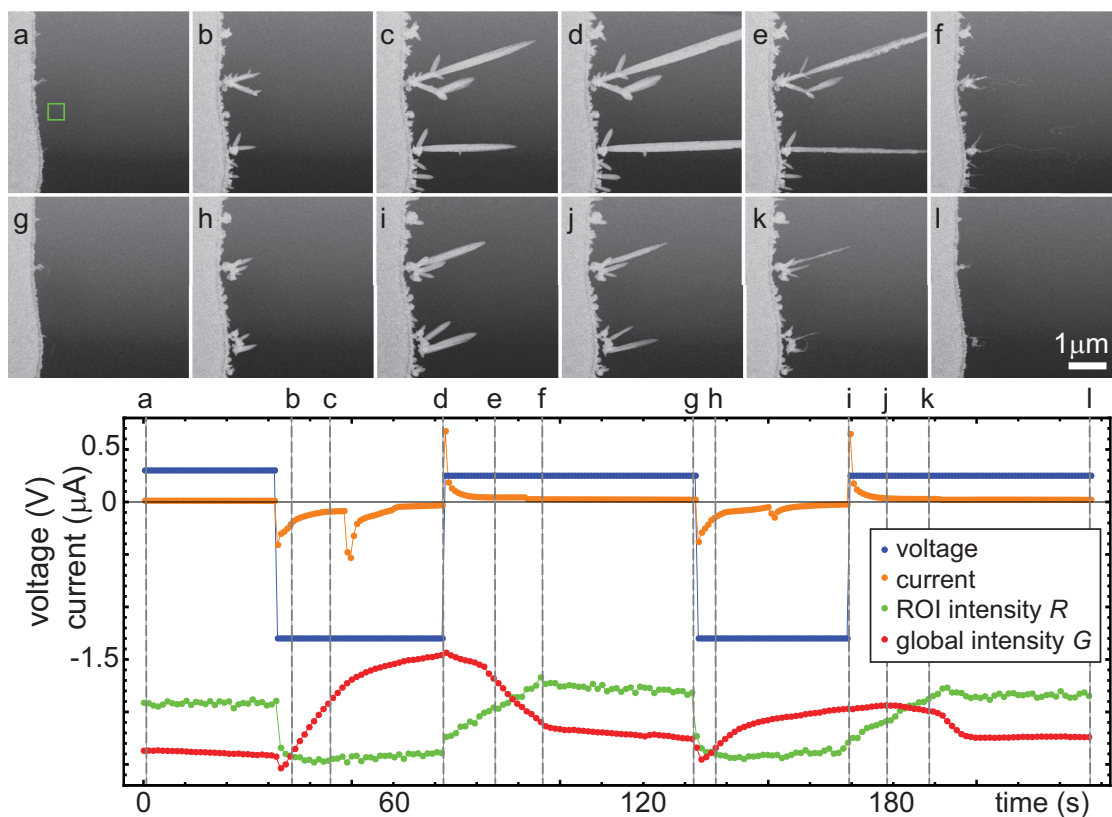
Figure 5.3: Repeated dendrite growth and collapse (see also Supplementary Movie SM3). The rows of frames a–f and g–l are taken from consecutive cycles, with the individual frame times indicated on the current-voltage plot below. Certain nucleation sites consistently nucleate larger dendrites. Also shown on the current-voltage plot are the STEM intensity R from the ROI indicated by the green box in frame a, and the global intensity G over the entire FOV as a function of time. Both have been rescaled and offset for display purposes.

changes between potentials with alternating polarities. Figure 5.3 shows images from two consecutive full cycles (out of a sequence of 43 — see Supporting Information, Movie SM3 for a partial sequence) of lead dendrite growth and collapse on a gold electrode. A thin (~ 100 nm) layer, shown to be polycrystalline lead *via* dark-field TEM imaging, is evident in all of the images and is not present on a pristine electrode. Small dendritic structures coat this layer almost uniformly during the growth phase, but the largest dendrites repeatedly grow from special, protruding sites that do not completely disappear, even at the end of the stripping phase (frames a, g, and l). Dendritic growth is again seen to occur mostly at the tips. During the stripping phase the longest dendrites collapse first, but material loss is more uniformly distributed along a dendrite's length. This lack of time symmetry leads to the wispy structures seen in, *e.g.* frames f and k, and in some cases causes a dendrite remnant to become detached from the electrode that initiated its formation. At their thinnest these wisps are $\lesssim 10$ nm across.

As has been seen previously with *ex situ* SEM measurements[54], the size and aspect ratio of the dendrites can be altered by adjusting the cycling waveform. We observe longer, narrower dendrites appearing when the cycling frequency is low. Alternatively, if the stripping is interrupted and left incomplete, the subsequent plating phase shows a wider array of dendritic branch growth directions, with blades nucleating throughout the structures that remain from the previous cycle.

The voltage steps responsible for the reproducible dendrite growth have associated current pulses that decay over some tens of seconds, as shown in Figure 5.3. The secondary cathodic current peaks that occur ~ 20 s after the voltage switches from 0.3 V to -1.3 V are not correlated with any visible event, and thus may correspond to chemistry outside the FOV. The same plot also shows an ROI intensity R indicative of the background Pb^{2+} concentration, and the global scattered STEM intensity G over the entire FOV. This latter statistic provides a measure of the total amount of lead deposition in the FOV; it rises while the dendrites are growing

and falls as they collapse. Comparing the ROI intensity to the global intensity, it is clear that within a single frame of the potential change the plating process has scavenged most of the available Pb^{2+} ions in the FOV, leaving the ROI at a decreased, constant level set by the rate of mass transport towards the electrode. The promptness of the collapse of the local Pb^{2+} concentration upon the initiation of plating is also reflected in a small dip in G that occurs before the dendrites start to grow — evidently the prompt loss of signal from Pb^{2+} ions is not entirely compensated by the gain from plated Pb, when averaged over the entire FOV. During stripping the ROI intensity steadily increases until the dendrites are gone, at which point it levels off or decreases slightly as the ions diffuse away.

To determine the chemical composition of the electrodeposits we have performed *ex situ* cyclic voltammetry control experiments and *in situ* select-area electron diffraction (SAED). The cyclic voltammetry experiments confirm the reversibility of the Pb plating and that PbO is not formed directly at the potentials reached in the *in situ* TEM experiments (see Supporting Information). The absence of PbO deposits is consistent with previous studies that found that oxide only forms after drying in an oxygenated environment[55]. The presence of solid Pb is confirmed with *in situ* electron diffraction. Figure 5.4 shows a TEM-mode micrograph of several blade-like dendrites with uniform edges and clear faceting. SAED on one of the dendrites reveals that it is a single crystal of lead (fcc, lattice parameter $a = 4.95$ Å).

In addition to verifying their chemical composition, the SAED gives important information on the growth dynamics of the dendrites. The dendrite highlighted in Figure 5.4 has its primary growth direction (blade length) along the [100] crystal axis and its secondary growth direction (blade width) along the [010] crystal axis. These observations together with the observed prevalence of right-angles in the large-scale morphology of compound dendritic structures (*e.g.* the tertiary
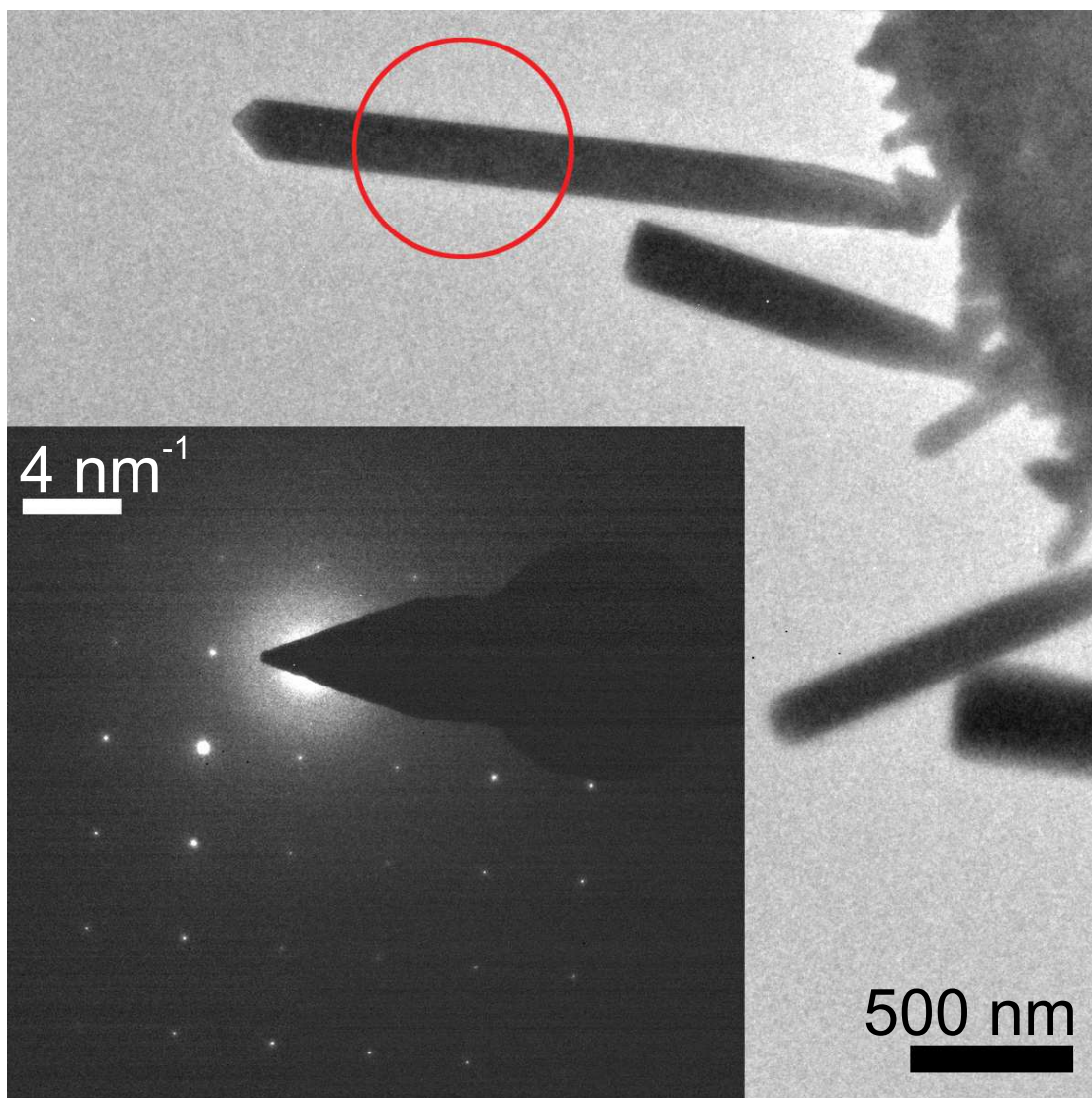
Figure 5.4: TEM image and associated *in situ* SAED of a blade-like dendrite immersed in the growth solution. The diffraction pattern (inset) acquired from the selected region (red circle) shows that the dendrite is lead, a single crystal, and oriented with its growth axis in the [100] direction.

dendrite of Figure 5.1) indicate that crystalline anisotropy plays a dominant role in determining the preferred growth directions. Previously[53] it has been noted that the preferred growth directions of Pb dendrites are $\langle 100 \rangle$ for high current densities and $\langle 110 \rangle$ for low current densities, with the crossover occurring near 1 A/cm^2. While we see examples of the 60° angles associated with $\langle 110 \rangle$ growth (*e.g.* Figure 5.3c), the 90° morphology is far more common. Thus the dendrite growth is occurring closer to the high current density regime.

Combining traditional electrochemical transport measurements with simultaneous *in situ* STEM imaging shows that the two techniques return complementary information. Figure 5.5 presents STEM micrographs acquired as a gold electrode goes through two cycles of Pb plating and stripping. It also shows plots that synchronize the results of a frame-by-frame digital image analysis with the electrical transport measurements. Here the potential is varying smoothly between ±1.3 V at 17 mV/s, a moderate rate that more often results in the deposition of a compact lead layer, as opposed to the dendrites that can be produced with rapid potential changes. (For more information see Figure S1 in the Supporting Information and Ref. 19.) The plating initiates at a potential of −0.2 V and peaks near −0.5 V, as indicated by the cathodic electrical current. A second cathodic current peak begins around −1.1 V and is still increasing in magnitude when the voltage ramp reverses direction.

The STEM images a–l and the corresponding difference images show features that can be qualitatively matched with the time evolution of the electrical current. For instance, in the first half-cycle most of the plating occurs between frame a and frame b. A second, more subtle stage of growth, representing ~ 20 nm of Pb, occurs between frames b and c. This additional plating is coincident with the second, smaller, cathodic current peak beginning around −1.1 V. The difference images b-a and c-b show the two distinct growth phases by highlighting the ad-
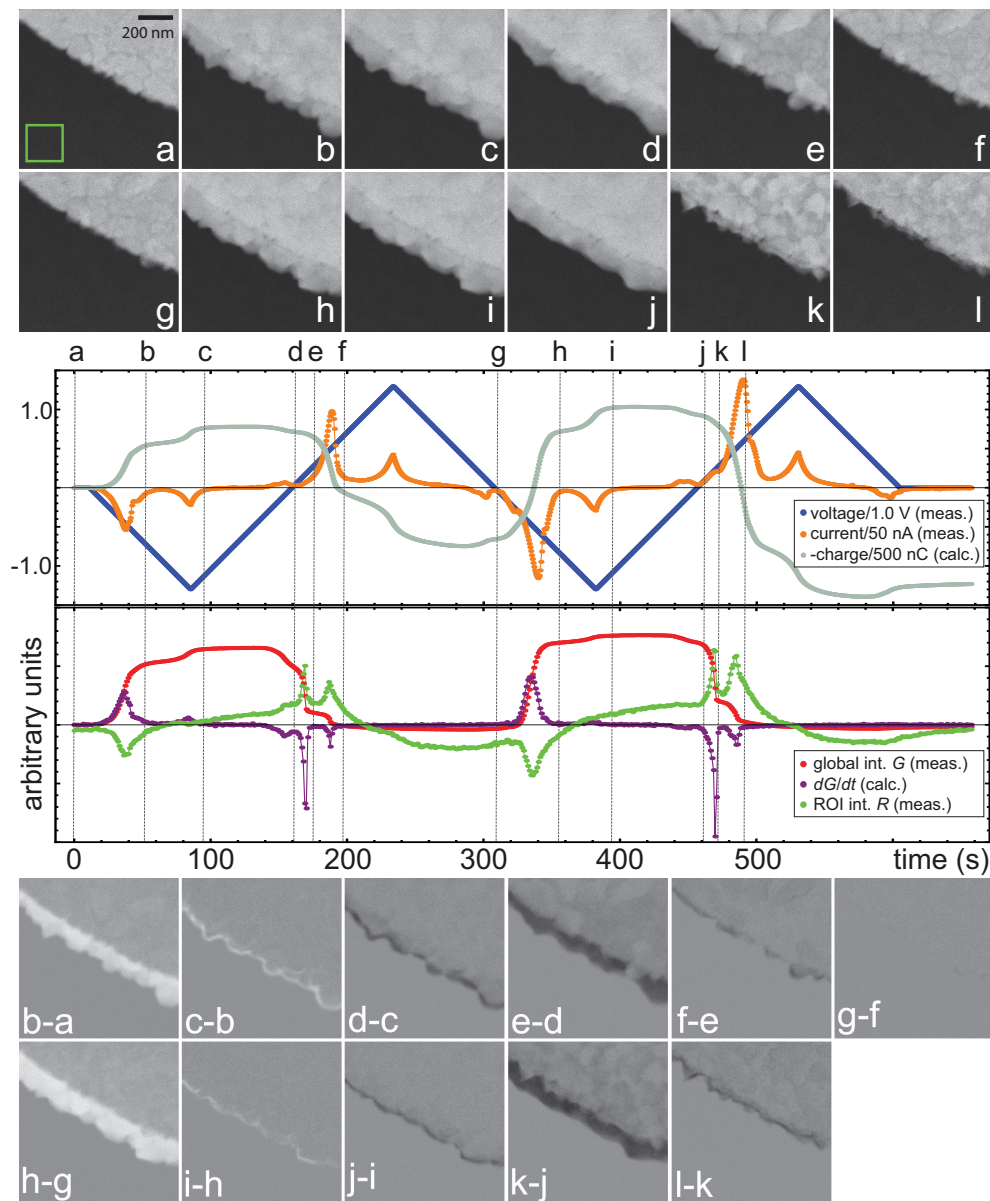
Figure 5.5: Triangle wave deposition at 17 mV/s . (top) Frames a–l show the growth and stripping of a $\sim$ 150 nm thick lead layer on an initially pristine (frame a) polycrystalline gold electrode through two complete cycles of cyclic voltammetry. The electrical parameters V, I, and Q show agreeable correlations with the image parameters G, dG/dt, and R. (bottom) Plated layer thickness changes are highlighted in images constructed by computing the difference between the indicated frames.

dition of new material between the displayed frames. Near the end of the first half-cycle the current becomes positive while the voltage is still negative; this reversal is reflected in the slight thinning of the plated layer between frames c and d and highlighted in the difference image d-c. Most of the stripping from the portion of the electrode shown in Figure 5.5 occurs between frames d and e. Finally, after a full cycle (frame g) the electrode has returned to a near approximation of its initial condition (frame a). Because the stripping is not complete the electrode's effective surface area is slightly larger, which may help explain the steady increase in the size of the electrical current peaks throughout the course of this dataset.

Along with the voltage V and the current I, the negative of the charge $Q = \int I dt$ is plotted in Figure 5.5, where the integration has been performed numerically with a Riemann sum. Digital analysis of the STEM images returns statistics that can be directly compared with the measured I and calculated Q. As shown in the lower part of the plot of Figure 5.5, the global scattered STEM intensity G, which is primarily determined by the thickness of the plated layer, faithfully reproduces the main features of the curve describing the charge transferred between the electrodes during the negative potential half-cycles. During the positive half-cycles plating is occurring on the electrode outside the FOV, and thus G is insensitive to the corresponding charge transfer.

In addition to G, Figure 5.5 shows the time derivative dG/dt and the scattered intensity R from an ROI away from the electrode. The numerical derivative has been evaluated using a two-point difference quotient, *i.e.* without smoothing. When the electrode is plating rapidly dG/dt becomes large and positive while R becomes large and negative with a nearly identical time signature. This correspondence indicates that the background concentration of Pb^{2+} (reflected in R) drops as the ions plate onto the electrode (reflected in G and its time derivative). These signals also mirror the behavior of the electrical current I.

For stripping the effects are similar, with two important differences. First, the

peaks change sign, as expected. Second, the single distinct peak appearing in I is split into two peaks in dG/dt and R. This split can be understood by noting that the electrical transport measurements necessarily average over the entirety of both electrodes. The peak in I is broadened by the position variation of the ionic concentrations across the electrodes, while the derivative dG/dt reflects only the local chemistry in the FOV. The ionic concentration measured directly by R, while dominated by the local chemistry, shows some broadening due to the effects of diffusion. However, in both cases the *in situ* STEM imaging clearly resolves two separate peaks where the electrical transport measurement detects only one. Because STEM imaging of the deposition products and reactants performs a prompt spatial average that is local and controlled in comparison to the blind current-voltage measurement, it may be able to improve on the resolution of more traditional, impedance-based spectroscopic techniques.

Each peak shown in Figure 5.5 has not been identified with a specific chemical reaction. For instance, the small cathodic peak in I at -1.1 V is accompanied by continued Pb plating, as seen in G and in the difference images c-b and i-h. However, this second peak also implies the appearance of new reactions at this potential. Hydrogen evolution is one possibility, although the gas would have to be forming outside the FOV or going straight into solution, since bubble formation would give obvious contrast.[11]

Under certain circumstances the *in situ* STEM imaging can detect the variation in the Pb^{2+} ionic concentration with millisecond time resolution. Simple metal cations in aqueous solution at room temperature typically[56] have diffusion constants D of order 10^{-9} m^2/s, which implies a displacement of 30 μm within a single ~ 1 s frame time. However, the line-to-line scan time of the electron beam is substantially shorter (2.2 ms for 512 pixel $\times$ 512 pixel images acquired with a frame period of 1.14 s), allowing time-resolved observation of diffusion phenomena on sub-micrometer length scales. Figure 5.6 shows two instances of the time evolu-

64

tion of the Pb^{2+} ionic concentration, where this evolution is revealed by changing the potential on the imaged electrode shortly after the frame scan has initiated. The images a0–b0 represent the difference of two successive frames, which removes time-independent intensity variations such as those caused by a gradient in the membrane thickness. Here data captured before the potential change, shown near the top of the images a0–b0, is uniformly gray with slightly more noise in the electrode due to the larger signal there.

Once the potential reverses polarity in a0, a light region and a dark region appear at the electrode boundary, with the former indicating a layer of plated lead and the latter a concomitant drop in the Pb^{2+} concentration nearby. Moving down the frame, which corresponds to moving forward in time, we see both regions expand to the right, with the plated layer growing to ~ 100 nm in thickness and the Pb^{2+}-depleted region expanding out to the edge of the FOV 4 μm away. The plated layer is not completely uniform, but shows 2–3 locations with incipient dendrites. At the bottom of the frame the Pb^{2+}-depleted region has retracted slightly from its maximum extent, probably because the electrode begins to curve away from the FOV just past the lower boundary.

Frame b0 of Figure 5.6 shows the time-reversal of the processes seen in frame a0: the electrode is stripping and the Pb^{2+} concentration jumps locally. This particular instance of stripping has been chosen for display because the collapsing dendrites have relatively small aspect ratios and terminate less than 900 nm away from the electrode. Thus the electrode boundary more closely approximates a spatially uniform Pb^{2+} source. As in a0, once initiated the changes spread gradually with increasing distance towards the bottom of the frame b0, showing clear evidence of the time evolution of both the plated layer thickness and the ionic concentration.

To estimate the effective diffusion constant of the Pb^{2+} ions we take our en-
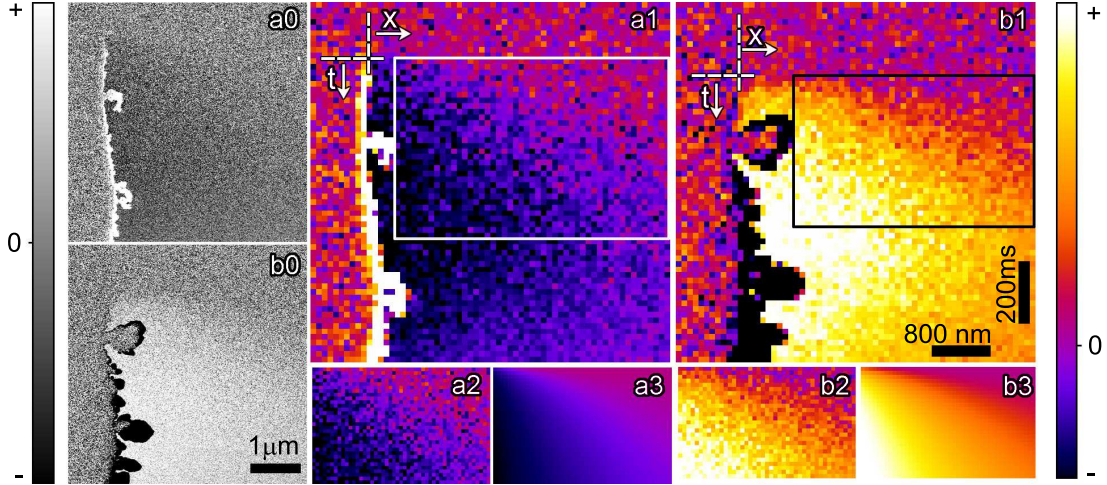
Figure 5.6: Time evolution of the Pb^{2+} ionic concentration. Images a0 and b0 are constructed by subtracting two consecutive 1.14 s frames in the Movie SM3 (see also Figure 5.3), giving lighter or darker regions where the intensity increases or decreases respectively. The STEM beam is scanning from top to bottom. During the acquisition of image a0 (b0) the potential V on the electrode shown switches polarity and begins plating (stripping) lead, which creates the white (black) regions on the electrode boundary. Images a1 and b1 depict the same events with 8×8 spatial binning and rescaling of the intensities to enhance contrast. Data (a2–b2) extracted from the boxed regions in a1–b1 is fit to eq 5.3 with t increasing down and x to the right. The best fits (a3–b3) return $D = 1.3$ and 1.5×10^{-11} m^2/s respectively.

vironmental cell to be strictly two-dimensional, which neglects, for instance, the plating and stripping occurring on top of the electrode (the electrode is not opaque to the STEM beam and shows intensity variation in phase with the deposition cycling). We also neglect the migration current, which may not be small compared to the diffusion current, and the spatial inhomogeneities that occur along the electrode surface. Finally, we choose regions that are more than one radius of curvature away from the electrode corner (not visible) for detailed analysis. With these approximations we can model the ionic concentration n in the selected regions of a1–b1 using the one-dimensional, time-dependent diffusion equation $\partial n/\partial t = D\,\partial^2 n/\partial x^2$, where the spatial coordinate x increases from $x = 0$ to the right and the time t increases from $t = 0$ moving downward in frames a2–b2 of Figure 5.6. The appropriate solution $n(x, t)$ to this diffusion equation is given by:

$$\frac{n(x,t) - n_0}{n_\infty - n_0} = \mathrm{erf}\left(x/2\sqrt{Dt}\right), \qquad (5.3)$$

where n_∞ is the background ionic concentration at large distances from the electrode and erf is the error function. We have enforced the boundary condition that the Pb^{2+} concentration at the electrode $n(x = 0, t)$ goes from n_∞ to n_0 at $t = 0$.

Applied to the difference data, eq 5.3 gives a satisfactory qualitative description (Figure 5.6, a3–b3) of the concentration plumes observed during plating and stripping. To perform the fit we have assumed that changes in the STEM intensity are proportional to $n(x, t)$ and allowed for two adjustable parameters: D and a term $\propto (n_\infty - n_0)$. We find the magnitude of the diffusion constant D to be in the range 1–2×10^{-11} m^2/s for both plating and stripping ($N = 56$), which helps explain how the millisecond time resolution afforded by STEM imaging is sufficient to resolve concentration variations propagating over a few hundred nanometers.

Previous investigations have found that, in the limit of infinite dilution, Pb^{2+} has a diffusion constant $D_0 = 9.4 \times 10^{-10}$ m^2/s [57], and that this value decreases with increasing concentration to 2.7×10^{-10} m^2/s for 48 mM solution[58].

The theory of diffusion in concentrated electrolyte solutions such as the one used here is not entirely developed [59]. The small effective diffusion constants and correspondingly long time constants (see, *e.g.* Figure 5.2) observed may reflect ion-ion interactions in the concentrated solution, structuring of the liquid near the charged electrode, hindering of free diffusion by the membrane surface, and the inadequacy of our simplifying assumptions[60, 61, 62]. Future experiments are planned to enable a more quantitative analysis.

5.4 Conclusion

Here we have presented *in situ* STEM observations of the electro-deposition and stripping of lead on polycrystalline gold electrodes from a 1.5 M aqueous solution of lead nitrate. Lead can be induced to deposit in a compact coating or as dendrites, with the latter morphology being more likely with abrupt potential changes. Individual dendrites are crystalline and grow from their tips most commonly along a $\langle 100 \rangle$ crystal axis. The magnitude of the current passed through the electrochemical cell shows excellent correlation with the observed rate of Pb deposition. The discrepancies observed arise because the electrical transport measurement is sensitive to chemical reactions occurring over an area 100 times larger than the STEM FOV. Such averaging effectively reduces the spectroscopic resolution of the transport measurement in comparison to the STEM observations. Finally, STEM imaging can detect variations in the local Pb^{2+} concentration with sub-second and sub-micrometer temporal and spatial resolution respectively. Because the contrast changes generated by Pb^{2+} are so large and easily detected, we expect that it will be possible to generalize this technique to visualize lighter and less-soluble solutes. With its ability to provide real-time, high-resolution images of both the reactants and the products in electrochemical processes, *in situ* fluid cell STEM promises to become a powerful tool for solving dendrite formation

problems in energy storage devices.

CHAPTER 6

Graphite intercalation compound formation

6.1 Introduction

Graphite intercalation compounds are formed when an atomic or molecular species is inserted between layers of a graphite host. The strong intraplane bonds keep each individual layer intact, and the intercalant is only present between layers which are held together with the weaker interplane bonds. There are a large number of different species that intercalate graphite, and they display a wide range of new electrical, thermal, and magnetic properties compared with the parent materials. As a result there has been intense research in the area of graphite intercalation compounds[63].

The number of graphite layers between each intercalant layer determines the intercalation stage, as demonstrated in Figure 6.1. The stage of the intercalation compound determines its material properties. Given the picture in Figure 6.1 the transition from, for instance, stage 7 to stage 6 would require an entire intercalant layer to exit the host material, and then reinsert itself one layer below. This model may seem rather unphysical given the changes required to change stage in bulk graphite where a 1 mm thick piece is 3 million layers thick. The Daumas-Herold model of staging offers an alternative that allows smooth transitions between stages[64]. In this model a pure stage consists of intercalant domains, where each intercalation domain permeates the direction along the c-axis of the compound, but in the lateral direction each domain is offset from the next by one layer. For

pure stage 3 this is illustrated in Figure 6.1.

There is evidence for domains predicted by the Daumas-Herold intercalation model[65]. The imaging of domains has been performed with techniques such as scanning tunneling and and scanning ion microscopy, which are only sensitive to the surface. Here, we use *in situ* transmission electron to visualize the effects of domain presence in intercalated graphite by the corresponding structural changes, and monitor the time dependence throughout the staging process. Repeated intercalation and deintercalation cycling of the graphite sheet shows structural changes that persist, and evolve over time. This demonstrates a new platform to study intercalation compounds in their native environment that are not air or vacuum stable.

6.2 Experimental methods

Graphite bisulfate was one of the first graphite intercalation compounds discovered and has been extensively studied[66, 67, 68, 69, 70, 71, 72, 73]. Graphite bisulfate is formed upon intercalation with sulfuric acid. Stage 1 graphite bisulfate has the formula $C_{24}^+ \cdot HSO_4^- \cdot 2.5H_2SO_4$. Sulfuric acid does not spontaneously intercalate into graphite as the reaction has a positive Gibbs free energy[68]. We control the intercalation process electrochemically by tuning the potential of the graphite. The intercalation process is highly reversible, and sulfuric acid is relatively stable under the electron beam making it a model system for us to study intercalation with the TEM.

The graphite is an exfoliated single flake. It has a typical size of approximately 100 μm^2 and is between 20 and 100 layers thick. To isolate the single flakes we use the Scotch tape method commonly used to transfer graphene sheets[74]. In brief, graphite is exfoliated using Scotch tape and then pressed on a silicon chip with 80 nm of SiO$_2$. The chip is coated with a thin layer of PMMA and the
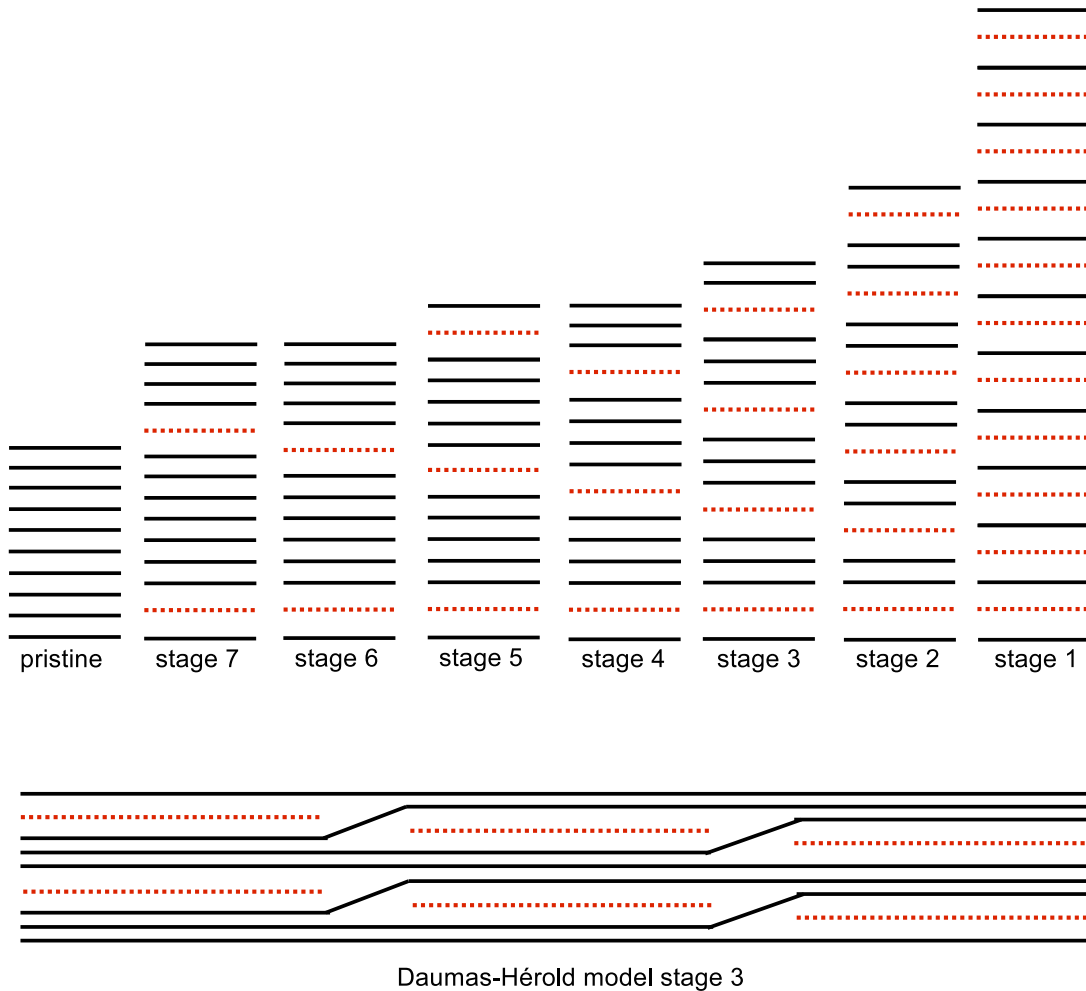
Figure 6.1: (top) Illustration of intercalant stages in graphite. For stage n, there are n graphitic layers (black lines) between each intercalant layer (red dotted lines). (bottom) Daumas-Herold model for stage 3 intercalation. The intercalant is broken up into domains that do not extend laterally across the graphite crystal. Instead, neighboring domains are offset by a layer.

oxide is etched away with sodium hydroxide leaving the graphite flake attached to the PMMA and floating in the etching solution. It is then transfered to another silicon chip which has platinum electrodes that meet on a 20 nm thick Si_3N_4 electron transparent window. The graphite flake is aligned on one of the platinum electrodes and allowed to dry, the PMMA is subsequently removed with acetone leaving the pristine graphite flake over the electron transparent window and electrically connected to one of the platinum leads. The other platinum leads serve as the counter and reference electrodes in the electrochemical cell. An optical picture of a transfered graphite flake is shown in Figure 6.2.

A small drop of sulfuric then placed on the electron transparent window. Another silicon chip with an electron transparent window is pressed on top of the chip with the graphite flake. The two windows are aligned, and epoxy is applied to the sides of the chips, creating a vacuum tight seal.

Once the electrochemical cell is complete the sample is ready to be imaged in the TEM. We use a Gamry 600 Potentiostat to initiate intercalation by controlling the electrochemical potential of the graphite.

If the electron beam is incident on the graphite crystal parallel to the c-axis the diffraction pattern will have six-fold rotational symmetry, which reflect the symmetry of the honeycomb lattice, the plane that is normal to the beam. However, due to the curvature of the Ewald sphere this is not the ideal imaging condition to maximize any particular peak intensity. The amount by which the Ewald sphere misses a reciprocal lattice point is the excitation error. The excitation error can be remove by tilting the graphite lattice slightly with respect to the optical axis so the diffraction condition $\Delta k = G$ is exactly met. In TEM mode this is known as the two-beam condition and is used for forming dark field images with sign signal. Here we operate in STEM mode and choose the ADF detector inner and outer angles such that only the diffraction peaks closest to the direct beam are
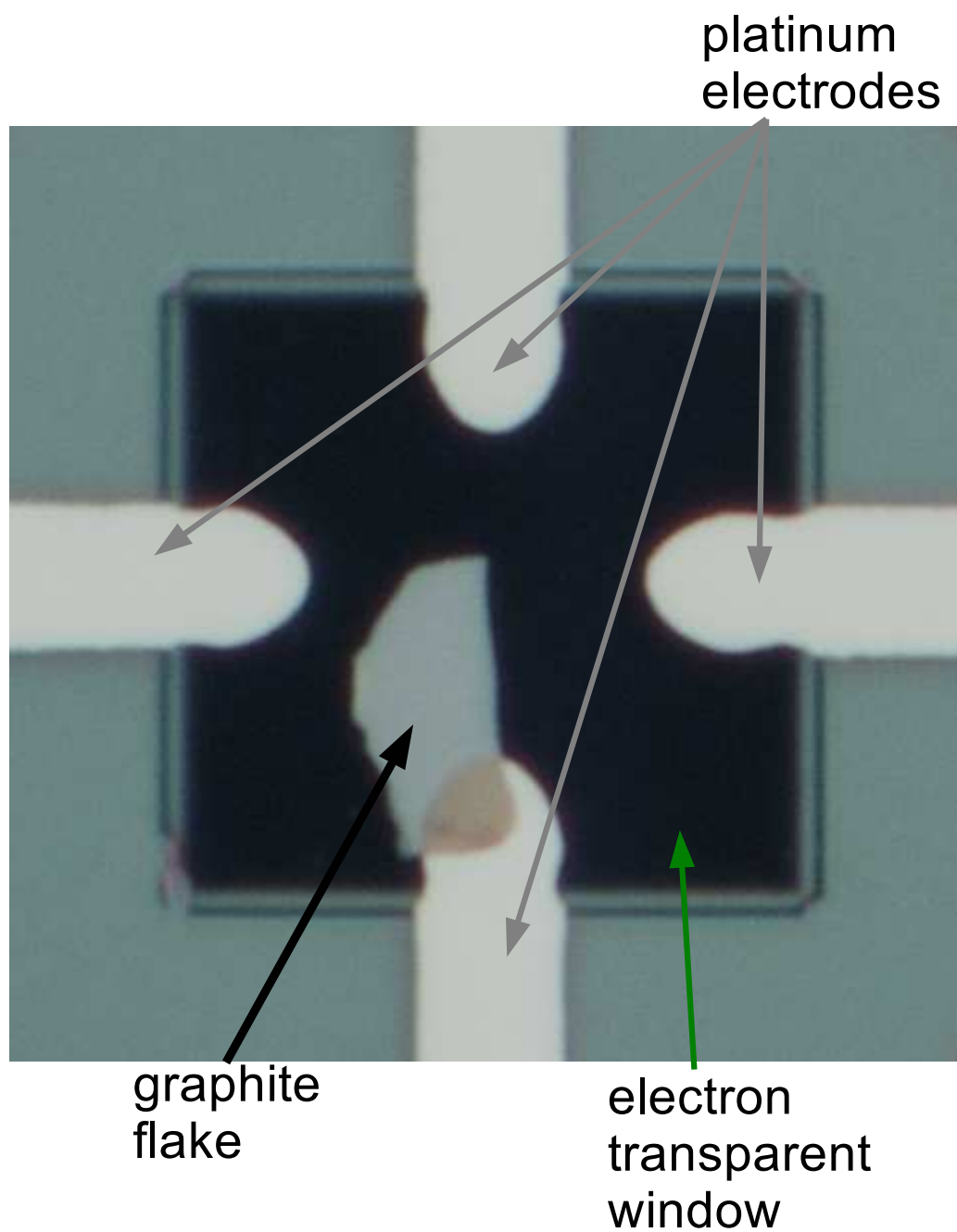
Figure 6.2: Optical image of a transfered graphite flake onto a preprocessed silicon chip patterned with platinum electrodes and an electron transparent window. The window is 30 μm on a side and the graphite flake is approximately 100 layers thick.
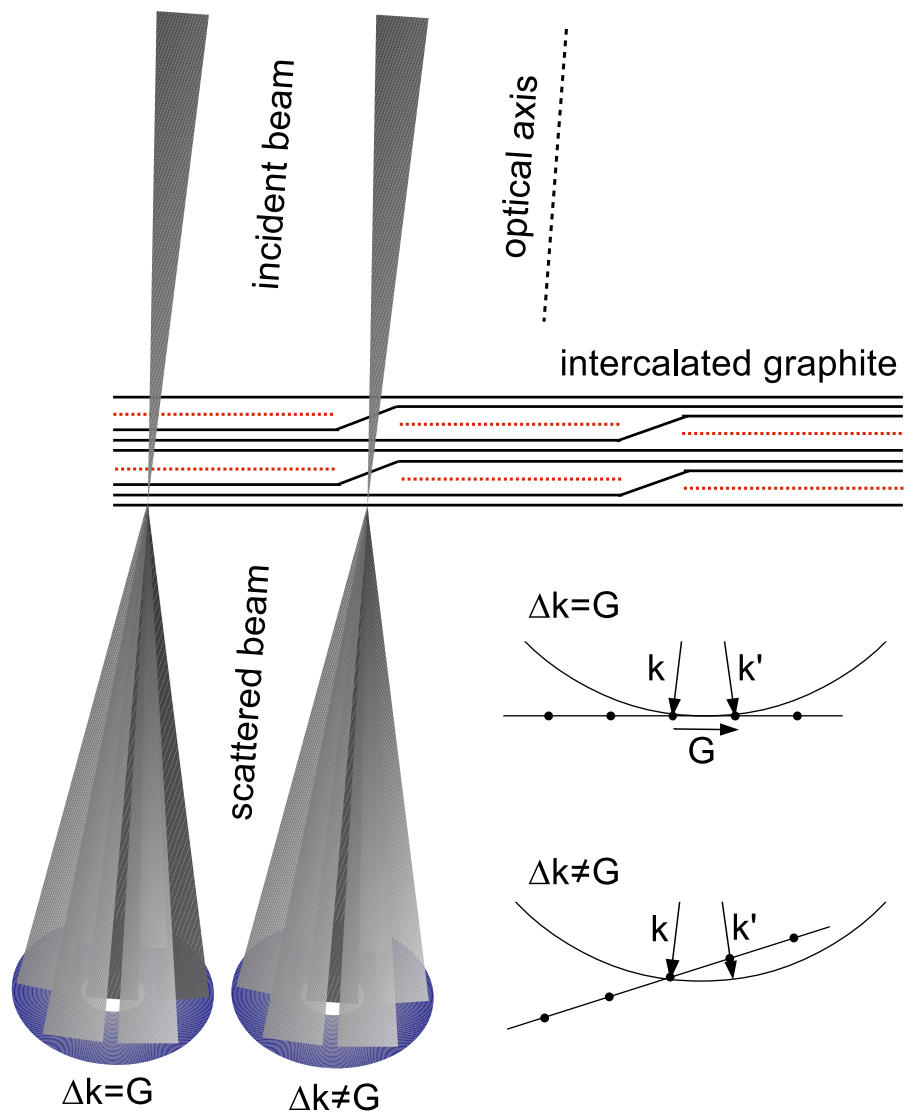
Figure 6.3: Schematic of illumination conditions set to maximize diffraction contrast in STEM. By slightly tilting the graphite lattice with respect to the incident beam, one peak is enhanced by eliminating the excitation error and exactly meeting the diffraction condition $\Delta k = G$. This produces a bright pixel in the ADF image. At the edges of domains in the graphite lattice tilts slightly, and we lose the peak enhancement as the excitation error is nonzero, resulting in a dark pixel.

incident on the detector. Thus the contrast is generated by the peak where the diffraction condition is met in an analogous way to dark field TEM and readily interpretable. This concept is illustrated in Figure 6.3, and shows how curvature in the graphite lattice caused by the presence of domains can be detected.

There is a second reason this imaging condition is desirable, which stems from the change in stacking that occurs when graphite intercalates. Each graphite layer forms a honeycomb lattice where the carbon-carbon bond length $\delta = 0.142$ nm. The graphite layers then stack on top of one another with an interlayer spacing of 0.335 nm in either the AA or AB configuration. In AA stacking each layer is stacked directly on top of the next. In AB stacking the second graphite layer is offset by δ from the sheet below, and the third sheet matches the stacking of the first. Figure 6.4 illustrates this[75]. Natural graphite stacks according to AB[74]. When graphite intercalates, the graphite layers on either side of the intercalant (which were initially AB) shift to AA stacking. This can result in, for instance, the sequence ABAB-BCBC-CACA-ABAB... for stage 4 intercalation, where AC is the mirror image of AB. Thus for stage 1 there is an AA stacked graphite lattice with an interlayer spacing equal to the size of the intercalant layer. This has dramatic consequences on the diffraction intensity of the first order peaks we use to generate the contrast.

Using kinematical scattering theory we have shown the number of electrons scattered into a particular peak of thin graphite is given by:

$$N_{\text{peak}} = \frac{16}{27} \frac{I\tau}{e} \left(\frac{Z\gamma\lambda}{a_B} \right)^2 |\mathcal{S}_b(v_1, v_2)|^2 \frac{e^{-2W}}{\delta^4 \left(\mu^2 + \Delta\mathbf{k}^2 \right)^2}. \tag{6.1}$$

where I is the electron beam current, τ is exposure time, e is the electron charge, Z is carbon's atomic number, γ is Lorentz factor, λ is the electron wavelength, a_B is the Bohr radius, $\mathcal{S}_b(v_1, v_2)$ is the structure factor, W is the Debye Waller factor, δ as before is the carbon-carbon bond length, and μ is the inverse screening length[74]. The only dependence on the stacking of the graphite sheet comes from
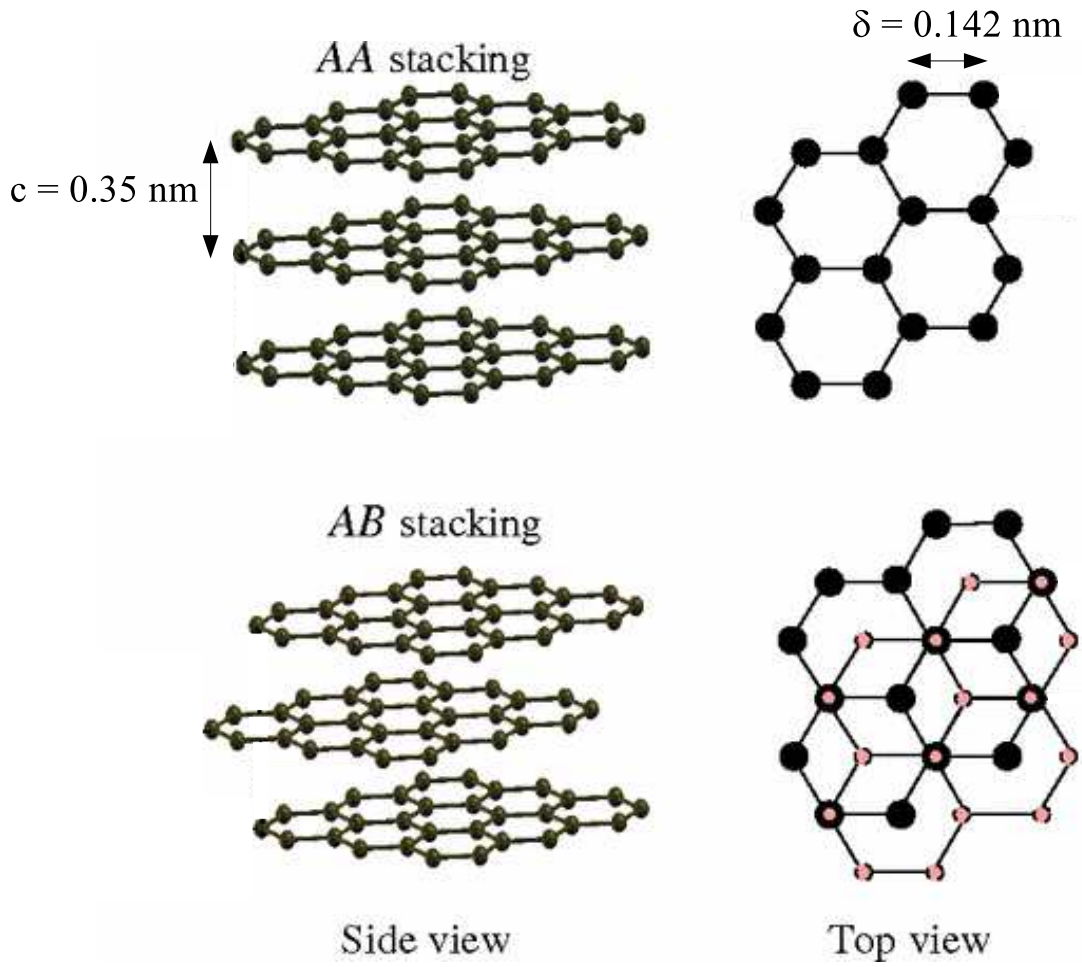
Figure 6.4: Graphite lattice. Each graphite layer forms a honeycomb lattice (hexagonal lattice with a two atom basis), which then stacks for form the graphite lattice. Two options for the stacking are shown, AA and AB.

Stacking	Condition	weak order	strong order
AA	n.a.	N^2	
AB	N is odd	$(N^2+3)/4$	
AB	N is even	$N^2/4$	$4N^2$
ABC	N mod 3 $\neq$ 0	1	
ABC	N mod 3 = 0	0	

Table 6.1: Summary of $|\mathcal{S}_b|^2$, the square of the relative structure factor, for various graphene stackings. The designations 'weak' (*e.g.* 1$^{\text{st}}$) and 'strong' (*e.g.* 2$^{\text{nd}}$) order are shorthand for $(v_1 + v_2) \mod 3 \neq 0$ and $= 0$ respectively.

the structure factor. Table 6.1 summarizes the different values the structure factor takes depending on the stacking, and the particular peak in the diffraction pattern. For the first order peaks which are 'weak' order, there is a factor of 4 increase in the number of electrons scattered into them. Thus, when the graphite reaches stage 1 the signal should increase by a factor of 4 relative to the unintercalated state when we choose just the first order peaks to be incident on the ADF detector.

There are four conditions that need to be met in order for the illumination to be as illustrated in Figure 6.3. They are:

$$\theta_{inner} > \alpha, \tag{6.2}$$

$$\theta_1 - \alpha > \theta_{inner}, \tag{6.3}$$

$$\theta_1 + \alpha < \theta_{outer}, \tag{6.4}$$

$$\theta_2 - \alpha > \theta_{outer}. \tag{6.5}$$

θ_{inner} and θ_{outer} are the detector inner and outer angles respectively, θ_1 and θ_2 are the first and second order diffraction peak angles in graphite, and α is the electron beam convergence angle. Inequality 6.2 ensures the detector does not pick up any of the direct beam. Inequality 6.3 ensures the innermost part of the 1st order peak falls on the detector. Inequality 6.4 ensures the outermost part of the 1st order peak falls on the detector. And finally inequality 6.5 ensures none of the second order peak falls on the detector. Essentially inequalities 6.2–6.5 require that the detector inner angle be between where the direct beam ends and the 1st order peak begins, and that the detector outer angle be between where the first order peak ends and the second order begins. This is illustrated in Figure 6.5.

For our detector the ratio $\theta_{outer}/\theta_{inner} = 2.7$ in the small angle approximation, which we are always in. For graphite, θ_1 and θ_2 are given by:

$$\theta_1 = \frac{2}{3}\frac{\lambda}{\delta}, \tag{6.6}$$

$$\theta_2 = \frac{2\sqrt{3}}{3}\frac{\lambda}{\delta}. \tag{6.7}$$

where δ is the carbon-carbon in-plane bond length and λ is the electron wavelength. The bond length $\delta = 142$ pm and a 300 keV electron has a wavelength $\lambda = 2.0$ pm. This gives $\theta_1 = 9.2$ mrad and $\theta_2 = 16.0$ mrad.

Using the above, inequalities 6.2–6.5 can be rewritten:

$$\theta_{inner} > \alpha, \tag{6.8}$$

$$\theta_{inner} < 9.2 - \alpha, \tag{6.9}$$
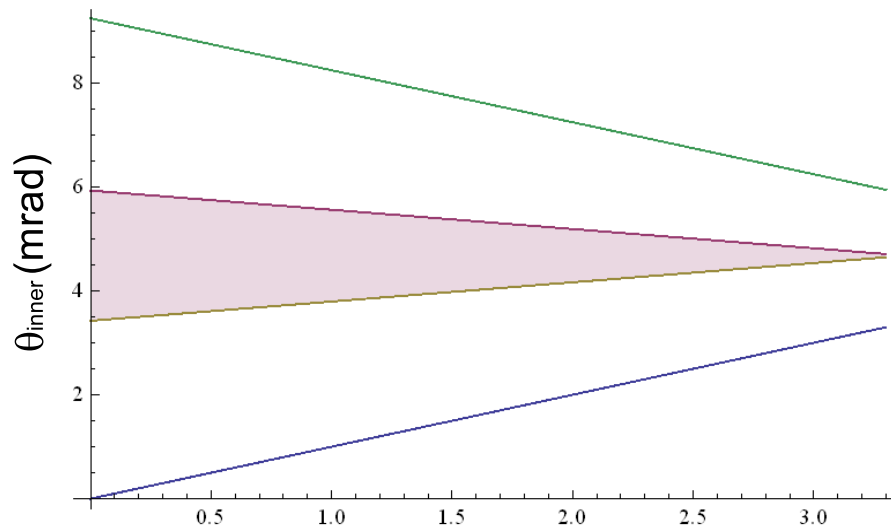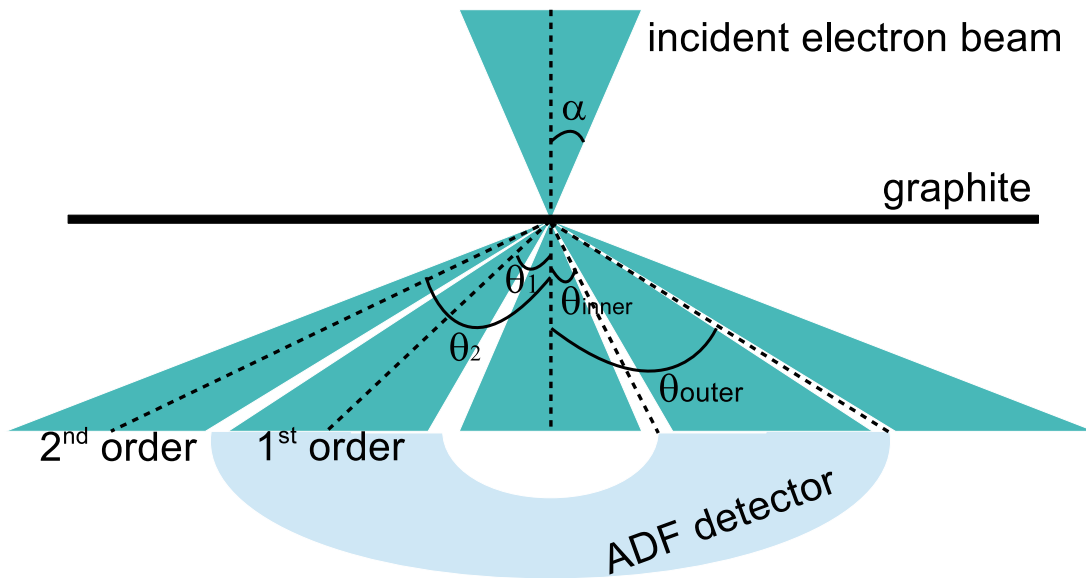
Figure 6.5: (top) Schematic of the conditions imposed by inequalities 6.2–6.5. The ADF detector angles and the convergence angles are chosen such that only the first order peaks are incident on the detector. (bottom) Plot of inequalities 6.8-6.11. The shaded region represents the area where all four inequalities are satisfied. Inequality 6.8 is the blue line, inequality 6.9 is the green line, inequality 6.10 is the yellow line, and inequality 6.11 is the red line.

$$\theta_{inner} > 3.4 + \frac{\alpha}{2.7}, \tag{6.10}$$

$$\theta_{inner} < 5.9 - \frac{\alpha}{2.7}. \tag{6.11}$$

where each numeric value is in mrad.

The result of these inequalities is shown in Figure 6.5. Plotted in this way we can see the phase space for θ_{inner} and α, the two tunable microscope parameters that we can control, that are allowed given our imposed conditions. θ_{inner} is inversely proportional to the camera length, and the convergence angle is controlled by the ratio of the objective and mini-condenser lenses, as well as the choice of C2 aperture. For the data shown below we use a convergence angle of 2.9 mrad and a detector inner angle of 3.1 mrad. Convergence angles approaching zero are inconsistent with having a focused probe. The choice of 2.9 mrad is the smallest available on our microscope operating under normal conditions.

By using STEM our time resolution for visualizing changes is determined by the pixel dwell time, and not the frame time as it would be in TEM mode. This allows correlation of peaks in the electrical transport data to events of rapid change, whereas in TEM mode changes over the course of a frame are blurred and no direct correlation between events can be made given the long exposures required. Also in STEM mode liquid cell samples are much more durable and remain stable even after prolonged exposure.

We also use Raman spectroscopy and optical microscopy to confirm the intercalation of the graphite flakes.
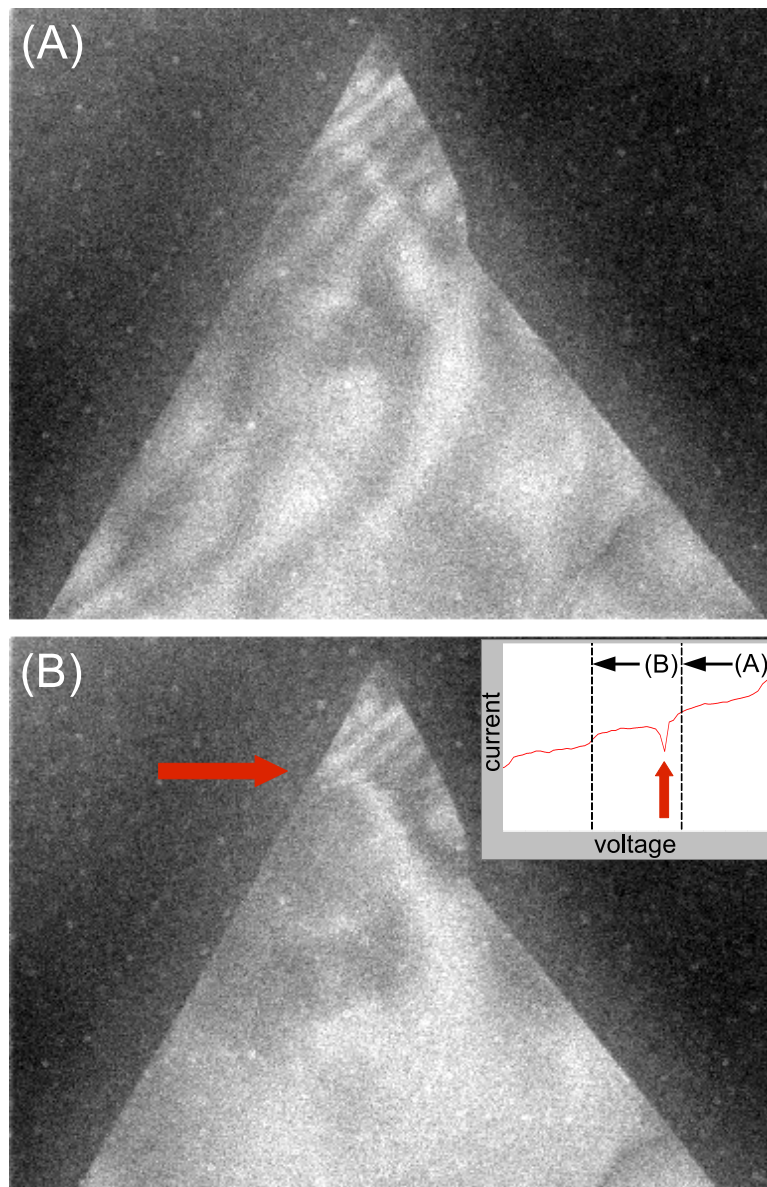
Figure 6.6: (A) ADF image of intercalated graphite. Intercalant domains present the host graphite cause the appearance of ripples. (B) ADF image of deintercalated graphite acquired immediately after (A). Approximately one tenth through the STEM beam raster for image acquisition the graphite sheet deintercalates, indicated by the red arrow. The inset shows the electrical transport data simultaneously acquired, and the peak indicated by the red arrow is synchronous with the deintercalation event in B. The field of view is 4 μm in the x direction.

6.3 Results and discussion

Figure 6.6 shows a deintercalation event. In (A), the graphite flake has already been intercalated, evidenced by the fringes in the graphite flake. The fringes are the result of the contrast mechanism illustrated in Figure 6.3 where the existence of neighboring intercalant domains in the graphite cause bend contours. The distance between bend contours, which is the distance between neighboring domains, varies from approximately 60 nm at the tip of the graphite flake to over 500 nm closer towards the bulk.

As the STEM beam begins rastering for the next frame, (B), the graphite sheet appears unchanged until the line indicated by the red arrow. At this point the graphite sheet deintercalates and it has much more uniform contrast and lacks the fringes caused by domains. The non-uniform contrast that persists is likely due to intercalant that does not exit the graphite flake indicating a high stage of intercalation.

The inset in (B) shows the electrical transport data acquired simultaneously with the ADF images. Throughout the acquisition of (A) and (B) the voltage of the graphite sheet is continuously ramping towards 0 from the positive direction, towards the starting potential of the pristine graphite. During the acquisition of (B) at the point indicated by the red arrow, there is a peak in the current data. Thus the deintercalation event evidenced by the disappearance of domains in the ADF image correlates with the deintercalation peak in the electrical transport data. The size of the current peak is -2.7 pC, which is approximately the amount of charge required to fill five intercalant layers of the entire graphite flake, meaning the peak is the right order of magnitude.

After the acquisition of (B) the potential of the graphite flake is continued to ramp down to the starting potential of the pristine flake. During this time the graphite flake remains largely unchanged in the ADF images and there are no

further deintercalation peaks in the current/voltage data.

Figure 6.7 shows the time dependence of the domain sizes as the graphite flake intercalates and deintercalates. It is also another example of the correlation between sudden changes in the ADF images of the intercalant domains and peaks in the electrical transport data. The pristine graphite (A) lacks the fringes associated with domains, but has nonuniform contrast likely due to some defect causing the lattice to bend. Upon intercalation, (B-C) the domains form. Near the end of the acquisition of (D) the flake deintercalates suddenly from a low stage to high stage. From (E) through the first half of (F) the domains move much more slowly through the graphite, until the onset of another sudden deintercalation event. In the next frame, (G), domains are no longer obvious, and many frames later (H) when the graphite has been brought back to the potential it was in its pristine form there is no sign of further deintercalation. However there is a large defect present in the graphite flake that was not apparent in the pristine image. In the lower right of (A) there appears to be the start of the defect, but by cycling the graphite the defect has grown to penetrate more of the flake (H).

The size of the current peaks in Figure 6.7 is substantially bigger than in Figure 6.6. This is because the graphite flake is 50% thicker and also almost twice the area. The thickness of the graphite flakes is measured by performing high resolution TEM imaging before the constuction of the fluid cell. The graphite flakes tend to have small folds near the edges, and the individual layers can be imaged, and counted, at these folds, similar to the way walls on multiwall carbon nanotubes are counted. This technique is illustrated in Figure 6.8.

Figure 6.9 shows another graphite flake before intercalation, and then after a given number of intercalation/deintercalation cycling. There are two distinct regions of interest on the graphite flake. The first is the bottom portion of the
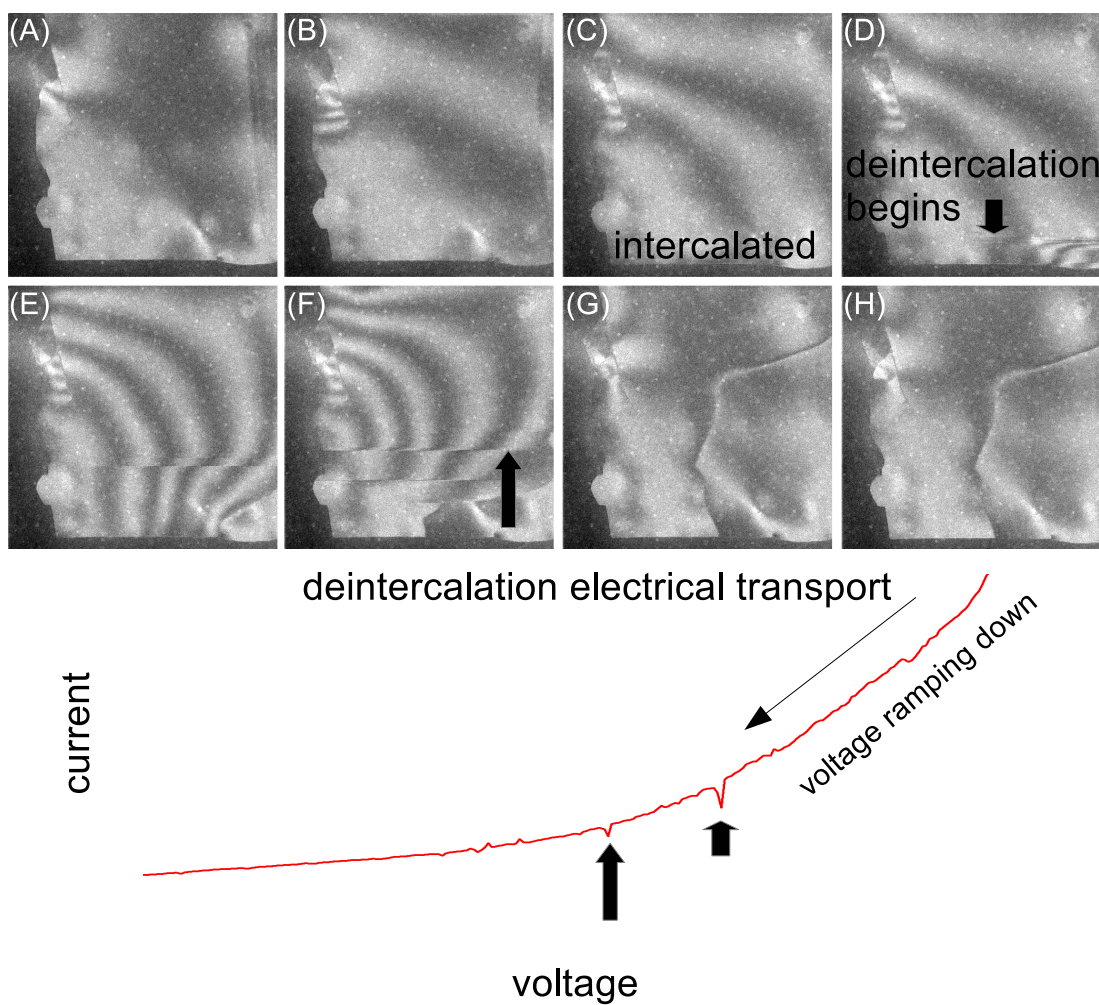
Figure 6.7: (A-H) Select frames from a time series of ADF STEM images showing the intercalation and deintercalation of a graphite flake. (bottom) Electrical transport data corresponding to the deintercalation of the flake. The sudden changes in the ADF images indicated by the black arrows are synchronous with the peaks in the current data, indicated by blacks arrows of the same respective shape. The field of view in each image is 3.7 μm, the full voltage range is 350-830 mV, and the large current peak indicated by the arrow is 15 pC and the smaller is 6 pC.
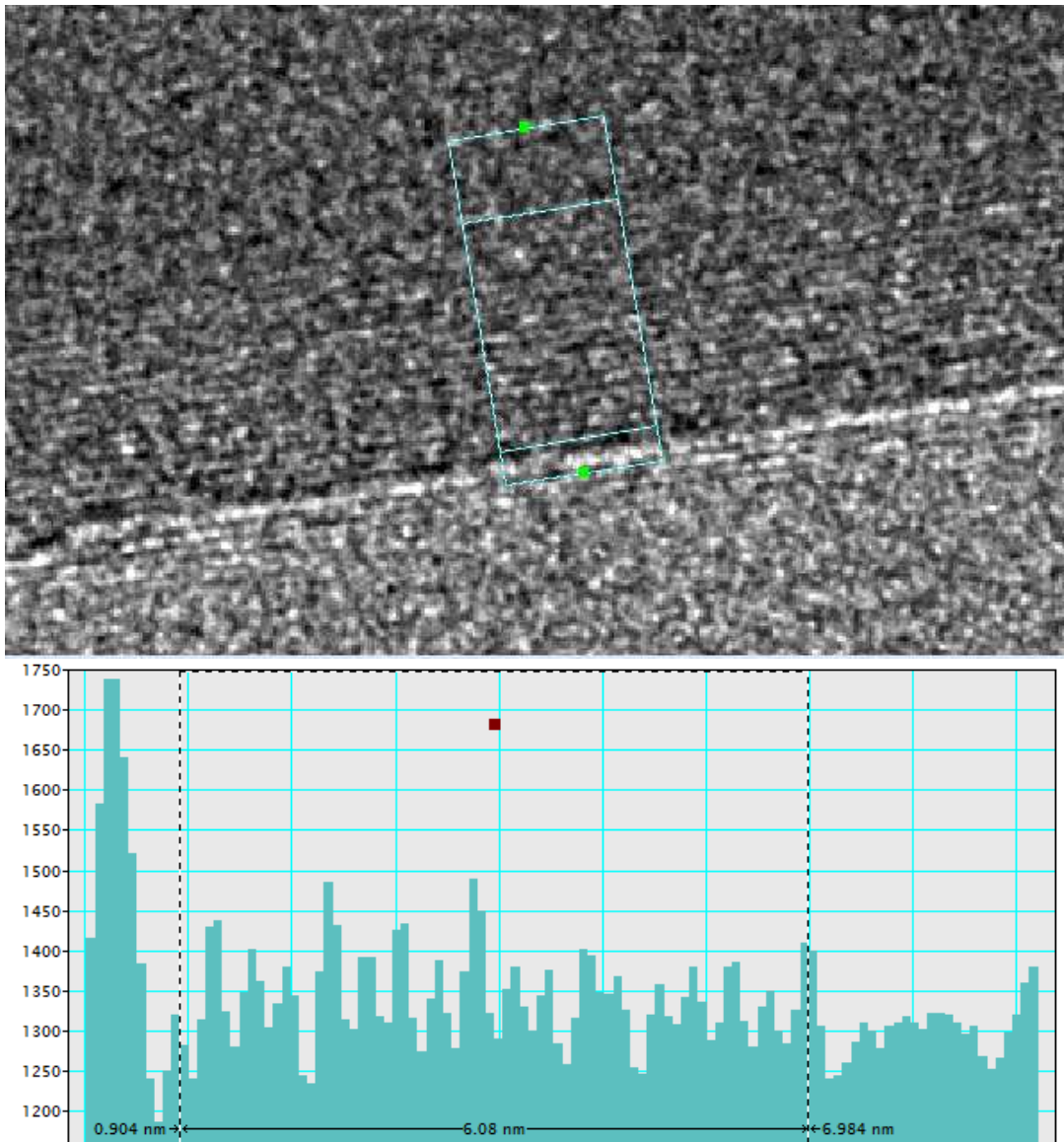
Figure 6.8: High resolution TEM image of a graphite flake with a fold. By counting the layers at the fold the thickness of the flake is determined. This flake is 6 nm thick, which corresponds to approximately 18 layers.
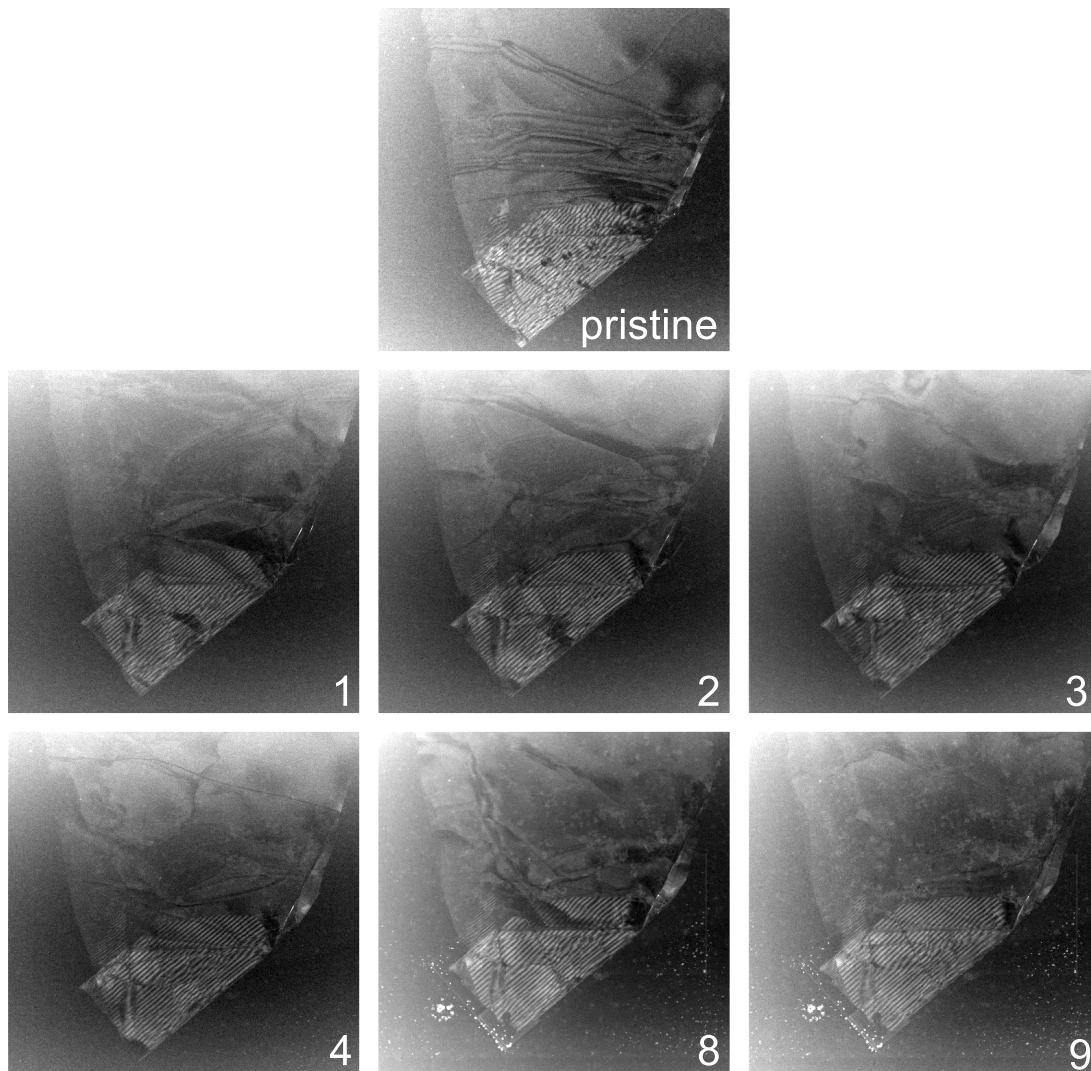
Figure 6.9: ADF STEM images of a graphite flake in the pristine case, and after n intercalation/deintercalation cycles, where n is indicated in the lower right of each image.

graphite where it has folded over onto itself. There is mismatch in the overlaying lattices caused by the fold. This mismatch gives rise to a moire pattern which is the bright stripes present in the image. The second region of interest is the rest of the graphite flake, where there is an absence of a moire pattern.

In both the folded and non-folded regions defects in the graphite lattice cause the dark lines present in the sheet. Some of the defects remain more or less intact comparing the pristine case to the post-cycling images. These defects are likely inherent to the graphite flake. One example in the line that starts at the upper left of the flake and extends to the right side at a slight downward slope.

However many of the dark lines evolve over the course of the intercalation cycling, meaning the defects move as a result of the intercalant moving in and out of the graphite lattice. Furthermore, many of the defects present in the pristine image are absent after cycling. We believe that during the transfer process the sheet becomes slightly wrinkled, and these wrinkles are smoothed out, or moved, during intercalation cycling.

The starkest example of smoothing can be seen in the moire pattern. Figure 6.10 shows the moire pattern in the pristine case and also immediately after the first intercalation event (in contrast to Figure 6.9 which shows after a full intercalation/deintercalation cycle). In the pristine case the stripes in the moire pattern are not straight, but upon intercalation the lines straighten, indicating the two lattices are overlapped in a more uniform way.

The intercalation event shown in Figure 6.10 is the first change that appeared in the graphite flake during the first time the flake was intercalated. Thus the lattice straightening that occurs begins at high stage intercalation before the detectable formation of domains appears in the graphite flake. It is also possible a layer of intercalant made its way between the 'bottom' and 'top' pieces of the folded graphite and allowed the lattices to more uniformly over lap. If the latter is true, it represents a new kind of intercalation between graphite sheets that are

at an angle relative to one another, rather than the usual AB stacking, which happens at a lower voltage than intercalation into the AB stacked flake. The intercalation event appears to be irreversible, as the moire pattern remains straight even after repeated cycling.

We verify our ability to electrochemically intercalate graphite with optical and Raman spectroscopy experiments on bulk samples as well as samples similar to those we image in the TEM.

Figure 6.11 shows results from intercalating an approximately 0.5 mm thick graphite flake 6 mm by 4 mm on each side. A platinum wire is used as the reference electrode, and a platinum foil as the counter electrode. A cyclic voltammogram is performed at a rate of 0.1 mV/s from -0.26 mV to 1.6 mV. As the voltage ramps up the graphite flake undergoes structural changes as it begins to intercalate. Then the flake turns blue when it reaches stage 1. The CV has similar characteristics compared with the literature[71]. We see high stage intercalation peaks consistent with the onset of intercalation, followed by a stage 1 0.55 V later, and finally the oxidation peak 0.63 V after that. As the voltage ramps down the graphite flake deintercalates and this process can be cycled many times and is highly reversible.

We repeat this experiment with a small flake approximately 80 layers thick that is 100 um by 40 um on each side. The flake is transfered onto a silicon chip with prepatterened platinum electrodes, the same configuration as the fluid cell we image in the TEM, but without the 'top' of the sandwich. We observe changes in the color of the graphite as it intercalates as shown in Figure 6.12. Unlike the bulk experiment we see dramatic color changes of the flake from high stage throughout the staging process. There is a voltage offset compared with the bulk experiments that can likely due to the fact that platinum is a pseudoreference material so the absolute potential we measure is rather meaningless, and there
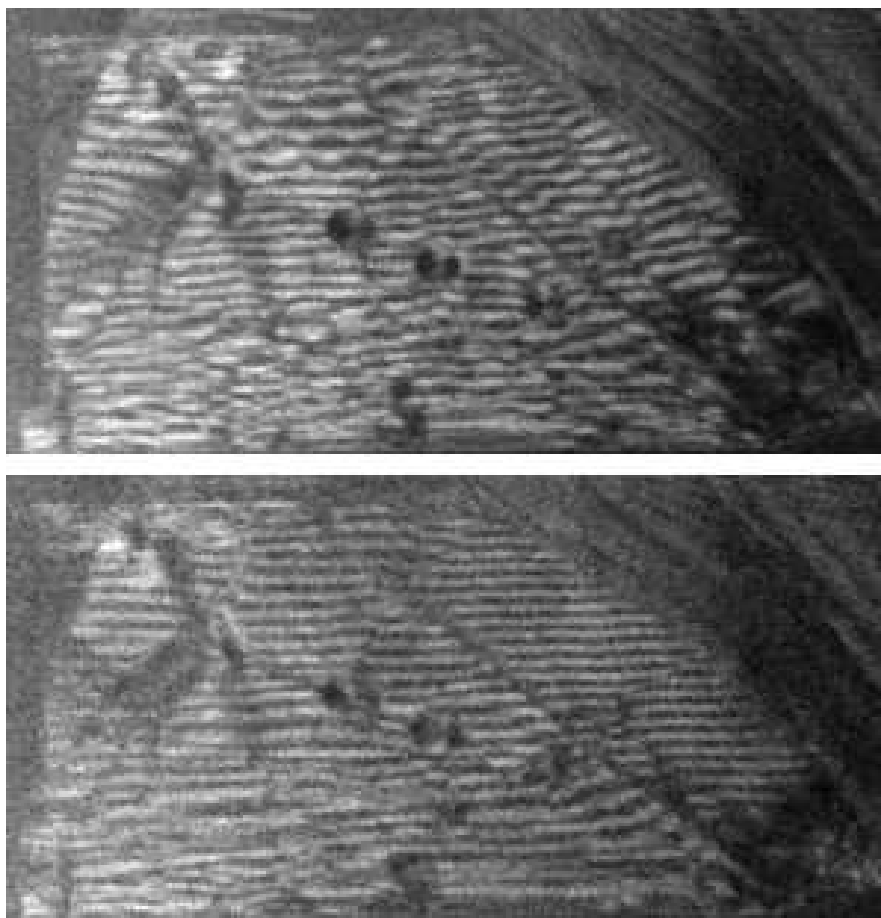
Figure 6.10: (top) Non-intercalated graphite. The single graphite flake folded over onto itself giving rise to a moire pattern. Ripples in the graphite cause the waviness in the fringes. (bottom) Intercalated graphite. Upon intercalation the fringes in the moire pattern straighten indicating the wrinkles in the graphite lattice have been removed.
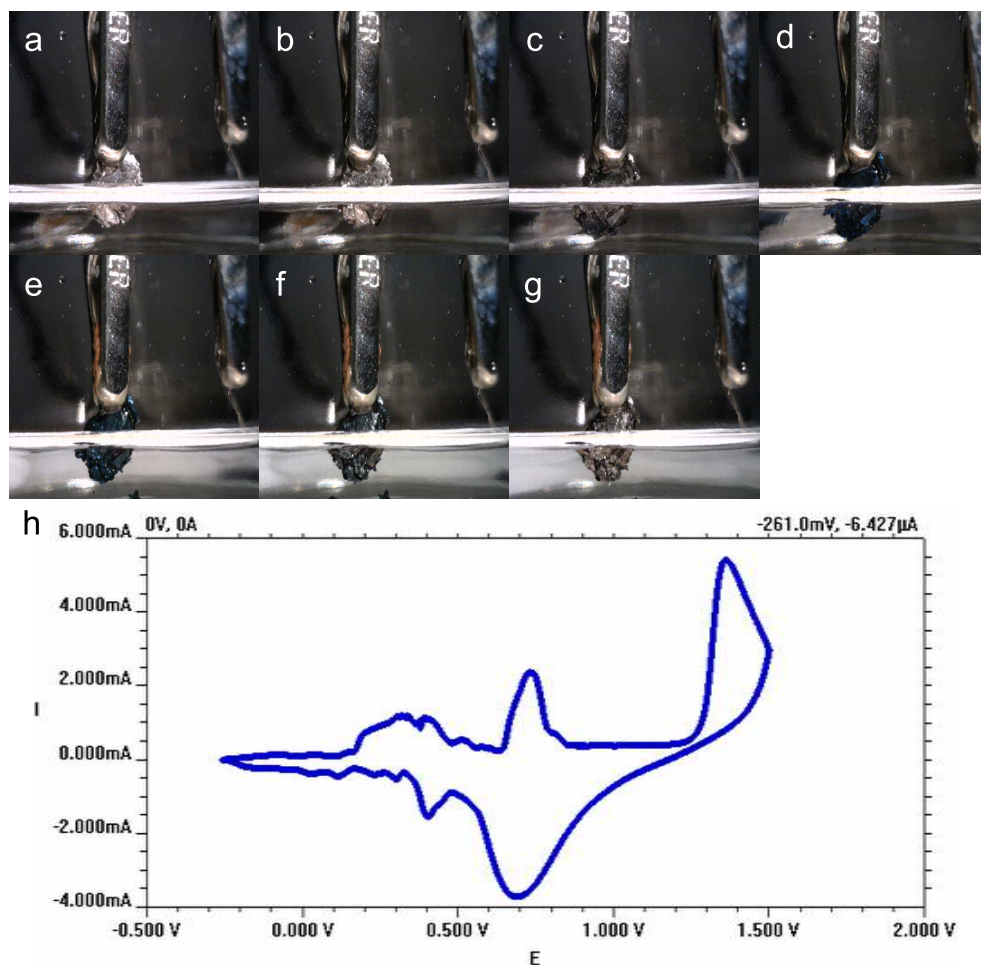
Figure 6.11: Intercalation process of natural graphite in 18 M sulfuric acid, H_2SO_4, via cyclic voltammetry. The graphite, 17.77 mg, was partially submerged in the liquid and electrically connected through a stainless steel alligator clip. (a) graphite at open circuit potential. (b) first signs of structural changes. (c) GIC at stage 2. (d) blue color change indicating the GIC is at stage 1. (e,f) deintercalation of the graphite from stage 1 to stage 2 respectfully. (g) fully deintercalated graphite. (h) cyclic voltammetry plot showing stage peaks. The scan rate was 0.1 mV/s. (a-g) were taken at -261.0, 207.9, 652.6, 868.6, 498.3, 322.2, and -261.0 mV respectively. The counter and pseudo-reference electrode are a platinum sheet and wire respectively, and are both viable in (a-g).
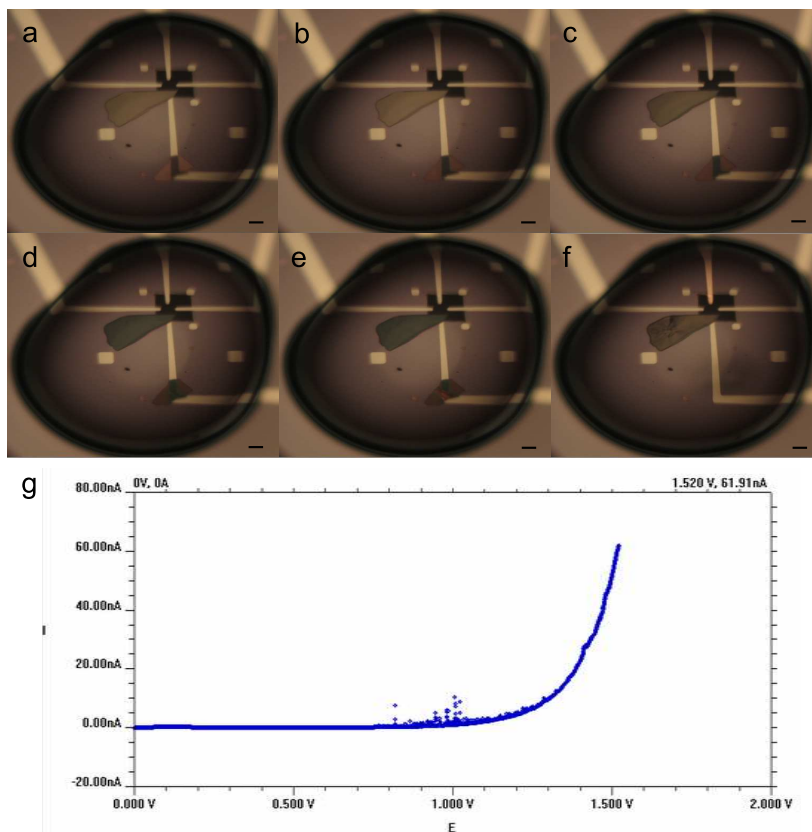
Figure 6.12: Intercalation process of exfoliated single crystal graphite in 18M sulfuric acid, H_2SO_4, via cyclic voltammetry. The two pieces of graphite were covered by a drop of the liquid and electrically connected through a platinum electrode. (a) graphite at open circuit potential. (b) first optical color change in thinner graphite (smaller). (c) first optical color change in thicker graphite (bigger). (d) blue color change in thicker graphite. (e) initial signs indicating delamination of thinner graphite. (f) both pieces have delaminated from the electrode. Thicker graphite has partially deintercalated. (g) cyclic voltammetry plot showing intercalation peaks. The scan rate was 1 mV/s. There are no deintercalation peaks shown because the graphite was no longer electrically connected. (a-f) were taken at 0.238, 818.9, 986.7, 1289, 1363, and 1604 mV respectively. The counter and pseudo-reference electrode were platinum electrodes shown in (a-f). The scale bar is 10 μm.

is a 5 nm sticking layer of titanium which could cause potential mixing. In the small scale experiments a large double layer charging background dominates the electrical transport above roughly 1.2 V. The peaks are also very narrow; the flake is several million times smaller than the bulk flake and can intercalate very quickly. Each peak may the formation or sliding of a domain in the graphite, or intercalation event. Many more peaks are visible than there are intercalation stage transitions, thus in contrast to the bulk measurements where a broad peak is related to the intercalation stage, with small enough flake individual intercalant domain movements may be resolved in the transport data.

We verify the staging of the graphite by performing Raman spectroscopy. Pristine graphite has a well defined G peak at 1582 cm^{-1}, and the G peak shifts as the graphite intercalates to 1610-1615 cm^{-1} at high stage, 1620 cm^{-1} at stage 2, and 1635 cm^{-1} at stage 1[72]. Figure 6.13 shows Raman spectra on pristine and intercalated graphite, both bulk samples and small flakes. The bulk sample we intercalate via cyclic voltammetry at a scan rate of 5 mV/s to 1.1 V, where it was held for approximately 10 minutes. After which the graphite was a deep blue, and we verified stage 1 with Raman spectroscopy as shown in Figure 6.13. The spectrum with the G2 peak and GN shoulder is after the flake was exposed to air for sufficiently long for it to partially deintercalate.

With the small graphite flake we can perform the Raman measurements *in situ* , and we intercalate the small flakes up to stage 2 as shown in Figure 6.13. Here cyclic voltammetry with a scan rate of 0.4 mV/s was used to intercalate the graphite flake. The Raman spectra are taken with the minimum possible power to see any resolvable peak to limit damage from the laser. We are unable to intercalate the small graphite flakes to stage 1, as bubble formation on the working electrode causes the flake to delaminate from the platinum and we lose electrical connection to the flake.
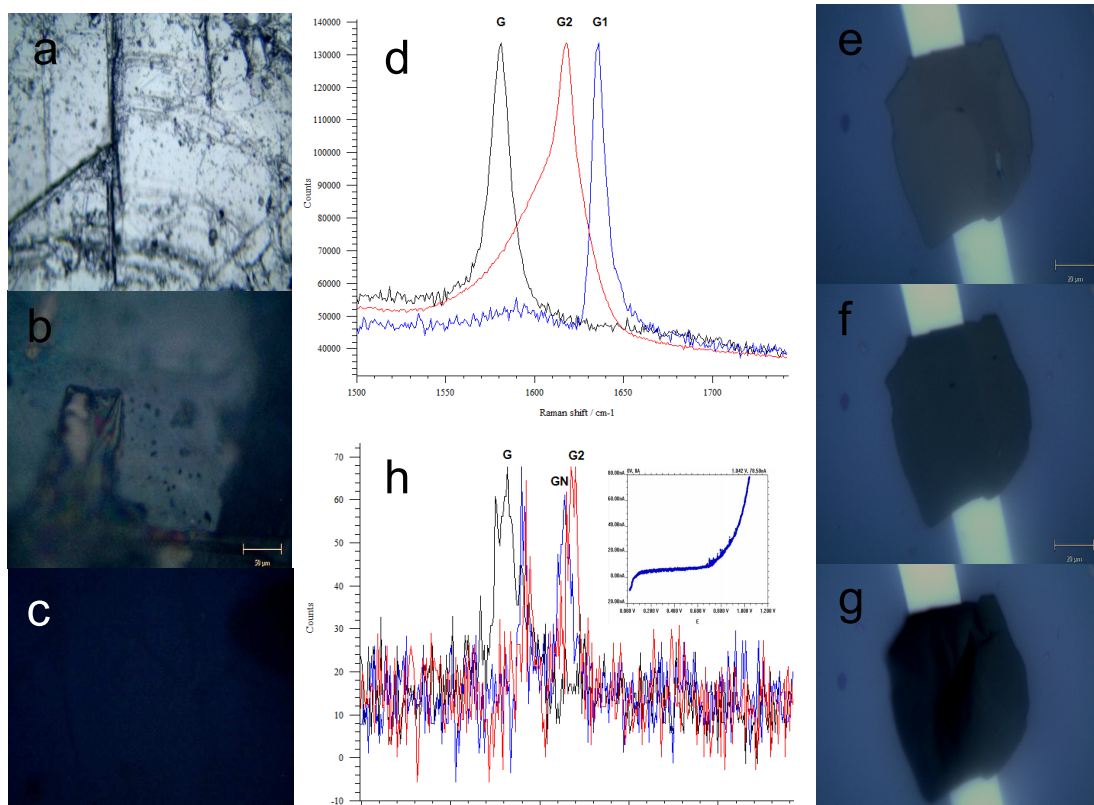
Figure 6.13: Raman spectroscopy of graphite intercalation. (a) Optical image of pristine graphite. (b) GIC at stage 2. (c) GIC at stage 1. (d) Raman spectra of (a-c) showing the G, G2, and G1 peaks respectively. (e-g) *In situ* Raman on an exfoliated single crystal graphite on a platinum electrode submerged in a drop of 18 M sulfuric acid. (e) Pristine graphite. (f) GIC at stage n (n ¿ 2). (g) GIC at stage 2, showing signs of delamination through bubble formation. (h) Raman spectra of (e-g) showing the G, GN, and G2 peaks respectively. The inset shows the cyclic voltammetry. (e-g) were taken at 22.08, 817.5, and 1008 mV respectively.

Using the laser to acquire the Raman spectra on intercalated graphite can severely damage it. The laser tends to put holes in the graphite, even when using the smallest possible laser power to see the peak in the spectra, accompanied by the formation of a large D peak, indicating defective graphite. This limits the number of spectra that can be taken per sample once it intercalates. The problem persists when using both 514 nm and 732 nm wavelength lasers. No such damage was observed on non- or de-intercalated graphite

6.4 Conclusion

In summary, we have imaged evidence of domain formation and movement during intercalation cycling of graphite. We accomplish this using the fluid cell TEM technology sandwiching a small graphite flake submersed in H_2SO_4 between two electron transparent Si_3N_4 windows. We choose imaging conditions in which bending of the graphite lattice gives contrast in STEM, allowing us to visualize the formation of domains upon intercalation. By using STEM we can can correlate changes in the STEM image to current peaks in the transport data with millisecond precision, which is much faster than the total frame acquisition time. We verify the intercalation stage with optical imaging and Raman spectroscopy.

CHAPTER 7

Electron beam induced current (EBIC)

The electron beam induced current (EBIC) method is a well established technique for characterizing semiconductor materials and devices[76]. When an energetic electron is incident on a semiconducting material it creates a large number of electron-hole pairs by inelastically scattering valence electrons into the conduction band, approximately equal to the incident electron's energy divided by the band gap in the semiconducting material. These electron-hole pairs can then be separated by an electric field, and this (electron beam induced) current is measured. EBIC is traditionally done in a scanning electron microscope, where, as in STEM, the electron beam rasters across the sample. At each pixel the EBIC signal is measured and an EBIC image can be generated where the intensity of each pixel is proportional to the EBIC signal.

The electric field that separates the electron-hole pairs can be generated externally or it can exist internal to the material. Often times the interesting material properties result in the latter, one example is the a p-n junction. When a p-doped (i.e. excess free hole concentration) and an n-doped(i.e. excess free electron concentration) region of a semiconducting material meet the result is a p-n junction. At the junction, holes from the p side diffuse into the n side, and electrons from the n side diffuse into the p side, until steady state is reached and the electric field this charge separation sets up exactly cancels the diffusive force. This electric field is what separates the charge carriers created by an incident high energy electron. This measurement technique is illustrates in Figure 7.1.
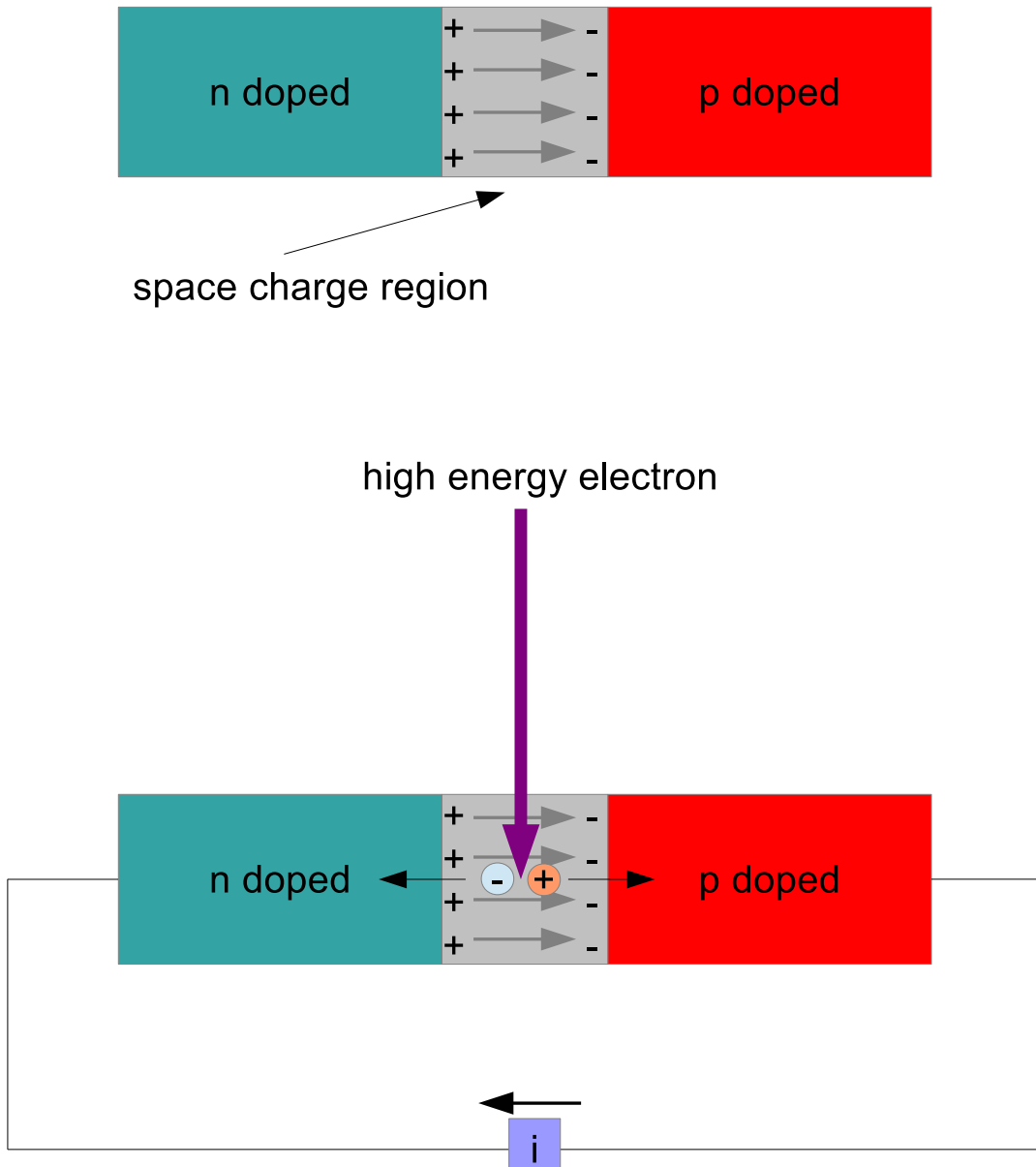
Figure 7.1: (top) Illustration of the space charge region and creation a the built in electric field as a result of a p-n junction. (bottom) EBIC signal from a p-n junction. The high energy incident electron creates electron hole pairs that are separated by the internal electric field. This creates a current that is measured, which is the EBIC signal.

EBIC is a common method used to locate p-n junctions. The EBIC method can also be used to determine carrier lifetime, diffusion length, defect energy levels, and surface recombination velocities, as well as reveal recombination sites such as dislocations and precipitates, and the presence of doping level inhomogeneities[76].

7.1 Experimental setup

Figure 7.2 shows the schematic layout of the EBIC setup illustrating the parallel acquisition of the EBIC and STEM data. The EBIC current from the sample is converted to a voltage using a transimpedance amplifier. This voltage is fed into the extra port on the microscope digitizing hardware. Thus both the STEM signal and the EBIC signal are digitized simultaneously in parallel and displayed by the microscope software.

The transimpedance amplifier we use is a FEMTO DLPCA-200, which is a variable gain low noise current amplifier. The maximum gain is 10^{11} V/A, thus a 1 pA signal will generate a 100 mV signal. We routinely achieve sub-picoamp resolution, limited by the noise discussed in the next section. Again this is several orders of magnitude better than the size of currents typically measured in an SEM EBIC system, and is to our knowledge the most sensitive EBIC system developed to date.

7.2 Noise

Often times minimizing noise is a significant challenge to perform precision measurements. There are two main sources of noise we've encountered with EBIC. The first is a systematic effect resulting from using electronics that necessitate wall power, and resulting in 60 Hz noise. The second is a fundamental limitation based on the device impedance that manifests as Johnson noise.

7.2.1 60 Hz noise: the art of proper grounding

By virtue of using electronics that need to be plugged into the wall there is the potential for 60 Hz noise to creep into the measurement. Typically this noise can be eliminated by ensuring all ground loops have been eliminated. In this case there is an additional problem that we have three competing grounds: the microscope column, the sample holder, and earth ground (from the wall) are all at different and time dependent potentials. The solution is to ensure on the measurement side the holder potential is used as ground, since it houses the wires that connect to the device. Then the FEMTO output is put through an isolation amplifier, which separates the measurement ground from the digitizing electronics that need to use earth ground from the wall. While tempting, the microscope column is not used as ground. With these precautions in place the 60 Hz noise signal is less than 1 pA, which is well below the signal size for most measurements. For measurements on the order of the noise level, the noise can be removed after the fact by postprocessing. Since the beam rasters at a constant rate and the 60 Hz noise component does not drift it can be removed essentially with a notch filter after acquiring the image. Of course the measurement can only be done if the noise does not use up the full dynamic range which is why it's still critical to minimize the noise as much as possible before the measurement is done.

7.2.2 Johnson noise

The second type of noise is a fundamental physical limitation on the size of the signal we can measure. Johnson noise is the result of the thermal fluctuations of the charge carriers in a resistive element. It can be shown that the Johnson noise current generated by a resistor R at temperature T is given by[77, 78]:

$$i_n = \sqrt{\frac{4k_B T \Delta f}{R}},$$ (7.1)

where k_B is Boltzmann's constant, and Δf is the bandwidth in Hz. This formula is classic example of the fluctuation-dissipation theorem, generalized by Callen and Welton[79]. For our EBIC measurements the bandwidth is set by the current amplifier which has a maximum bandwidth of 1 kHz at maximum gain. This corresponds to a 1 ms dwell time for the scanning speed. To reduce read noise we want the current amplifier integration time to be longer than $1/\Delta f$, thus our dwell time is usually at least twice $1/\Delta f$, or 2 ms. The acquisition of a 256x256 square pixel image then takes just over two minutes. In principle the noise can be reduced by increasing the dwell time, however since you only reduce the noise as the square root of the bandwidth the acquisition times become impractically long for an appreciable reduction in Johnson noise.

As an exercise we calculate the Johnson noise due to a 100 kΩ resistor at room temperature with a bandwidth of 1 kHz. Plugging in the numbers we find $i_n = 13$ pA. Even for a moderate resistance of 100 kΩ the Johnson noise is already 100 times larger than the smallest signal we'd like to measure. Unlike the 60 Hz noise there is no way to remove the Johnson noise with postprocessing. In order to see EBIC signals on the order of a picoamp or less device impedances of at least 1 GΩ are required.

This also requires special precautions for wiring the connections to the device. If there is a leakage current path that has an impedance less than the device impedance the leakage Johnson noise will dominate. All connections should be on the order of 1 TΩ, which is nontrivial. Many out of the box parts have impedances less than 1 TΩ. Care must be taken only to use parts rated at leakages less than this level, and the parts must be kept extremely clean while building the wire housings.
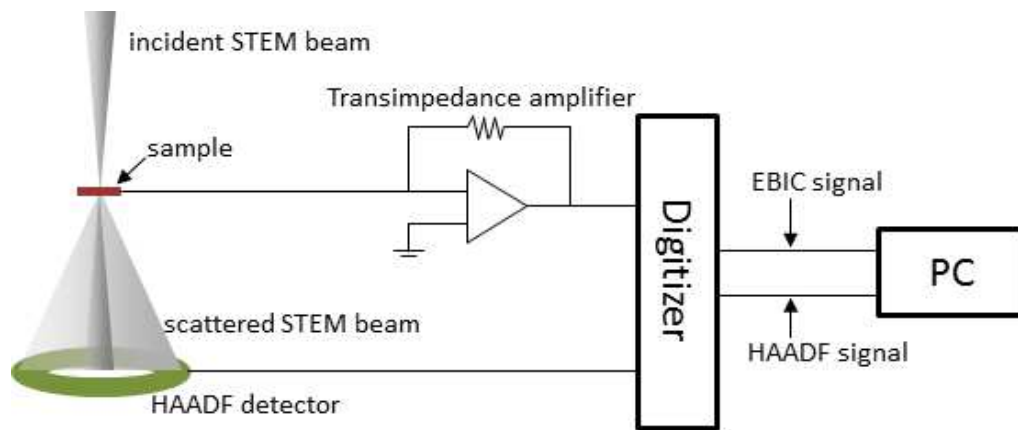
Figure 7.2: Schematic of simultaneous EBIC and HAADF data acquisition. Current generated in the sample is converted to a voltage appropriate for the microscope digitizing electronics by the transimpedance amplifier. The HAADF signal is digitized in parallel with the EBIC signal, thus the two images are generated simultaneously.

CHAPTER 8

EBIC on atomically thin films

8.1 Vertical heterostructure photo cell

The construction of heterostructures made from thin layered materials such as graphene and transition metal dichalcogenides (TMDCs) has created a new area of materials research, as these ultrathin hybrid structures have interesting properties making them suitable for electronic and photonic devices. One such heterostructure that has seen much recent interest is a graphene-MoS_2-graphene heterostructure, which has been shown to have strong light-matter interactions via photocurrent generation[80, 81]. However, the stability of a device of this kind in less benign environment is an open question. Here we show how the device responds to ionization damage using the electron beam induced current (EBIC) method.

The heterostructures are fabricated using the same transfer technique described in the graphite intercalation chapter. Here three transfers are required. First graphene is transfered onto MoS_2, then that combination is transfered onto another graphene sheet, and finally the completed heterostructure is transfered onto an electron transparent membrane with predefined platinum electrodes, onto which each graphene sheet makes electrical contact with.

In these devices band bending at the graphene-MoS$-$2 interface creates the electric field inside the device that captures the charge carriers generated by the
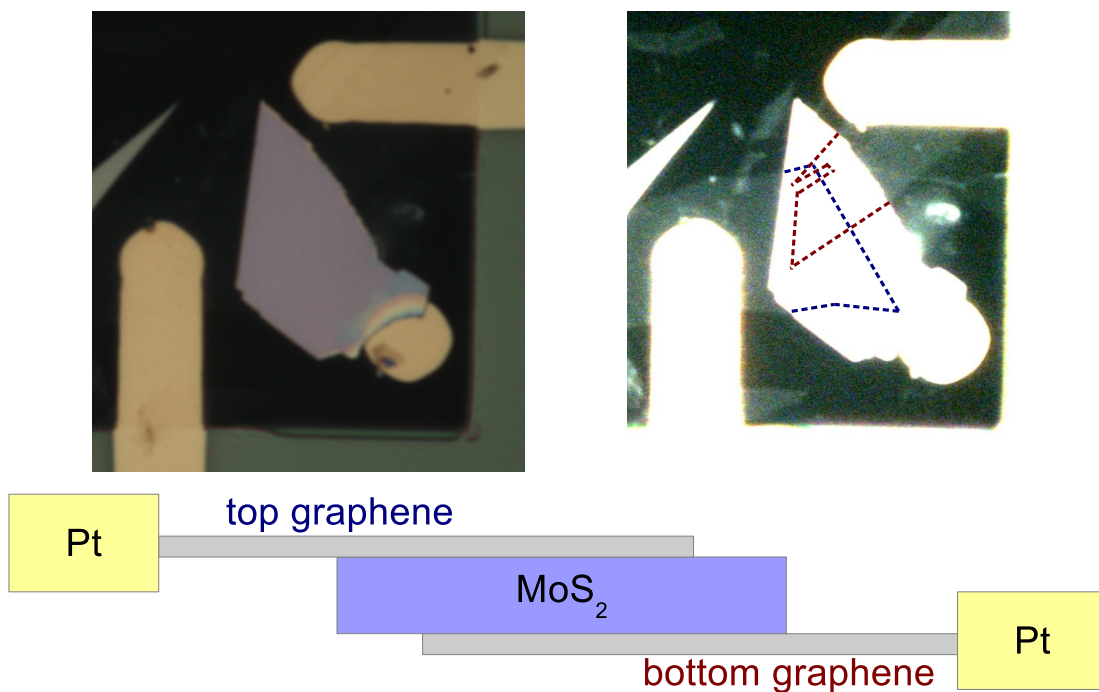
Figure 8.1: Graphene-MoS$_2$-graphene heterostructure. (left) Photograph of heterostructure. The large purple flake is the MoS$_2$, and sits over an electron transparent window of Si$_3$N$_4$. (right) The sample photograph with the brightness and contrast altered to highlight the graphene over the window. The outline of the graphene-MoS$_2$ overlap regions are continued by the dotted lines. (bottom) Cross-sectional schematic of the heterostructure.

electron beam. The electron beam acts to both create the electron hole pairs, and to gradually cause the ionization damage. By continually imaging the device ionization damage increases, which causes local changes in the EBIC response, as shown in Figure 8.2. Initially the entire MoS$_2$ sheet has an EBIC signal, in fact the edges where there is no overlap with the graphene shows the strongest response. This indicates that the diffusion length is on the order of the size of the MoS$_2$ crystal, or 10 μm. After several minutes of exposure to an approximately 100 nA electron beam the only part of the MoS$_2$ that shows an EBIC response is the part in direct contact with the graphene layers. The top layer shows a much stronger EBIC response at this point. This means that the diffusion length has decreased to less than 150 nm, which is the smallest feature size we resolve. Ionization damage caused the diffusion length to decrease by two orders of magnitude and totally change the EBIC response of the device, this has implications for future use of a device of this type in any environment in which it can be subject to this type of damage.

As these heterostructures show promise for applications as photonic devices we also perform photocurrent measurements. The measurement configuration for photocurrent measurements is identical to that of EBIC except that a Keithley 2400 is used to measure the current. Also the charge carriers are generated by a 514 nm laser that is focused onto and then scanned over the sample. Unlike in the TEM where only a small fraction of the incident probe produces electron-hole pairs, almost all of the light is absorbed by MoS$_2$. We used a laser power of 3 μW in all measurements. The photo generated current is given by

$$i = \eta \frac{e\lambda}{hc} P = \eta \frac{\lambda}{1240 \text{ nm}} P \tag{8.1}$$

where η is the external quantum efficiency, λ is the wavelength of light, P is the laser power, and h, c, and e are Planck's constant, the speed of light and the fundamental charge, respectively. Our devices have efficiencies of roughly

10%. Using the laser parameters above the photogenerated currents should be on the order of tens to hundreds of nanoamps, which is why the low noise current amplifier is not required.

Figure 8.3 shows a the photocurrent measurements before and after high dose imaging in the electron microscope along with the corresponding EBIC images. The similarities in the features present in each pair is clear. In the 'before' pair the region of the MoS_2 covered by the top layer of graphene is obvious, and draws current in the opposite direction as the rest of the sheet. In the 'after' pair the bottom layer of graphene is the most prominent. However once the diffusion length drops below the last spot size, which is approximately 1 μm, structure only resolvable in the EBIC image is revealed. The island-like structure is a result of inhomogeneities in the graphene sheet as a result of the transfer process. These are likely small folds in the graphene sheet that act as recombination centers, locally suppressing the induced current.

8.2   Many-layer graphene

Since its discovery in 2004 graphene has become a very widely studied material. The electronic excitations in single layer graphene can be described as two-dimensional massless Dirac particles, resulting in desirable electronic properties for nanoelectronic devices. Adding layers allows the electronic properties to be tuned, thus multilayer graphene is better suited for some device applications. Characterizing defects in this material is critical for understanding device performance. Recently Butz et al. have used dark field TEM to image dislocations in bilayer graphene, furthering our understanding of its electronic properties and the key importance of defects [82]. Here, we report using electron beam induced current (EBIC) measurements in a scanning transmission electron microscope (STEM) to image local changes in the conductivity of multilayer graphene.

Typical EBIC signal is generated when the incident electron beam impacts a semiconducting material creating electron-hole pairs that are collected by an electric field. Another, much weaker way to induce current in the sample is by secondary electron emission. Occasionally a high-energy incident electron will collide with an electron in the sample, ejecting it into the vacuum. The resulting net positive charge on the sample escapes to ground via the current amplifier, creating the EBIC signal. In this case no gain results and the currents are smaller than the incident beam current, typically picoamperes.

Figure 8.4 shows a single, multilayer graphene sheet and the corresponding ADF and EBIC images. The contrast in the EBIC image is not produced by electron-hole separation. Electron-hole pairs generated in the graphene must recombine since there is no second electrode to collect the opposite charge carrier. Thus, we attribute the EBIC signal to secondary electron emission. The incident electron beam current is 200 pA and the EBIC signal generated in the graphene is about 10 pA, which is consistent with expectations for a secondary electron EBIC signal. A comparison of the ADF and EBIC images in Figure 2 reveals the advantages of EBIC imaging. Regions of low conductivity in the graphene sheet likely caused by defects give a smaller EBIC signal. Contrast from these defects is completely absent from the ADF image. The ADF signal is dominated by residue left over from the graphene transfer process. EBIC is sensitive to the electrical properties of the sample, and thus reveals the important electrical information desired when characterizing devices for nanoelectronic applications.

Figure 8.5 shows three SEM pictures of the same sample shown in Figure 8.4. The secondary electron detector is used to generate the image. The features are similar to those in the EBIC image, as would be expected as both contrast mechanisms are via secondary electron emission. However, the EBIC shows bright contrast only in regions that are electrically connected to the current amplifier.

106

EBIC does what SEM cannot: provides a spatial map of electrical connectivity of the device.
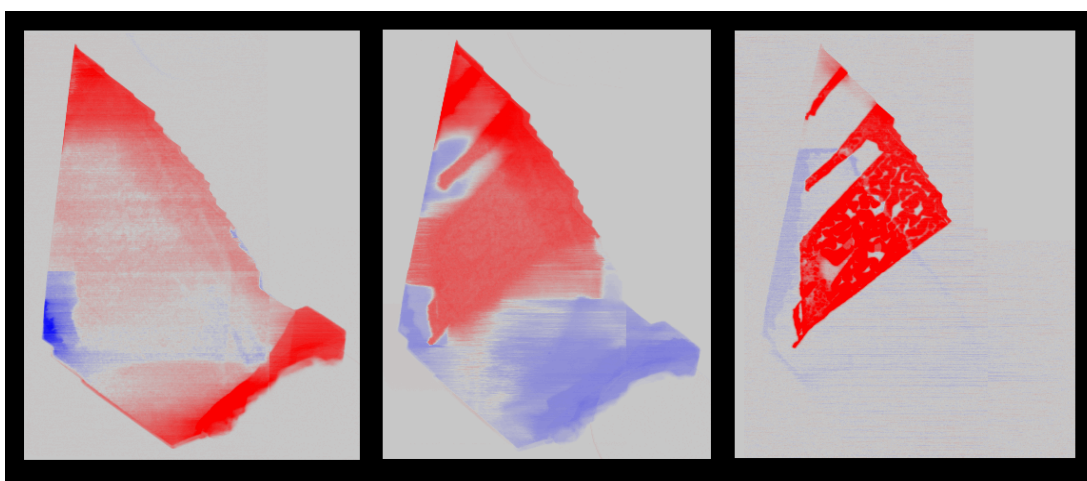
Figure 8.2: Series of EBIC images of a graphene-MoS$_2$-graphene heterostructure. The total dose the heterostructure has received increases from left to right, with the leftmost being the first EBIC image taken, and the rightmost having received a dose of approximately 1 μC.
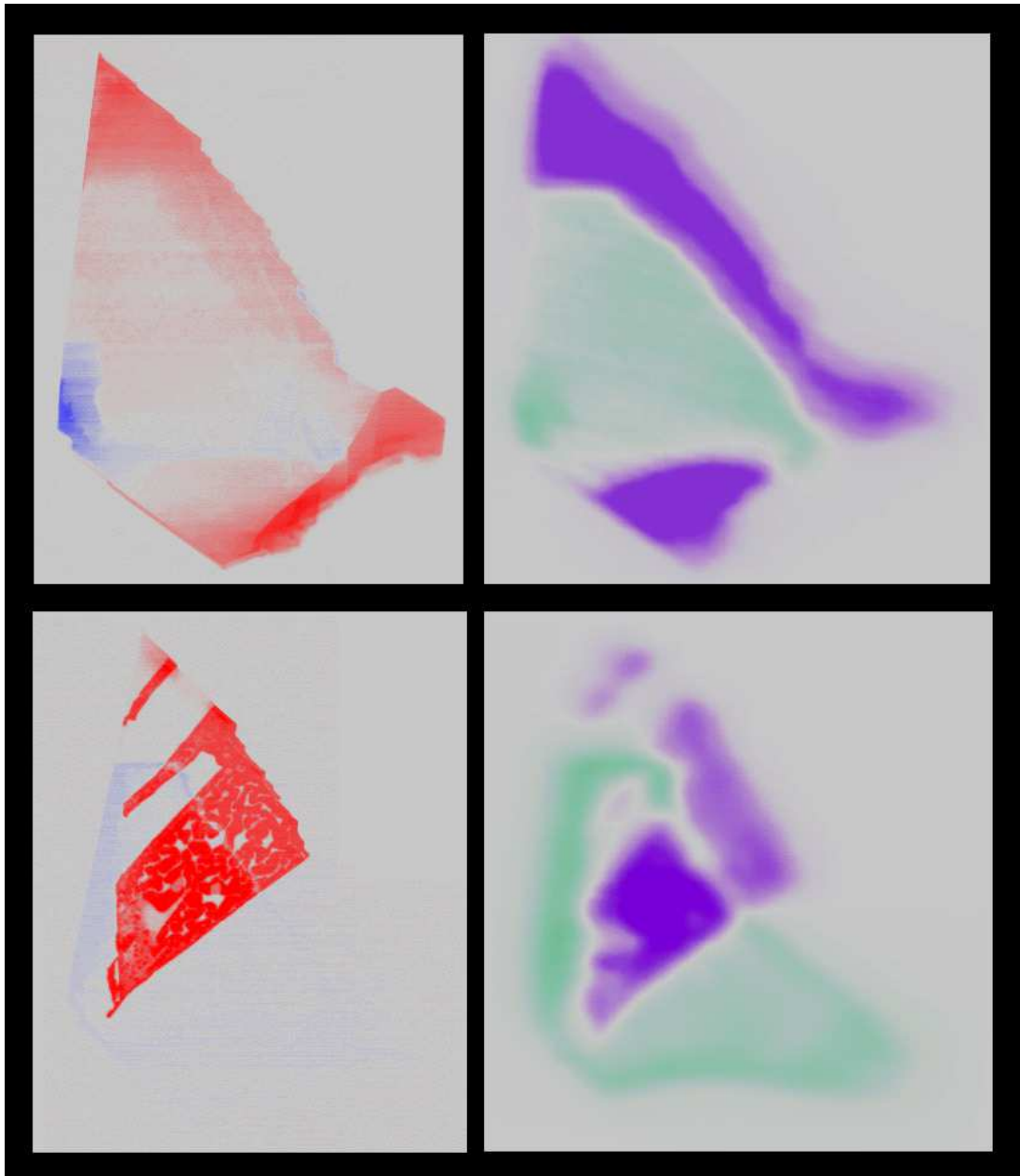
Figure 8.3: Comparison of EBIC and photocurrent measurements before (top) and after (bottom) high dose imaging. The left two images are EBIC and the right two are photocurrent.
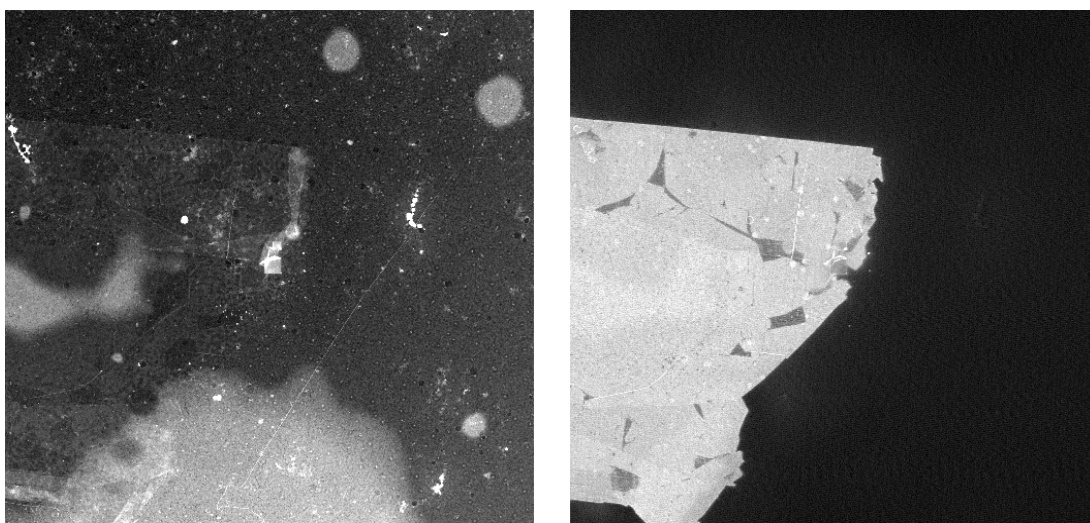
Figure 8.4: ADF (left) and EBIC (right) images of a multilayer graphene sheet. In the ADF image residue left from the graphene transfer process produces most of the contrast. EBIC signal is only generated by electrically connected regions, hence only the graphene generates contrast. Areas with reduced EBIC signal in the graphene sheet correspond to regions of reduced conductivity. The images are 7 μm on a side.
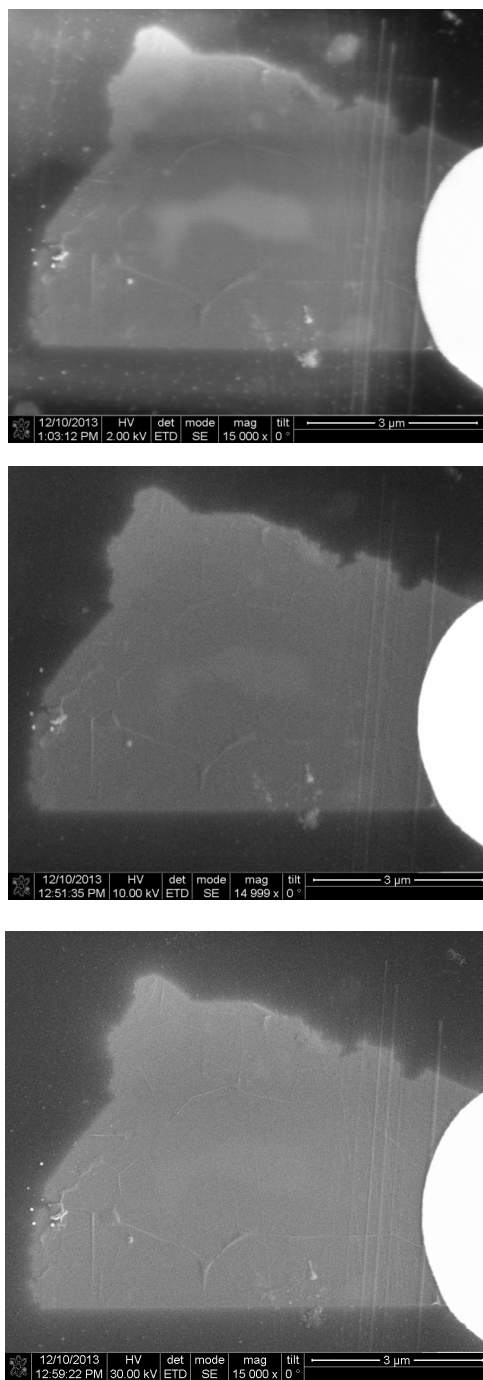
Figure 8.5: SEM images of many-layer graphene at different accelerating voltages. The secondary electron detector was used to form all of these images, and from top to bottom the accelerating voltages are 2 kV, 10 kV, and 30 kV.

CHAPTER 9

Conclusion

The transmission electron microscope is an indispensable tool for scientists across disciplines interested in performing structural characterization of nanoscale materials. Experiments can be done inside the TEM to visualize dynamical processes driven by an external probe, or the electron beam itself. Advances in nanofabrication processes have resulted in the construction of microfluidic chambers that hold thin fluid layers between two electron transparent windows. Combining this technology with electrical transport measurements we have performed pioneering research in this new field. We give an account of dose effects due to nanoparticle charging by the electron beam under conditions previously considered to be benign. We observe the formation and collapse of nanobubbles, giving some of the highest resolution images to date. We initiate the growth and dissolution of dendrites in solution, imaging a common battery failure mode at the nanoscale. We demonstrate ion diffusion can be directly imaged in the TEM. Finally we give evidence of Daumas-Herold domains in graphite intercalation and image their time evolution during intercalation cycling.

We also develop a system for performing electron beam induced current(EBIC) measurements in the transmission electron microscope. Overcoming the technical challenges associated with small electrical signal detection in a TEM, we show secondary electron emission can generate contrast. The secondary electrons must be generated from a part of the sample that is electrically connected to the current amplifier in order to produce EBIC contrast. Thus the EBIC signal gives a

topological map of electrical connectivity in the device. We also perform traditional EBIC measurements on graphene-MoS$_2$ heterostructures and visualize the time evolution of the minority carrier diffusion length under continued ionization damage. These heterostructures show promise for use in photoactive devices, and our results have direct implications for future applications.

References

[1] Reimer, L. & Kohl, H. *Transmission electron microscopy : physics of image formation* (Springer, Berlin, 2008).

[2] Gringer. Scheme tem en. *Wikipedia* (2009).

[3] Williamson, M. J., Tromp, R. M., Vereecken, P. M., Hull, R. & Ross, F. M. Dynamic microscopy of nanoscale cluster growth at the solid-liquid interface. *Nature Materials* **2**, 532–536 (2003).

[4] Dukes, M. J., Peckys, D. B. & de Jonge, N. Correlative fluorescence microscopy and scanning transmission electron microscopy of quantum-dot-labeled proteins in whole cells in liquid. *Acs Nano* **4**, 4110–4116 (2010).

[5] Zheng, H. M., Smith, R. K., Jun, Y. W., Kisielowski, C., Dahmen, U. & Alivisatos, A. P. Observation of single colloidal platinum nanocrystal growth trajectories. *Science* **324**, 1309–1312 (2009).

[6] Radisic, A., Ross, F. M. & Searson, P. C. In situ study of the growth kinetics of individual island electrodeposition of copper. *Journal of Physical Chemistry B* **110**, 7862–7868 (2006).

[7] de Jonge, N. & Ross, F. M. Electron microscopy of specimens in liquid. *Nature Nanotechnology* **6**, 695–704 (2011).

[8] Grogan, J. M. & Bau, H. H. The nanoaquarium: A platform for in situ transmission electron microscopy in liquid media. *Journal of Microelectromechanical Systems* **19**, 885–894 (2010).

[9] Gelbart, W. M., Bruinsma, R. F., Pincus, P. A. & Parsegian, V. A. Dna-inspired electrostatics. *Physics Today* **53**, 38–44 (2000).

[10] de Jonge, N., Poirier-Demers, N., Demers, H., Peckys, D. B. & Drouin, D. Nanometer-resolution electron microscopy through micrometers-thick water layers. *Ultramicroscopy* **110**, 1114–1119 (2010).

[11] White, E. R., Mecklenburg, M., Singer, S. B., Aloni, S. & Regan, B. C. Imaging nanobubbles in water with scanning transmission electron microscopy. *Applied Physics Express* **4**, 055201 (2011).

[12] Zheng, H., Claridge, S. A., Minor, A. M., Alivisatos, A. P. & Dahmen, U. Nanocrystal diffusion in a liquid thin film observed by in situ transmission electron microscopy. *Nano Letters* **9**, 2460–2465 (2009).

[13] Klein, K. L., Anderson, I. M. & De Jonge, N. Transmission electron microscopy with a liquid flow cell. *Journal of Microscopy* **242**, 117–123 (2011).

[14] Grogan, J. M., Rotkina, L. & Bau, H. H. In situ liquid-cell electron microscopy of colloid aggregation and growth dynamics. *Physical Review E* **83** (2011).

[15] Evans, J. E., Jungjohann, K. L., Browning, N. D. & Arslan, I. Controlled growth of nanoparticles from solution with *In Situ* liquid transmission electron microscopy. *Nano Letters* **11**, 2809–2813 (2011).

[16] de Jonge, N., Peckys, D. B., Kremers, G. J. & Piston, D. W. Electron microscopy of whole cells in liquid with nanometer resolution. *Proceedings of the National Academy of Sciences of the United States of America* **106**, 2159–2164 (2009).

[17] Liu, K. L., Wu, C. C., Huang, Y. J., Peng, H. L., Chang, H. Y., Chang, P., Hsu, L. & Yew, T. R. Novel microchip for in situ tem imaging of living organisms and bio-reactions in aqueous conditions. *Lab on a Chip* **8**, 1915–1921 (2008).

[18] Peckys, D. B. & de Jonge, N. Visualizing gold nanoparticle uptake in live cells with liquid scanning transmission electron microscopy. *Nano Letters* **11**, 1733–1738 (2011).

[19] Creemer, J., Santagata, F., Morana, B., Mele, L., Alan, T., Iervolino, E., Pandraud, G. & Sarro, P. An all-in-one nanoreactor for high-resolution microscopy on nanomaterials at high pressures. *2011 IEEE 24th International Conference on Micro Electro Mechanical Systems (MEMS)* **24**, 1103–1106 (2011).

[20] Israelachvili, J. N. *Intermolecular and surface forces* (Academic Press, Burlington, MA, 2011).

[21] Min, Y., Akbulut, M., Kristiansen, K., Golan, Y. & Israelachvili, J. The role of interparticle and external forces in nanoparticle assembly. *Nature Materials* **7**, 527–538 (2008).

[22] Kazoe, Y. & Yoda, M. Measurements of the near-wall hindered diffusion of colloidal particles in the presence of an electric field. *Applied Physics Letters* **99**, 124104–3 (2011).

[23] Holmqvist, P., Dhont, J. K. G. & Lang, P. R. Anisotropy of brownian motion caused only by hydrodynamic interaction with a wall. *Physical Review E* **74**, 021402 (2006).

[24] Cazaux, J. Correlations between ionization radiation damage and charging effects in transmission electron microscopy. *Ultramicroscopy* **60**, 411–425 (1995).

[25] Duhr, S. & Braun, D. Why molecules move along a temperature gradient. *Proceedings of the National Academy of Sciences* **103**, 19678–19682 (2006).

[26] Kohl, H., Rose, H. & Schnabl, H. Dose-rate effect at low temperatures in fbem and stem due to object-heating. *Optik* **58**, 11–24 (1981).

[27] Chen, R., Lu, M. C., Srinivasan, V., Wang, Z., Cho, H. H. & Majumdar, A. Nanowires for enhanced boiling heat transfer. *Nano Letters* **9**, 548–553 (2009).

[28] Craig, V. S. J. Very small bubbles at surfaces-the nanobubble puzzle. *Soft Matter* **7**, 40–48 (2011).

[29] Cavicchi, R. E. & Avedisian, C. T. Bubble nucleation and growth anomaly for a hydrophilic microheater attributed to metastable nanobubbles. *Physical Review Letters* **98**, 124501 (2007).

[30] Slifka, A. J., Singh, G., Lauria, D. S., Rice, P. & Mahajan, R. L. Observations of nanobubble formation on carbon nanotubes. *Applied Physics Express* **3**, 065103 (2010).

[31] Tyrrell, J. W. G. & Attard, P. Images of nanobubbles on hydrophobic surfaces and their interactions. *Physical Review Letters* **87**, 176104 (2001).

[32] Attard, P., Moody, M. P. & Tyrrell, J. W. G. Nanobubbles: the big picture. *Physica a-Statistical Mechanics and Its Applications* **314**, 696–705 (2002).

[33] Simonsen, A. C., Hansen, P. L. & Klosgen, B. Nanobubbles give evidence of incomplete wetting at a hydrophobic interface. *Journal of Colloid and Interface Science* **273**, 291–299 (2004).

[34] Evans, D. R., Craig, V. S. J. & Senden, T. J. The hydrophobic force: nanobubbles or polymeric contaminant? *Physica a-Statistical Mechanics and Its Applications* **339**, 101–105 (2004).

[35] Matsumoto, M. & Tanaka, K. Nano bubble - size dependence of surface tension and inside pressure. *Fluid Dynamics Research* **40**, 546 (2008).

[36] Radisic, A., Vereecken, P. M., Hannon, J. B., Searson, P. C. & Ross, F. M. Quantifying electrochemical nucleation and growth of nanoscale clusters using real-time kinetic data. *Nano Letters* **6**, 238–242 (2006).

[37] Fan, Y. W., Singer, S. B., Bergstrom, R. & Regan, B. C. Probing Planck's law with incandescent light emission from a single carbon nanotube. *Physical Review Letters* **102**, 187402 (2009).

[38] Yokota, T., Murayama, M. & Howe, J. M. In situ transmission-electron-microscopy investigation of melting in submicron al-si alloy particles under electron-beam irradiation. *Physical Review Letters* **91**, 265504 (2003).

[39] Arora, P. & Zhang, Z. M. Battery separators. *Chemical Reviews* **104**, 4419–4462 (2004).

[40] Bruce, P. G., Freunberger, S. A., Hardwick, L. J. & Tarascon, J.-M. Li-o$_2$ and li-s batteries with high energy storage. *Nature Materials* **11**, 19–29 (2012).

[41] Langer, J. S. Instabilities and pattern formation in crystal growth. *Reviews of Modern Physics* **52**, 1–28 (1980).

[42] Libbrecht, K. G. The physics of snow crystals. *Reports on Progress in Physics* **68**, 855–895 (2005).

[43] Rosso, M., Chassaing, E., Fleury, V. & Chazalviel, J. N. Shape evolution of metals electrodeposited from binary electrolytes. *Journal of Electroanalytical Chemistry* **559**, 165–173 (2003).

[44] Devos, O., Gabrielli, C., Beitone, L., Mace, C., Ostermann, E. & Perrot, H. Growth of electrolytic copper dendrites i: Current transients and optical observation. *Journal of Electroanalytical Chemistry* **606**, 75–84 (2007).

[45] Tang, S., Backofen, R., Jincheng, W., Zhou, Y., Voigt, A. & Yu, Y.-M. Three-dimensional phase-field crystal modeling of fcc and bcc dendritic crystal growth. *Journal of Crystal Growth* **334**, 146–152 (2011).

[46] Bridel, J.-S., Azais, T., Morcrette, M., Tarascon, J.-M. & Larcher, D. *In Situ* observation and long-term reactivity of si/c/cmc composites electrodes for li-ion batteries. *Journal of The Electrochemical Society* **158**, A750–A759 (2011).

[47] Dolle, M., Sannier, L., Beaudoin, B., Trentin, M. & Tarascon, J.-M. Live scanning electron microscope observations of dendritic growth in lithium/polymer cells. *Electrochemical and Solid-State Letters* **5**, A286–A289 (2002).

[48] Liu, X. H., Zhong, L., Zhang, L. Q., Kushima, A., Mao, S. X., Li, J., Ye, Z. Z., Sullivan, J. P. & Huang, J. Y. Lithium fiber growth on the anode in a nanowire lithium ion battery during charging. *Applied Physics Letters* **98**, 183107 (2011).

[49] Ghassemi, H., Au, M., Chen, N., Heiden, P. A. & Yassar, R. S. Real-time observation of lithium fibers growth inside a nanoscale lithium-ion battery. *Applied Physics Letters* **99**, 123113 (2011).

[50] Ross, F. M. Electrochemical nucleation, growth and dendrite formation in liquid cell tem. *Microscopy and Microanalysis* **16**, 326–327 (2010).

[51] White, E. R., Mecklenburg, M., Shevitski, B., Singer, S. B. & Regan, B. C. Charged nanoparticle dynamics in water induced by scanning transmission electron microscopy. *Langmuir* **28**, 3695–3698 (2012).

[52] Spence, J. C. H. *High-Resolution Electron Microscopy* (Oxford University Press, Oxford; New York, 2003).

[53] Wranglen, G. Dendrites and growth layers in the electrocrystallization of metals. *Electrochimica Acta* **2**, 130–143 (1960).

[54] Popov, K., Stojilkovic, E., Radmilovic, V. & Pavlovic, M. Morphology of lead dendrites electrodeposited by square-wave pulsating overpotential. *Powder Technology* **93**, 55–61 (1997).

[55] Sawatani, S., Ogawa, S., Yoshida, T. & Minoura, H. Formation of highly crystallized β-PbO thin films by cathodic electrodeposition of Pb and its rapid oxidation in air. *Advanced Functional Materials* **15**, 297–302 (2005).

[56] Koneshan, S., Rasaiah, J. C., Lynden-Bell, R. M. & Lee, S. H. Solvent structure, dynamics, and ion mobility in aqueous solutions at 25°C. *Journal of Physical Chemistry B* **102**, 4193–4204 (1998).

[57] Sato, H., Yui, M. & Yoshikawa, H. Ionic diffusion coefficient of cs$^+$, pb^{2+}, sm^{3+}, ni^{2+}, seo$_4^{2-}$ and tco$_4^-$ in free water determined from conductivity measurements. *Journal of Nuclear Science and Technology* **33**, 950–955 (1996).

[58] Wong, S. M. & Abrantes, L. M. Lead electrodeposition from very alkaline media. *Electrochimica Acta* **51**, 619–626 (2005).

[59] Dufreche, J.-F., Bernard, O., Durand-Vidal, S. & Turq, P. Analytical theories of transport in concentrated electrolyte solutions from the msa. *Journal of Physical Chemistry B* **109**, 9873–9884 (2005).

[60] Morris, R. B., Franta, D. J. & White, H. S. Electrochemistry at Pt band electrodes of width approaching molecular dimensions - breakdown of transport-equations at very small electrodes. *Journal of Physical Chemistry* **91**, 3559–3564 (1987).

[61] Bockris, J. O., Reddy, A. K. N. & Gamboa-Aldeco, M. E. *Modern Electrochemistry* (Plenum Press, New York, 1998).

[62] Bullard, J. W. Approximate rate constants for nonideal diffusion and their application in a stochastic model. *Journal of Physical Chemistry A* **111**, 2084–2092 (2007).

[63] Dresselhaus, M. & Dresselhaus, G. Intercalation compounds of graphite. *Advances in Physics* **30**, 139–326 (1981).

[64] Daumas, N. & Herold, M. A. Notes des membres et correspondants et notes presentees ou transmises par leurs soins. *Comptes rendus hebdomadaires des sances de l'Acadmie des sciences. Srie C, Sciences chimiques* **268**, 373 (1969).

[65] Levi-Setti, R., Crow, G., Wang, Y. L., Parker, N. W., Mittleman, R. & Hwang, D. M. High-resolution scanning-ion-microprobe study of graphite and its intercalation compounds. *Phys. Rev. Lett.* **54**, 2615–2618 (1985).

[66] Rudorff, U., Von W. und Hofmann. Über graphitsalze. *Zeitshrift fur anorganishe und allgemeine Chemie* **238** (1951).

[67] Hennig, G. The properties of the interstitial compounds of graphite. i. the electronic structure of graphite bisulfate. *The Journal of Chemical Physics* **19** (1951).

[68] Aronson, S., Frishberg, C. & Frankl, G. Thermodynamic properties of the graphite-bisulfate lamellar compounds. *Carbon* **9**, 715 – 723 (1971).

[69] Metrot, A. & Fischer, J. Charge transfer reactions during anodic oxidation of graphite in {H2SO4}. *Synthetic Metals* **3**, 201 – 207 (1981).

[70] Eklund, P., Olk, C., Holler, F., Spolar, J. & Arakawa, E. Raman scattering study of the staging kinetics in the c-face skin of pyrolytic graphite-h2so4. *Journal of Materials Research* **1**, 361–367 (1986).

[71] Thermodynamic data for anodic solid state graphite oxidation products in 96% sulphuric acid. *Carbon* **30**, 223 – 228 (1992).

[72] Dimiev, A. M., Bachilo, S. M., Saito, R. & Tour, J. M. Reversible formation of ammonium persulfate/sulfuric acid graphite intercalation compounds and their peculiar raman spectra. *ACS Nano* **6**, 7842–7849 (2012).

[73] Dimiev, A. M., Ceriotti, G., Behabtu, N., Zakhidov, D., Pasquali, M., Saito, R. & Tour, J. M. Direct real-time monitoring of stage transitions in graphite intercalation compounds. *ACS Nano* **7**, 2773–2780 (2013).

[74] Shevitski, B., Mecklenburg, M., Hubbard, W. A., White, E. R., Dawson, B., Lodge, M. S., Ishigami, M. & Regan, B. C. Dark-field transmission electron microscopy and the Debye-Waller factor of graphene. *Physical Review B* **87**, 045417 (2013).

[75] Ziambaras, E., Kleis, J., Schröder, E. & Hyldgaard, P. Potassium intercalation in graphite: A van der waals density-functional study. *Phys. Rev. B* **76**, 155425 (2007).

[76] Leamy, H. J. Charge collection scanning electron-microscopy. *Journal of Applied Physics* **53**, R51–R80 (1982).

[77] Johnson, J. B. Thermal agitation of electricity in conductors. *Phys. Rev.* **32**, 97–109 (1928).

[78] Nyquist, H. Thermal agitation of electric charge in conductors. *Phys. Rev.* **32**, 110–113 (1928).

[79] Callen, H. B. & Welton, T. A. Irreversibility and generalized noise. *Phys. Rev.* **83**, 34–40 (1951).

[80] Britnell, L., Ribeiro, R. M., Eckmann, A., Jalil, R., Belle, B. D., Mishchenko, A., Kim, Y.-J., Gorbachev, R. V., Georgiou, T., Morozov, S. V., Grigorenko, A. N., Geim, A. K., Casiraghi, C., Neto, A. H. C. & Novoselov, K. S. Strong light-matter interactions in heterostructures of atomically thin films. *Science* **340**, 1311–1314 (2013).

[81] Yu, W. J., Liu, Y., Zhou, H., Yin, A., Li, Z., Huang, Y. & Duan, X. Highly efficient gate-tunable photocurrent generation in vertical heterostructures of layered materials. *Nature Nanotechnology* **8**, 952958 (2013).

[82] Butz, B., Dolle, C., Niekiel, F., Weber, K., Waldmann, D., Weber, H. B., Meyer, B. & Spiecker, E. Dislocations in bilayer graphene. *Nature* **505**, 533537 (2014).